EXPERIMENTAL AND NUMERICAL INVESTIGATION OF TIP CLEARANCE EFFECTS IN A HIGH-SPEED CENTRIFUGAL COMPRESSOR

by

Matthew F. Fuehne

A Thesis

Submitted to the Faculty of Purdue University

In Partial Fulfillment of the Requirements for the degree of

Master of Science in Aeronautics and Astronautics

School of Aeronautics and Astronautics

West Lafayette, Indiana

August 2020

THE PURDUE UNIVERSITY GRADUATE SCHOOL
STATEMENT OF COMMITTEE APPROVAL

Dr. Nicole Key, Chair

School of Mechanical Engineering

Dr. Sally Bane

School of Aeronautics and Astronautics

Dr. Carson Slabaugh

School of Aeronautics and Astronautics

Approved by:

Dr. Gregory Blaisdell

"Shot clock down to 9, Cline, can't dribble himself free, he's going to have to take a long one. Cline, step back 3, for the tie…"

~ Brian Anderson

ACKNOWLEDGMENTS

First and foremost, I would like to thank my advisor, Nicole Key, for giving me this opportunity two years ago and for her continued support and guidance throughout. I have become a better researcher and grown as an engineer during my time in the lab. I would also like to thank Prof. Sally Bane and Prof. Carson Slabaugh for serving on my committee. Fangyuan Lou has been instrumental in helping me understand centrifugal compressors and I would like to thank him for his technical input, knowledge, and contributions over the last two years. I am also very grateful for the help from Grant Malicoat, Rob McGuire, Toby Lamb, Jen Ulutas and the entire support staff at Zucrow Laboratories.

This project was sponsored by Honeywell Aerospace and I would like to acknowledge their contributions, both technically and financially. Darrell James, Andrew Loudenbeck, Jacob Harding, Mark De La Torre, and Glen Nawrocki have been a pleasure to work with. Thank you also to the students of the Honeywell team here at Purdue, William Brown, Trey Harrison, Amelia Brooks, and Evan Bond. They were a great team to share the ups and downs of experimental research with. And to the members of the rest of the lab, Will, Matt, Nick, Doug, Yujun, Andrew, and Yu Ning, it has been an absolute pleasure coming to lab each day and I am thankful for your friendship and assistance in various ways.

Lastly, I owe a huge thank you to my parents, Joe and Gail, for having supported me over the last six years here at Purdue. Your continuous encouragement and patience throughout my time here has allowed me to find and pursue something that I enjoy and to keep me going when things got tough. And thank you to Laura, who was always there to talk and get my mind off work when I needed it most. Your support and motivation have meant a great deal to me. I would not be who I am today without you guys.

TABLE OF CONTENTS

LIST OF TABLES

LIST OF FIGURES

NOMENCLATURE

Acronyms	**Definition**
AC	Alternating Current
APU	Auxiliary Power Unit
CR	Clearance Ratio
CFD	Computational Fluid Dynamics
HP	Horsepower
LDA	Laser Doppler Anemometry
LDV	Laser Doppler Velocity
PE	Peak Efficiency
PS	Pressure Surface
PID	Proportional Integral Derivative
PIV	Particle Image Velocimetry
RPM	Revolutions Per Minute
SS	Suction Surface
SSCC	Single Stage Centrifugal Compressor
TPR	Total Pressure Ratio
TTR	Total Temperature Rise Ratio

Greek	**Definition**
γ	Ratio of specific heats
Δ	Change in a quantity
η	Efficiency
η_{diff}	Diffuser effectiveness
ρ	Density
ψ	Work factor
Ω	Mass flow – speed parameter

Subscripts	**Definition**
0i	Total conditions at station i
i	Static conditions at station i
ax	Axial
abs	Absolute
CFD	Computational data
corr, c	Corrected conditions
diff	Diffuser
eff	Effective
EXP	Experimental data
Imp	Impeller
m	Meridional
mech	Mechanical
ref	Reference condition
θ	Tangential direction
s	Isentropic condition

Symbols	**Definition**
A	Constant in roughness conversion equation
a	Speed of sound
a_c	Coefficient in tip clearance trend equation
B	Performance parameter in tip clearance trend equation
b	Blade height
C_p	Diffuser static pressure rise coefficient
C_d	Discharge coefficient
Cl	Clearance
D	Diameter
d	Throat diameter of venturi flow meter
e_a^{21}	Approximate relative error between grids 1 and 2

e_{ext}^{21}	Extrapolated relative error between grid 1 and extrapolation
GCI^{21}	Fine-grid convergence index
h	Enthalpy
K_{bar}	Blockage factor
K_{diff}	Diffuser total pressure loss coefficient
k	Slope in tip clearance trend equation
k_s	Equivalent sand grain roughness
M	Mach number
$\dot{m}$	Mass flow rate
N	Rotational speed
P	Pressure
R	Gas constant
R_a	Centerline average roughness
S	Entropy
t	Tip clearance gap measurement
U	Wheel speed
V	Velocity

ABSTRACT

The objective of this research is to investigate the effects of tip clearance on the stage and component performance in a high-speed centrifugal compressor. The experimental data were compared against results from a numerical model to assess the ability of the numerical simulation to predict the effects of tip clearance. Experimental data were collected at Purdue University on the Single Stage Centrifugal Compressor (SSCC), a high-speed, high-pressure ratio test compressor sponsored by Honeywell Aerospace. Numerical simulations were completed using the ANSYS CFX software suite and part of the research computing clusters located at Purdue University.

Two tip clearances were tested, the nominal tip clearance and a tip clearance that is 66% larger than the nominal clearance, at speeds from 60% to 100% corrected speed. To compare data points with different tip clearances, various parameters were evaluated, and one was chosen. The value of $TPR/\dot{m}_{inlet\ corr}$ best represented similar loading conditions, and thus similar incidences, for each tip clearance and was chosen as the best method for comparing similar data points taken with different clearances. Stage and component performance were focused on the sensitivity of each performance parameter to the changing of the tip clearance. The stage total pressure ratio and stage efficiency showed moderate sensitivity while the stage work factor showed much lower sensitivity. The impeller is more sensitive to changing tip clearances than the stage is, showing greater changes when comparing data from each tip clearance. The diffuser was on the same order of sensitivity as the impeller, with marginally higher sensitivities for some parameters. It was found that by the typical performance metrics, the diffuser performs worse at the nominal clearance than at the larger clearance. Upon further investigation though, the impeller is providing a higher static pressure and therefore, more diffusion, at the nominal clearance so the diffuser must perform less diffusion during nominal clearance operation.

To assess the validity of a prediction of the performance and sensitivity of the stage and components to the tip clearance, a numerical model was developed and validated. The numerical model was able to reasonably predict the stage performance with better comparisons of performance in the impeller and worse in the diffuser. The instrumentation in the experiment was replicated in the software to calculate performance the same way it is calculated experimentally so that the results would be comparable. While the performance of the stage and components was

lacking in some areas, the trends predicted were similar to those calculated from the experimental data. As with the performance, the trends in the impeller matched very well between the experiment and the numerical simulation. The trends in stage and diffuser performance were predicted more accurately than the stage and diffuser performance maps and were able to capture the magnitude of the change in performance caused by changing the tip clearance.

1. INTRODUCTION

1.1 Motivation

Centrifugal compressors have a wide range of use, from aviation engines to domestic appliances. Due to the need for high performance and efficiency, however, much of the research on centrifugal compressors is focused on the aircraft engine application (Cumpsty, 1989). Centrifugal compressors typically have higher stage total pressure ratios than axial compressors but lower efficiencies because of an increased flow path length and stronger secondary flows (Kunte et al. 2012). The axial compressor has become the primary choice for many aviation applications where size is not the primary constraint in the engine design, because it can achieve a higher efficiency than the centrifugal compressor. However, the potential for improvement and the larger total pressure ratio produced by the centrifugal design while using less stages has driven research to improve the performance of the centrifugal compressor.

A main area of improvement in centrifugal compressors lies in reducing the adverse effects from secondary flows. A contributor to secondary flow that adversely affects the performance is the tip clearance of an unshrouded centrifugal impeller. Tip leakage flows occur when there is a space between the rotating impeller and the stationary shroud. The tip leakage flow mixes with other lower velocity flow and creates the wake region in the jet-wake structure. This flow structure affects the velocity profile at the diffuser inlet, a critical area to the performance of the machine, and can significantly hinder the performance (Kunte et al., 2012). Experimental and numerical investigations have been performed to characterize the decrease in performance with an increasing tip clearance, but many of these investigations focus on stage performance of centrifugal compressors with subsonic inlet Mach numbers. Very little public literature exists analyzing the tip clearance effects on a high-speed, high-pressure ratio centrifugal compressor at the stage and component levels.

Because the tip clearance is chosen during the design phase and the clearance will slowly increase over time because of the wear during compressor operation, predicting the adverse effect on performance is critical in the design stage with the use of computational fluid dynamics (CFD). Tip leakage flows are complex, and CFD models used for design iterations may have limited

success in predicting absolute performance metrics, but CFD can provide understanding of the flow field to allow for better informed decisions to be made.

1.2 Tip Clearance in Centrifugal Compressors

1.2.1 Shrouded vs. Unshrouded Compressors

Two different designs for centrifugal compressors are available - shrouded and unshrouded. The main design difference is that the shroud is connected to and rotates with the impeller in a shrouded impeller whereas the shroud is stationary, and a small gap exists in the unshrouded version. Shrouded impellers are mainly used in industrial and multistage applications (Harada, 1985). However, in turbochargers and gas turbine applications, the impeller is unshrouded due to higher mechanical stresses and manufacturing difficulties with shrouded designs (Harada, 1985). Due to the gap between the shroud and the impeller in unshrouded compressors, there exists a tip leakage flow that interacts with the other impeller secondary flows and leads to significant losses in the compressor.

Secondary flows are those that are not part of the primary flow (Cumpsty, 1989). In the case of centrifugal impellers, the secondary flow exists in blade passages but is perpendicular to the blades instead of parallel to the blades, which is the primary flow. These secondary flows can have a major impact on the velocity distribution and the effectiveness of the diffuser. Because of the effects of secondary flows, the flow pattern exiting the impeller is referred to as the jet-wake structure. The jet consists of the high energy fluid while the wake is made up of low momentum fluid, with respect to the rotor-relative reference frame. The wake accounts for about 15% of the entire mass flow at the impeller exit and also consists of a stable, but sharp, velocity gradient between the main flow and the wake (Eckardt, 1976).

Eckardt shows in his experiment that the flow is uniform through the impeller until almost halfway through the meridional length of the impeller (1976). Near the knee of the impeller, the effects of secondary flows start to become noticeable. As the flow reaches the exducer though, the effects on the velocity distribution are more severe. This distorted impeller exit flow leads to significant losses through the diffuser due to the tip clearance and other secondary flows.

Hong et al. (2003) used a 3D LDA system on an unshrouded compressor with a vaneless diffuser to take time-resolved measurements of total pressure at the impeller exit for three diffuser

tip clearance ratios, which is defined as the tip clearance gap divided by the blade height at the impeller exit. Their results show that for a given operating condition, if the tip clearance is increased, the total pressure deficit also increases leading to a larger wake in the passage flow. This is illustrated in Figure 1.1, which shows the effects of increasing tip clearance on the flow profile at the impeller exit. In the nominal clearance case shown on the top, the jet and the wake are not affected significantly by the tip leakage flow. But when the tip clearance is increased, the tip leakage flow becomes significant and interferes with the main flow in the passage, as shown in the bottom figure.

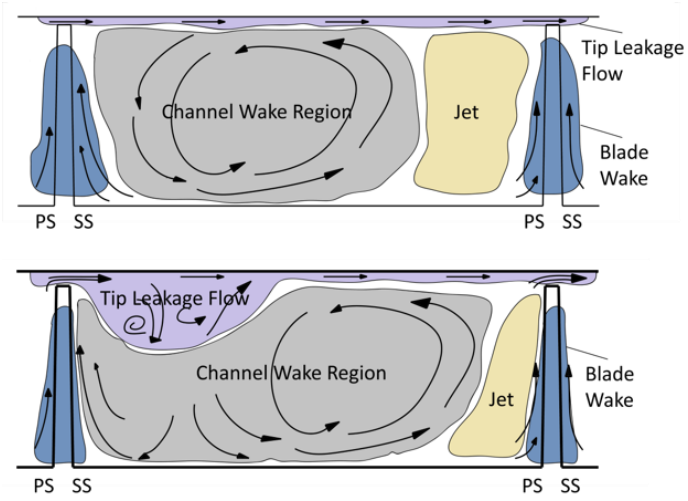

Figure 1.1 Graphic showing the impeller exit flow field for a nominal tip clearance (top) and larger tip clearance (bottom)

1.2.2 Tip Clearance Measurement Techniques

Measurements of the tip clearance are normally made in three different locations on the impeller – the inducer, the knee and the exducer. While all three measurements are important to consider, the exducer measurement is the most significant because the gap between the impeller and the shroud at the impeller exit is mostly in the axial direction. The impeller tip clearance is changed in the axial direction through various methods. All three measurements will change when adjusting the clearance, but the axial measurement at the exducer is impacted the most when moving the impeller, as depicted in Figure 1.2.

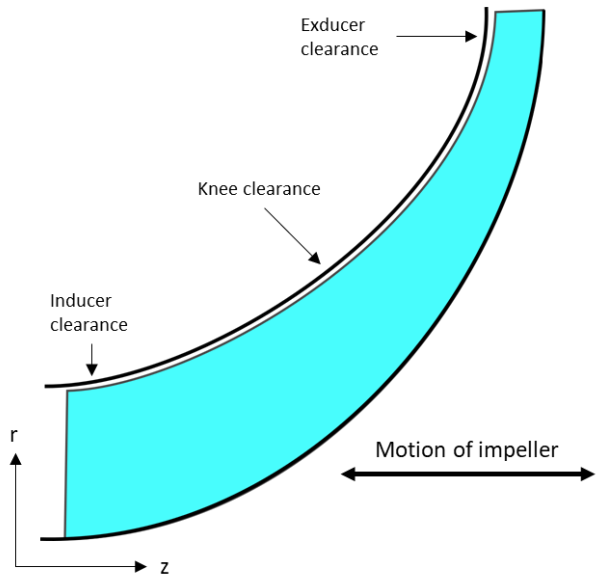

Figure 1.2 Locations of tip clearance measurements

Tip clearance measurements can be made in two main ways, running and stationary. Running measurements are made while the impeller is spinning, and stationary measurements are made when the compressor is installed in the test configuration but not spinning. Obtaining an estimate of the running tip clearance from a stationary measurement can be difficult since impeller thrust, possible blade deflections due to centrifugal effects, and thermal expansion will cause a change in tip clearance at speed. Stationary measurements are easier to record, but they are not as accurate as running measurements, which can be significantly more difficult to obtain.

Stationary measurements can be acquired in multiple ways. Backman et al. (2007) placed a lead wire of known diameter between the impeller and the shroud while assembling and then removed it once the shroud was fixed in place. Hong et al. (2003) used a shim to move the shroud away from the impeller to change the tip clearance. And Eisenlohr and Chladek (1994) determined the desired running tip clearance and then used a thermal growth analysis at steady state to determine the corresponding room temperature clearance at which the compressor should be set.

Running tip clearance can be difficult to measure, and while many early experiments did not actively measure the tip clearance, recent experiments have begun to do this by two different methods. A method used by Backman et al. (2007) measured the tip clearance by placing a plastic stick with a diameter of 6 millimeters through the shroud while the impeller was spinning. The top side of the stick had a reference surface that would be flush with the shroud and the impeller would

cut the stick, indicating the tip clearance. The researchers then changed the tip clearance with an active magnetic bearing (Backman et al., 2007).

Another method is continuous measurement of tip clearance while testing. Weimer (1992) designed and tested an active tip clearance measurement system using high-frequency capacitance sensors. Weimer (1992) also indirectly measured the tip clearance by measuring the clearance of the back face of the impeller. Capacitance probes were still used to measure the clearance on the back face, but with fewer frequency requirements than those directly measuring the clearances. The probes measuring the clearance on the back face do not need the frequency capability to resolve a blade passing by the probe but could still capture the required information about the current tip clearance.

1.3 Effects on Performance

Improving the performance of a centrifugal compressor is the main motivation for understanding and mitigating the effects of loss mechanisms, such as secondary flows. Compressor performance parameters include total pressure ratio, efficiency, work input, and stall margin.

1.3.1 Steady Performance

The tip clearance effects on steady centrifugal compressor performance are well documented in the literature from experimental and numerical perspectives. Many researchers focus their efforts on understanding the effects on the efficiency, total pressure ratio, and work input. The design and operating condition of the compressor, though, significantly affect the magnitude of the tip clearance effects on the various performance parameters.

An important parameter that is affected by the tip clearance is the efficiency. Efficiency is defined as

$$\eta = \frac{h_{02s} - h_{01}}{h_{02} - h_{01}} \tag{1.1}$$

where the numerator is the isentropic work and the denominator is the actual work needed to achieve a certain pressure ratio. By assuming a perfect gas, the constant pressure specific heat and the inlet total temperature can be divided out of the efficiency equation resulting in

$$\eta = \frac{T_{02s}/T_{01} - 1}{T_{02}/T_{01} - 1} \tag{1.2}$$

Another assumption can be made by using the isentropic relations in the numerator. Replacing the isentropic total temperature ratio with the pressure ratio and the ratio of specific heats, the resulting equation is in terms of the other main performance parameters

$$\eta = \frac{\left(\frac{P_{02}}{P_{01}}\right)^{\frac{\gamma-1}{\gamma}} - 1}{T_{02}/T_{01} - 1} = \frac{TPR^{\frac{\gamma-1}{\gamma}} - 1}{TTR - 1} \tag{1.3}$$

where TPR is the stage total pressure ratio and TTR is the stage total temperature ratio. This simplification gives a direct relationship between the main stage performance parameters of efficiency, total pressure ratio, and total temperature ratio and shows how a change in one parameter can affect the other parameters.

The tip clearance of a centrifugal compressor can have a significant effect on the efficiency of a given machine. Klassen (1977) was one of the first to research tip clearance effects on performance with his 13.65-centimeter tip-diameter centrifugal compressor. The compressor had a design pressure ratio of 6, a design speed of 80,000 rpm and was used for small engine applications. He tested the compressor at four different tip clearance ratios from 50% to 100% corrected speed. The results show a direct correlation between the tip clearance and the overall compressor efficiency. All speedlines from 50% to 100% corrected speed show that as the axial tip clearance is decreased, the efficiency is increased. This is depicted in Figure 1.3 for a single speed and with two different tip clearance ratios where CR2 is smaller than CR1. At 100% corrected speed in the choke condition, the mass flow rate is constant and independent of the tip clearance. However, at lower speeds, the choked mass flow rate does change with tip clearance. Klassen attributes this to inducer choke in the impeller at 100% corrected speed as opposed to diffuser choke at the lower speeds.

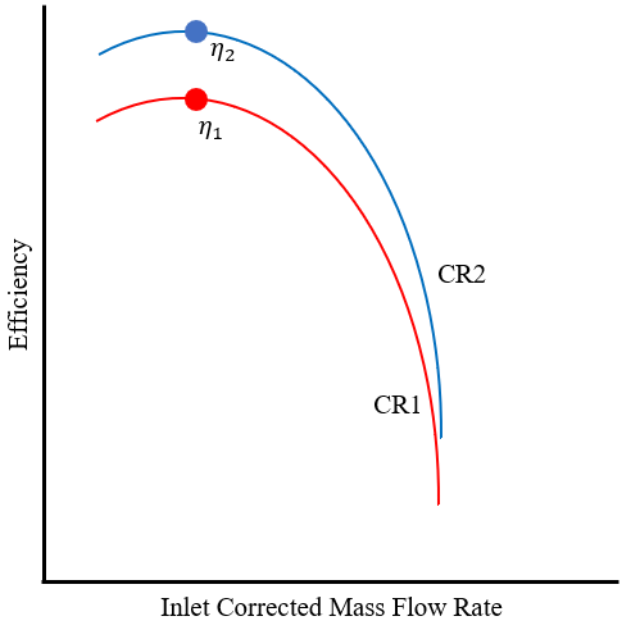

Figure 1.3 Effect of tip clearance on efficiency speedlines

Eisenlohr and Chladek (1994) also discovered a similar trend regarding efficiency and tip clearance using a compressor specifically designed for an Auxiliary Power Unit (APU). They also showed that the isentropic efficiency decreases with increasing tip clearance and that the two quantities are linearly correlated leading to a decrease in isentropic efficiency of 0.35 to 0.45 points per one-point change in tip clearance for 90%, 95%, 100%, and 105% corrected speeds. Brasz (1988), however, used the polytropic efficiency in his results, but still found the same trend. The compressor used in his experiments had a tip diameter of 0.516 meters, spun at a design speed of about 7000 rpm and used refrigerant 11 as the working fluid. He noted that the polytropic efficiency decreased about 0.31% for a percent increase in tip clearance, like the results of Klassen.

Backman et al. (2007) performed a study with six different compressors with different design parameters (such as diffusion ratio, specific speed, and type of diffuser - vaned or vaneless) to evaluate the tip clearance sensitivity on each compressor. They found that compressors with lower efficiencies were not as sensitive to changes in tip clearance as those with higher efficiencies. Also, an impeller coupled with a vaned diffuser was more sensitive to tip clearance than those with a vaneless diffuser. Compressors with larger diffusion ratios showed a more negative effect on

performance with increasing tip clearance, but the specific speed of a machine was not correlated to how sensitive a compressor is to changes in tip clearance.

An experimental and numerical investigation performed by Kunte et al. (2012) with an eight-inch-radius impeller, a nominal speed of 19249 RPM, and a pipe diffuser showed similar experimental results for the tip clearance effect on efficiency. They also compared those results and trends to a numerical model to investigate the ability of the model to predict changes in performance with changing tip clearance. The CFD results showed that the isentropic efficiency agreed well with the experimental data, except near the choke limit where there was a difference of about 0.5 points of efficiency. The good agreement of the computed efficiency to the experimental data is explained by Kunte et al. as the total pressure ratio being overpredicted and the total temperature ratio being underpredicted, both of which will be discussed below. The trend of decreased efficiency with increasing tip clearance is also predicted well by the CFD model near the operating point on the speedline. The numerical results, however, failed to predict the strongly curved section of the speedline, the knee near the choke limit, accurately.

Other numerical investigations have sought to determine the effects of tip clearance on the efficiency and performance of a centrifugal compressor. Tang et al. (2006) performed a numerical analysis on a small centrifugal compressor with an exit diameter of 4.8 centimeters and five different tip clearance ratios with respect to the impeller exit blade height: 0%, 5%, 10%, 16.7%, and 25%. The results showed that the efficiency decreased linearly with increasing tip clearance at various speeds. Eum and Kang (2002) performed a similar analysis on a compressor with an impeller exit radius of 8.2 centimeters and rotational speed of 60,000 RPM. Not only did they show that the efficiency decreased as tip clearance increased, but they evaluated the most significant factors contributing to the decrease in efficiency and found that entropy generation had the strongest effect on the decrease in efficiency as tip clearance increases.

Klassen (1977) also investigated the tip clearance effect on total pressure ratio in his experiments. His results showed that there was very little change in total pressure ratio below 70% corrected speed. Between 70% and 100% corrected speed, though, the equivalent mass flow rate increased with decreasing tip clearance in the upper part of the speedline. And at design speed, the total pressure increased significantly with decreasing tip clearance. Brasz (1988) also reached the same conclusions regarding the total pressure ratio. The mass flow rate in choke at design speed was constant for all tip clearances but this differed near the operating line and surge, like the results

from Klassen. The results were also the same, smaller tip clearances yielded higher pressure ratios (Brasz, 1988). Similar experimental results have also been published by Eisenlohr and Chladek (1994) and Jaatinen, et al. (2012).

Numerical results regarding the decrease in total pressure ratio are also consistent with the experimental results. Kunte et al. (2012) showed that their computational results predict the shape of the total pressure speedline relatively well but the total pressure ratio is 2% overpredicted by the model. Tang et al. (2006) found similar trends with comparable drops in total pressure ratio with increases in tip clearance at various operational speeds.

Finally, the work input into the compressor is examined as a function of the tip clearance ratio. Eisenlohr and Chladek (1994) used the total temperature ratio, the ratio of the outlet total temperature divided by the inlet total temperature, to represent the work input. They showed four different speedlines for the temperature ratio and seven tip clearances on each speedline. At 90% and 95% corrected speed, the tip clearance had negligible effect on the temperature ratio but at 100% corrected speed, there was a small increase in the temperature ratio at tighter tip clearances. They also tested at 105% corrected speed, and the tip clearance effects on the temperature ratio were slightly more pronounced, indicating that more work input was needed as the tip clearance becomes smaller. Klassen (1977) used a different parameter and published a work factor for his experiments, defined as the change in stagnation enthalpy divided by the rotational speed squared. The conclusions are the same though, as the work factor also slightly increased with decreasing tip clearance. Klassen attributed this to the increased airflow over the blade for large clearances. Because the fluid is passing between the shroud and the impeller, the impeller was not doing as much work on it as with the main flow through the blades, so the work factor was increased for smaller tip clearances.

Similar results for the effect on work input to the compressor due to the tip clearance are presented in numerical studies. Kunte et al. (2012) underpredicted the total temperature ratio by about 0.7% when comparing the numerical results to the experimental data. This underprediction combined with the overprediction of total pressure ratio led to a close efficiency prediction, albeit for the wrong reasons. It is important that the CFD models capture the correct flow physics and trends, rather than matching a certain number because, as was shown, that number could be matched but the flow field could be completely mis-represented, potentially leading to poor design

choices. Tang et al. (2006) showed little change between the input power needed for various tip clearances except near the 0% tip clearance case, where the required work input starts to increase.

1.3.2 Stability

Another important consideration for compressor performance is the stable operating range. Compressor stall occurs when the mass flow rate through the compressor has been reduced to a point where flow disruptions are occurring. The stall margin of the compressor is a parameter that defines how close the operating point is to stall inception. Depending on the compressor and operating parameters, the compressor may first reach rotating stall and then surge, or the compressor may surge quickly after reaching the last stable operating point. A few investigations into the effects of tip clearance on the stability margin and stall inception have been completed, but the results are inconsistent.

Eisenlohr and Chladek (1994) found interesting results relating the stable operating range to the relative tip clearance. They found that the stable operating range is increased as the tip clearance is increased for the 100% corrected speed condition. Therefore, the onset of surge happened more quickly when the relative tip clearance is decreased, but there was no comment on rotating stall inside the compressor. Hong et al. (2003) found similar results with the surge margin of their compressor decreasing with smaller tip clearances, however, they found an optimal tip clearance ratio for operation to maximize surge margin. The researchers tested six different tip clearance ratios and found that in the middle of their tip clearance ratio range, the surge limit was maximized and that either increasing or decreasing the tip clearance ratio would result in a lower surge limit.

Schleer et al. (2008) also investigated this effect with two different clearance ratios for a variety of rotational speeds and found similar results at low speeds but conflicting results at high speeds. Their compressor was a scaled-up centrifugal compressor for use in small-scale power generation or automotive turbochargers. For higher speeds, the stability margin is unchanged by the tip clearance ratio. The pressure ratio is increased for the same rotational speed and smaller tip clearances, but the line indicating surge for high speeds is nearly linear in that region meaning there is no effect on the stability margin at high speeds. However, in the low speed region, there were quite a few changes between the two tip clearance ratios. The smaller tip clearance ratio delays the onset of rotating stall because of the difference in flow pattern at the impeller exit, but

at high speeds, the surge margin depends more on the overall setup of the compressor and less on the diffuser inlet flow pattern (Schleer et al., 2008).

Another investigation by Buffaz and Trébinjac (2012) sought to also understand how tip clearance affects the surge margin, and they reported similar results to Schleer et al (2008). Only one speedline, the cruise speed for their compressor at 92.7% corrected speed, was published at two difference clearances. But there was no change in surge margin between the two tip clearances. And lastly, Methel (2016) found similar results to Buffaz and Trébinjac (2012). She tested four different speeds, 80%, 90%, 95%, and 100% corrected speed, at two different clearances and showed that the surge margin does not change significantly at any speed between the clearances. Methel noted that the surge margin for each corrected speed is within 0.9% between the two clearances, which is noted as negligible.

1.3.3 Component Analysis

Much of the tip clearance research has focused on the effects on stage performance. Perhaps equally important is the effect on each component in the compression system to better understand how a compressor stage performs and where to make improvements in the design.

Kunte et al. (2012) have performed the most extensive component analysis and the majority of their analysis is focused on the pipe diffuser. They evaluated the normalized static pressure recovery coefficient (C_p) and the normalized total pressure loss in the diffuser. As they throttled the compressor, the static pressure recovery coefficient increased, and the total pressure loss decreased. At the design point, the numerical simulation overpredicted the value of C_p by 1% and underpredicted the total pressure loss by 0.005. The larger tip clearance resulted in a decreased in C_p of 0.75% and increased total pressure losses. Their computational model was more sensitive to the change in tip clearance, though, as the decrease in C_p predicted by CFD is almost twice that of the experiment. Despite the difference in magnitude, CFD correctly predicted the trend of diffuser performance.

A numerical study by Eum and Kang (2002) focused on the impeller performance of a centrifugal compressor designed for an APU with an impeller exit radius of 8.2 centimeters and a design speed of 60,000 RPM. To isolate the impeller performance, though, the simulation only considered a vaneless diffuser to eliminate the effects of impeller-diffuser interaction (the actual

compressor featured a vaned diffuser). Using the computational model, the variations of total pressure ratio and total temperature ratio with respect to the zero-tip-clearance case were evaluated along the meridional length of the passage. As the tip clearance was increased, the variations of both total pressure and total temperature increased, as did the entropy generation along the flow passage. Near the leading edge of the splitter blade, there was a decrease in the variation in total pressure and total temperature at all tip clearances before the variations then increase again. Most of the entropy generation and differences in entropy generation between tip clearances also occurred after the leading edge of the splitter blade. The authors also showed that most of the differences in total pressure and total temperature at the impeller exit are between the midway point of the span and the shroud, showing that the change in tip clearance does not affect the flow near the hub.

Lastly, a computational study by Tang et al. (2006) was also performed with an impeller and a vaneless diffuser, and they investigated how the flow angles in the impeller change with tip clearance. The incidence increased linearly with increasing tip clearance, and the change in incidence with respect to the tip clearance was higher with increasing speeds. At the exit of the impeller, the relative flow angle also increased with increasing tip clearance, but the angle is the same at different speeds for a given clearance. Therefore, the linear increase in relative flow angle with tip clearance did not change slope between speeds and was of similar magnitudes for all speeds. The absolute flow angle at the impeller exit, however, did change significantly between speeds and tip clearances. As the speed increased, the absolute flow angle decreased for a given tip clearance; and for a given speed, the absolute flow angle increased linearly with increasing tip clearance. The slope of the change in absolute flow angle with tip clearance was consistent between all speeds tested, the magnitude was the main difference.

1.4 Trends in Tip Clearance Sensitivity and Empirical Correlations

The sensitivity of various performance parameters with respect to the tip clearance has been evaluated in some of the previous studies as well. Knowing the sensitivity of the compressor to the tip clearance aids in the understanding of the performance of the compressor and how the tip clearance will affect the performance at various speeds and operating conditions.

Because of the importance of efficiency, much work has been done on understanding the efficiency sensitivity with respect to the tip clearance and quantifying the losses in efficiency due

to the tip clearance. Eisenlohr and Chladek (1994) found an approximately linear trend regarding efficiency and tip clearance using their compressor designed for an APU. As the tip clearance continued to increase, the isentropic efficiency linearly decreased with a one-point change in relative tip clearance leading to a decrease of 0.35 to 0.45 points in isentropic efficiency. Brasz (1988) used polytropic efficiency in his experiments but also noticed a similar trend. There were only two tip clearance ratios tested so a linear trend was assumed and resulted in an efficiency decrease of about 0.31% per percent increase in tip clearance.

Tang et al. (2006) also suggested a linear curve that was fit to each speed that presented the change in efficiency equal to a slope multiplied by the clearance ratio. As the speed increased, the slope of efficiency drop with tip clearance increased to about -0.31. Eum and Kang (2002) also characterized the efficiency drop again as a linear function with a slope and the tip clearance ratio. They, however, compared the efficiency drop at various tip clearances to the efficiency at a zero tip clearance. Because of this method, their slope is positive, but the magnitude is very similar at 0.35.

Attempts have been made to quantify the losses in efficiency due to the tip clearance as empirical correlations. One of the first equations derived provides a linear relationship between the efficiency drop and the tip clearance

$$\frac{\Delta\eta}{\eta} = \frac{2a_c t}{b_1 + b_2} \tag{1.4}$$

where η is the efficiency, a_c is an experimentally derived coefficient, t is the tip clearance, and b_1 and b_2 are the impeller blade heights at the inlet and exit, respectively (Eckert & Schnell, 1961).

Equation (1.4) provides a starting point for finding a relationship between the tip clearance gap and the decrease in efficiency, but it cannot be used without first experimental testing with a compressor. Multiple authors, such as Senoo and Ishida (1987) and Turunen-Saaresti and Jaatinen (2013), note that the coefficient *a* cannot be determined accurately because it is dependent on the specific compressor design. Other authors recommended a range for the coefficient but determining the exact value for a specific compressor requires experimental data.

A more simplified relationship given by several authors, such as Turunen-Saaresti and Jaatinen (2013), Pampreen (1973), and Lou et al. (2018), shows a direct linear correlation between the drop in efficiency and the tip clearance ratio

$$-\Delta\eta = k\Delta CR \tag{1.5}$$

where k is the slope of efficiency and ΔCR is the change in the clearance ratio, computed by dividing the tip clearance to the blade height, both at the impeller exit. In equation (1.5), only the slope of efficiency, which must be determined experimentally, is unknown. Pampreen (1973) suggested using a slope of one-third since there is about a one-third point loss in efficiency per percent clearance ratio, on average. Figure 1.4 illustrates this relationship between efficiency and clearance ratio. The left figure shows the efficiency on the ordinate while the right figure plots the efficiency drop from zero clearance. The abscissa of both figures is the clearance ratio. On the left, the linear trend in efficiency is shown between the two data points with a slope of -k, and the efficiency at a zero clearance is extrapolated. The figure on the right shows a different graphical representation of this trend using the efficiency drop from the extrapolated efficiency at a zero clearance. The magnitude of the slope is the same between both figures, but the right figure is more useful in comparing the tip clearance sensitivity between different speeds or different compressors because each set of data intersects the origin so the slopes become the main criteria for comparison.

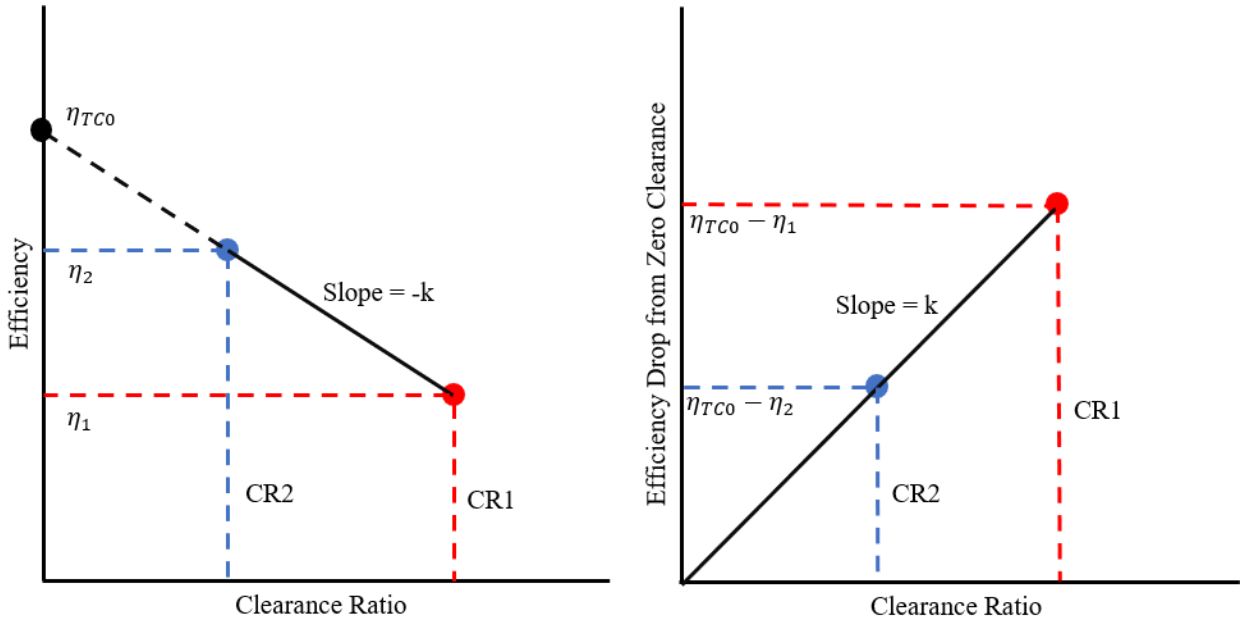

Figure 1.4 Linear tip clearance trend for efficiency

Turunen-Saaresti and Jaatinen (2013) compared the slope of efficiency to various other parameters, such as specific speed, blade height ratio, diffusion ratio, and blade number to attempt to find a linear relationship between efficiency drop and another parameter. However, they found that none of the correlations results in a distinct pattern to differentiate the decrease in efficiency with said parameters.

Brasz (1988) also identified a trend of total pressure ratio with changing tip clearance by collecting data at four different clearance ratio values. By plotting the total pressure ratio against the tip clearance ratio, the slope between the collected data points can be calculated, similar to left plot in Figure 1.4. As expected, the slope between the two smallest clearance ratios was the largest at -1.20 while the slope between the two largest clearance ratios was -0.51 and the middle slope was -0.67. Because the slope was steeper at lower tip clearances, the total pressure ratio is more significantly affected by changing tip clearances at smaller tip clearances.

The experimental and computational results presented by Kunte et al. (2012) also showed the trend of decreased total pressure ratio with increased tip clearance but the CFD overpredicted the effect of the tip clearance. Experimentally, there was a 1% reduction in total pressure ratio between the two tip clearances, but the CFD model predicted a 2% reduction. Tang et al.'s (2006) numerical results also showed that the trend of total pressure decreased approximately linearly and that when the tip clearance ratio is less than 15%, the total pressure decreases more quickly with the increase in tip clearance. Eum and Kang (2002) followed a similar procedure for total pressure ratio as they did with efficiency by calculating the total pressure drop from the zero tip clearance and also analyzing the contributions of the total pressure drop from work and entropy generation. While the efficiency drop was mainly due to the entropy generation, the total pressure drop contributions from work and entropy generation were approximately equal with the entropy generation having a slightly larger effect at small clearances and both contributions being approximately equal at larger tip clearances.

Empirical correlations for predicting the effects of tip clearance on a centrifugal compressor are challenging to derive because each compressor design will behave differently with a change in tip clearance. Attempting to predict the performance loss of a compressor is very challenging and most equations in literature require some experimental data to determine the slope or any constants in the equations.

1.5 Investigations into Flow Physics

The numerical studies that have been completed also sought to analyze the details of the flow field at various locations through a compressor for different tip clearances. Occasionally, this can be compared to experimental results if measurements are available at these locations, such as probe measurements in the flow path, laser doppler velocimetry (LDV) measurements, or particle image velocimetry (PIV) measurements.

Kunte et al. (2012) compared their experimental results with the pipe diffuser to their numerical results at the quasi-throat plane in the semi-vaneless space by using pitot probe measurements, at the diffuser exit plane by using Cobra probe measurements, and in the diffuser passage by using PIV results. Total pressure measurements taken at the quasi-throat plane, upstream of the diffuser throat and in the semi-vaneless space, near the peak efficiency operating point showed that there was a distinct area of maximum total pressure in the middle of the passage (the core flow) with total pressure losses in each direction. When comparing to the computational results, though, the core flow was predicted to be twice as large as it was in the experiment, and it appeared to be shifted slightly compared to the experiment. The maximum total pressure was predicted to be 1.5% less than the experimental data show. The tip clearance was then increased, and the same measurements were acquired, revealing that the maximum total pressure in the plane was reduced from the nominal clearance and the region of maximum total pressure was shifted towards the impeller inlet. These results were captured by the CFD simulation, though the reduction of maximum total pressure was overpredicted for the larger tip clearance. At the diffuser exit plane, the Mach number distribution resulting from the Cobra probe measurements showed that there existed a jet closer to the suction side of the diffuser while there is a large separation region on the pressure side. The CFD also predicted a jet flow in this area of the passage but it was closer to the suction side wall and closer to halfway between the front and back walls of the pipe diffuser whereas the experiment showed the jet was more towards the front wall. The larger tip clearance experimental results showed that the jet has shifted more towards the suction side and was larger in area. The authors explain that this is because the diffuser was not diffusing the flow as well as with the nominal clearance case. Their CFD simulation showed the same trends of increased jet flow and the maximum Mach number in the simulation was only 0.6% different from the maximum observed in the experiment. Lastly, PIV measurements in the diffuser passage were taken and compared the to the CFD prediction for both tip clearance cases. The results showed

that the flow was separating on the pressure side of the diffuser, which was observed at the diffuser exit. The CFD simulation correctly predicted the jet flow and the separation region but was not able to predict the magnitude of the velocities as well. At the throat and middle windows, the velocity was predicted between -1% and +5% of the experimental value and at the rear window, the velocity was consistently underpredicted by 10%. For the larger tip clearance case, the jet was shifted towards the pressure side of the diffuser, also in agreement with the results from the diffuser exit. The relative velocity dropped by up to 11% compared to the nominal configuration. The start of flow separation on the pressure side of the diffuser and the shift of the jet were also predicted by the CFD simulation however, the velocity reduction was only predicted to be 5% whereas the measured velocity deficit between the nominal and larger tip clearances was 11%. Overall, the steady CFD simulation was able to predict the larger features of the flow, such as the jet and separation of the flow, in the pipe diffuser and the trends associated with changing the tip clearance, but the magnitudes of the changes may not be representative of the experimental data (Kunte et al., 2012).

Tang et al. (2006) used their numerical investigation to focus on the flow inside the impeller and how a change in tip clearance affected the flow distribution. The simulation with no tip clearance showed that there existed a low-speed region on the inducer shroud of the impeller that occurs on either side of the splitter blade as well as a high-speed region on the suction side of the splitter blade near the leading edge. As the tip clearance became larger, the low-speed regions on either side of the splitter blade grew and the high-speed region near the leading edge shrunk because of the increased tip leakage flow. At the impeller exit, similar results are found with respect to increasing tip clearance and relative Mach number. The simulation showed that as the tip clearance increased, the low speed region in the shroud suction side corner of the passage grew and started to become a larger percentage of the passage flow. Because of this increase in size, the high-speed flow in the hub pressure side corner was compressed and accelerated resulting in less flow uniformity as tip clearance increases. Figure 1.5 illustrates these results of relative Mach number at the impeller trailing edge.

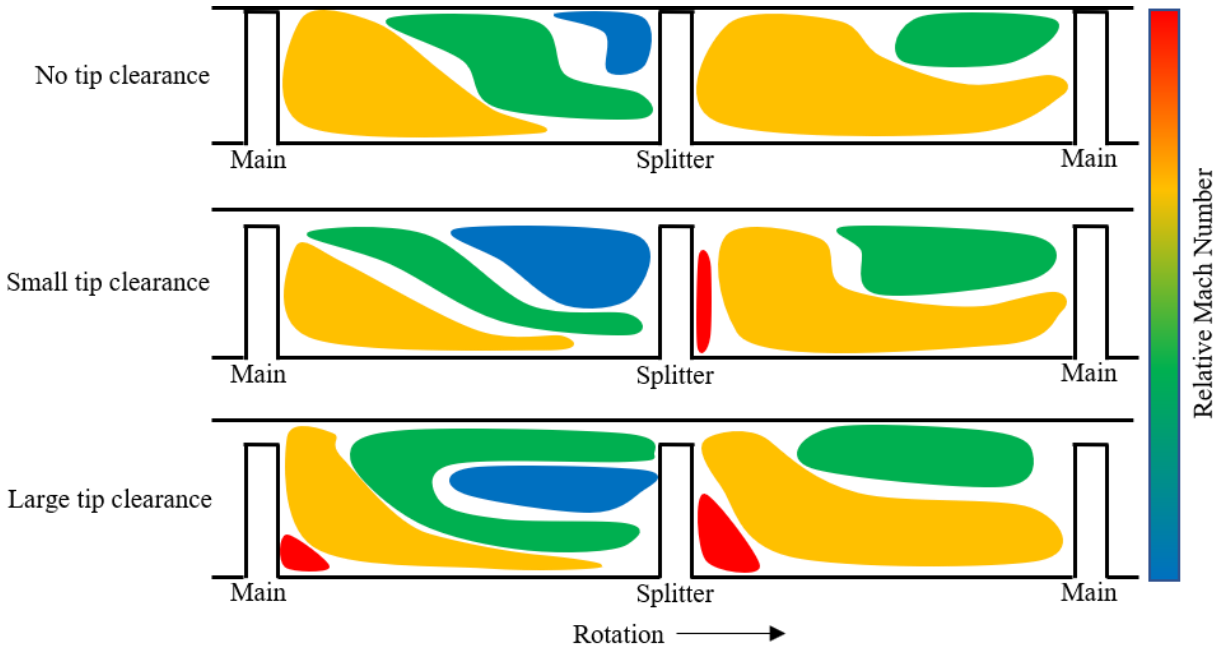

Figure 1.5 Graphic showing effects of tip clearance on impeller trailing edge relative Mach number from Tang et al. (2006)

Eum and Kang (2002) also used a numerical investigation to study the loss distributions at the impeller exit and how they are affected by the tip clearance. They found that for no tip clearance, most of the loss occurs near the shroud suction corner of the splitter blade. As the tip clearance increased, the high loss regions started to grow and extend into the main passage toward the pressure side hub corner. The loss distributions are very similar to Figure 1.5, where a low relative Mach number corresponds to a high loss region and low loss regions result in higher relative Mach numbers. This is reflected in the variations of total pressure and total temperature distributions through the impeller because larger tip clearances cause greater losses as the flow moves through the impeller.

Zhao, Wang, Ye, and Xi (2016) used the open data case of Krain's impeller to simulate the tip leakage vortex trajectory at design and off-design conditions. The impeller has a design mass flow rate of 4.7 kg/s, a total pressure ratio of 4.7, and a rotational speed of over 22,000 RPM resulting in subsonic conditions at the impeller inlet. Their results showed that as the loading condition of the compressor increased (and the mass flow rate decreased), the starting position of the tip leakage vortex moved upstream toward the leading edge of the main blade, and the angle with respect to the blade also increased with loading condition. Near the stall condition, the

interface between the main flow and the tip leakage flow was close to the leading edge of the main blade of the impeller.

1.6 Research Objectives

Tip clearance effects on stage performance of centrifugal compressors have been well documented experimentally, but compressor component analyses have rarely been performed. A component analysis is imperative to determining the source of losses due to tip clearance. The sensitivity of centrifugal compressor performance to tip clearance has also been presented with some researchers suggesting empirical correlations to predict the drop in efficiency with increasing tip clearance. Assessing the sensitivity of a compressor to changing tip clearance can aid in the design process as operating with a smaller tip clearance is preferred due to increased performance but poses challenges due to increased chances for tip rubs. A sensitivity analysis can also help in understanding the changes in performance over a long lifetime of a compressor as tip clearances will increase throughout the machine's lifetime due to wear. Several numerical studies have also been performed to assess the ability of computational tools to predict centrifugal compressor performance and the performance deficits due to the increasing tip clearance. These studies, while useful, have focused more on the impeller performance because of the use of a vaneless diffuser eliminating the interaction between the impeller and diffuser. A few of the computational studies do analyze the underlying flow physics and how the flow changes through the compressor with an increased tip clearance. Many challenges still exist, though, in trying to predict the effects and sensitivity of tip clearance in a centrifugal compressor.

The first portion of this research is to characterize the effects of tip clearance on the stage performance of the Honeywell Single Stage Centrifugal Compressor (SSCC) operated at Purdue and analyze the sensitivity of various performance parameters to tip clearance. Furthermore, a component analysis will be presented for both the impeller and diffuser to assess each component's losses and their corresponding sensitivity to changes in tip clearance. Data are collected at two different tip clearances, measured in real time, that are kept constant throughout the data collection at all rotational speeds and mass flow rates. This will create a high-quality dataset and analysis for a high-speed, high-pressure ratio centrifugal compressor designed for aeroengine applications.

Additionally, a numerical model for the SSCC was developed to aid in the understanding of the differences in flow physics with changing tip clearances. The steady model was developed

to assess the ability to predict stage performance, component performance, and sensitivities of the stage and components, all of which will be discussed in this thesis. Analysis of the results will reveal where the computational model fails to predict the performance of the stage or the components accurately as well as the flow mechanisms causing the tip clearance losses. The combination of the experimental data and numerical results will provide a valuable comparison for centrifugal compressors of this type as well as aid in the design process for future centrifugal compressors.

2. EXPERIMENTAL FACILITY AND COMPUTATIONAL APPROACH

2.1 Experimental Facility and Instrumentation

The experimental work was completed using the Honeywell Single Stage Centrifugal Compressor (SSCC) Facility at the Purdue High-Speed Compressor Laboratory. The SSCC is a high-speed, high-pressure ratio centrifugal compressor for use in aeroengine applications. The impeller consists of 17 main blades and 17 splitter blades, and the diffuser has 25 vanes. The design speed is near 45,000 RPM, the total pressure ratio is on the order of 6.5, and the machine Mach number is about 1.7. The first half of this chapter outlines the experimental facility, instrumentation, and data collection and analysis procedures used.

2.1.1 Purdue Single Stage Centrifugal Compressor (SSCC) Facility

All data presented for this research were collected using the SSCC facility with the axisymmetric inlet installed. Figure 2.1 shows the SSCC facility, which is an open loop design. Not shown in Figure 2.1 are the compressor and gearbox lubricating and cooling systems, secondary air system, and data acquisition systems.

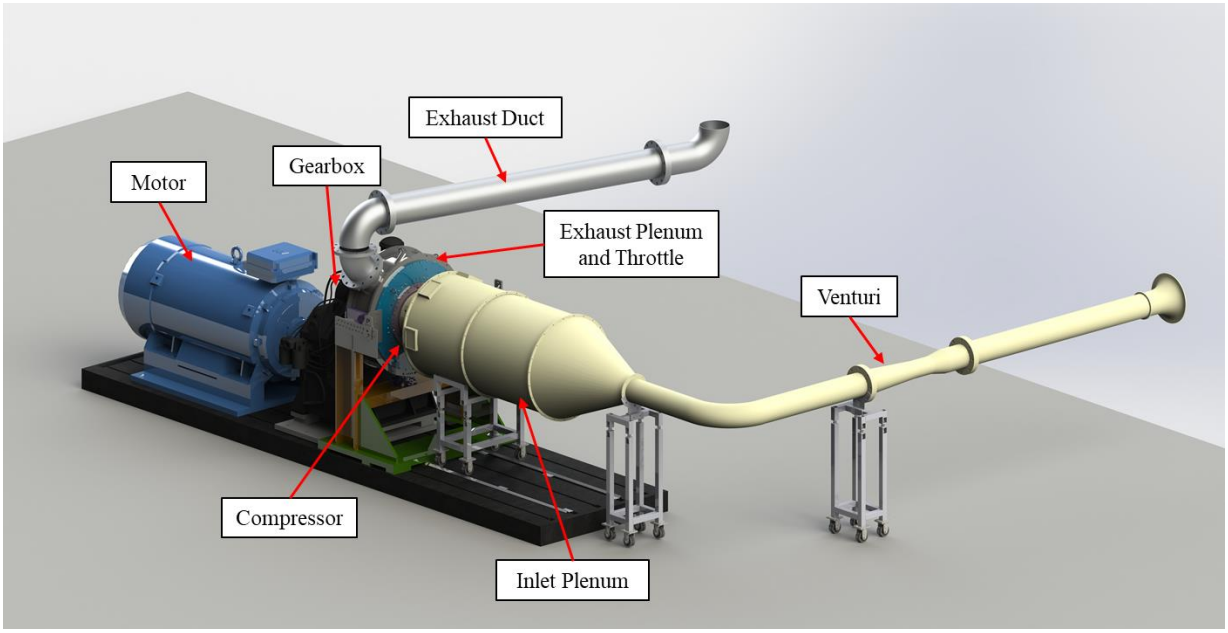

Figure 2.1 SSCC facility with axisymmetric inlet

The compressor is driven by a 1,400 HP AC electric motor through a speed-increasing gearbox with a gear ratio of 30.46:1. The electric motor is controlled by a variable frequency drive capable of controlling the speed within 0.01% of the desired value. The gearbox was manufactured by Cotta and has a maximum physical speed of 54,000 RPM, however the maximum speed tested with this compressor is 48,000 RPM. The gearbox output shaft is mated to a crowned spline shaft to allow for misalignment between the gearbox and the exhaust plenum. Through the middle of the exhaust plenum sits the torque tube, connecting the compressor to the spline shaft. The torque tube is meant to transfer power through the exhaust plenum but also isolate the compressor from the rest of the driveline by using squeeze film dampers and an axial spring to dampen the axial vibrations.

The facility has two separate lubricating and cooling systems, one for the gearbox and one for the compressor. Oil temperature, pressure and flow rate are monitored on the gearbox oil system supply lines as well as oil temperature in the high-speed bearings. The gearbox also has three accelerometers mounted on it for measuring vibrations in the vertical, horizontal, and axial directions. The crowned spline shaft that mates to the gearbox output shaft has proximity probes to measure the orbit of the crowned shaft.

The compressor oil supply system splits into four supply lines: one each for the torque tube, aft compressor bearing, forward compressor bearing, and slip ring. Pressure regulators for each line reduce the pressure to the appropriate range. The oil temperature, pressure, and flow rate are monitored on all supply lines as well as the temperature of each compressor bearing. Accelerometers are used on each of the four components to measure the vibrations and proximity probes are used on the compressor shaft to measure the shaft orbit.

Air is brought in from a large settling chamber through a bellmouth to transition the flow to an 8-inch diameter duct. The duct feeds the ASME long-form standard venturi used to measure the mass flow rate into the compressor. After flowing through a 90-degree elbow, the air then enters the inlet plenum, which contains multiple flow conditioners. The diagram in Figure 2.2 depicts a layout of the inlet plenum and the flow conditioners inside. The air first passes through a flow spreader to evenly distribute the flow as the diameter increases and then through two honeycomb screens to straighten the flow before entering the compressor. This inlet is designed to provide distortion-free inlet flow to the compressor.

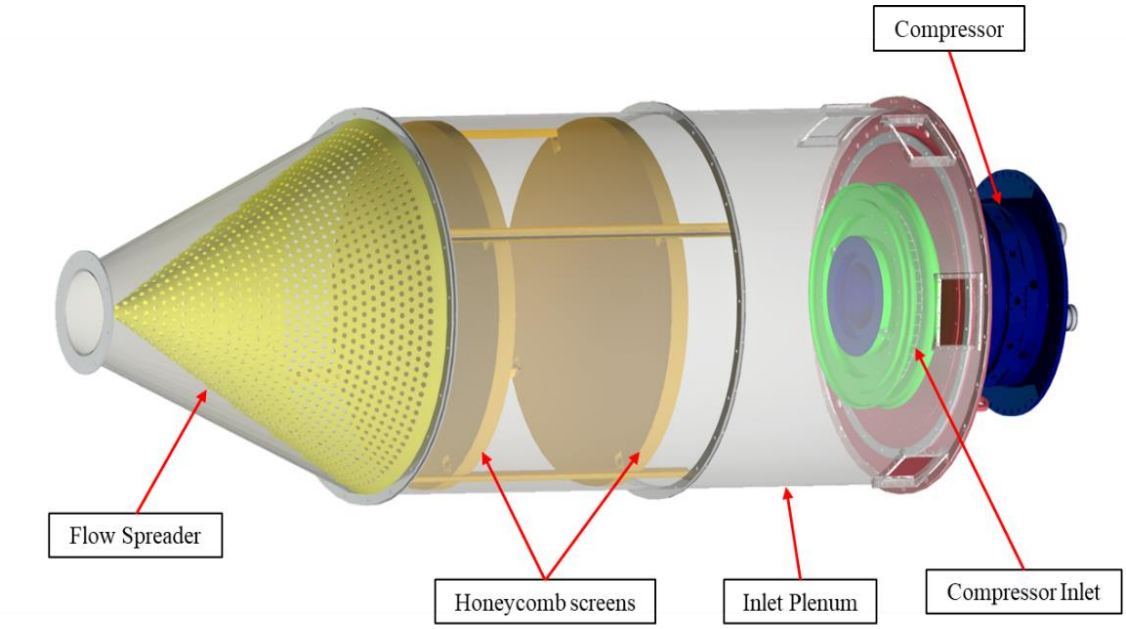

Figure 2.2 Inlet plenum flow conditioners

As the compressor is designed for use in aero engine applications, the inflow to the compressor is radial to best imitate use on an actual engine. The flow turns to axial inside the inlet housing and enters the impeller, which turns the flow back to radial. The flow stays radial through the stationary diffuser but makes a final turn back to axial to go through the bend and deswirl before exiting the compressor. A meridional view of the flow path through the compressor stage is shown in Figure 2.3.

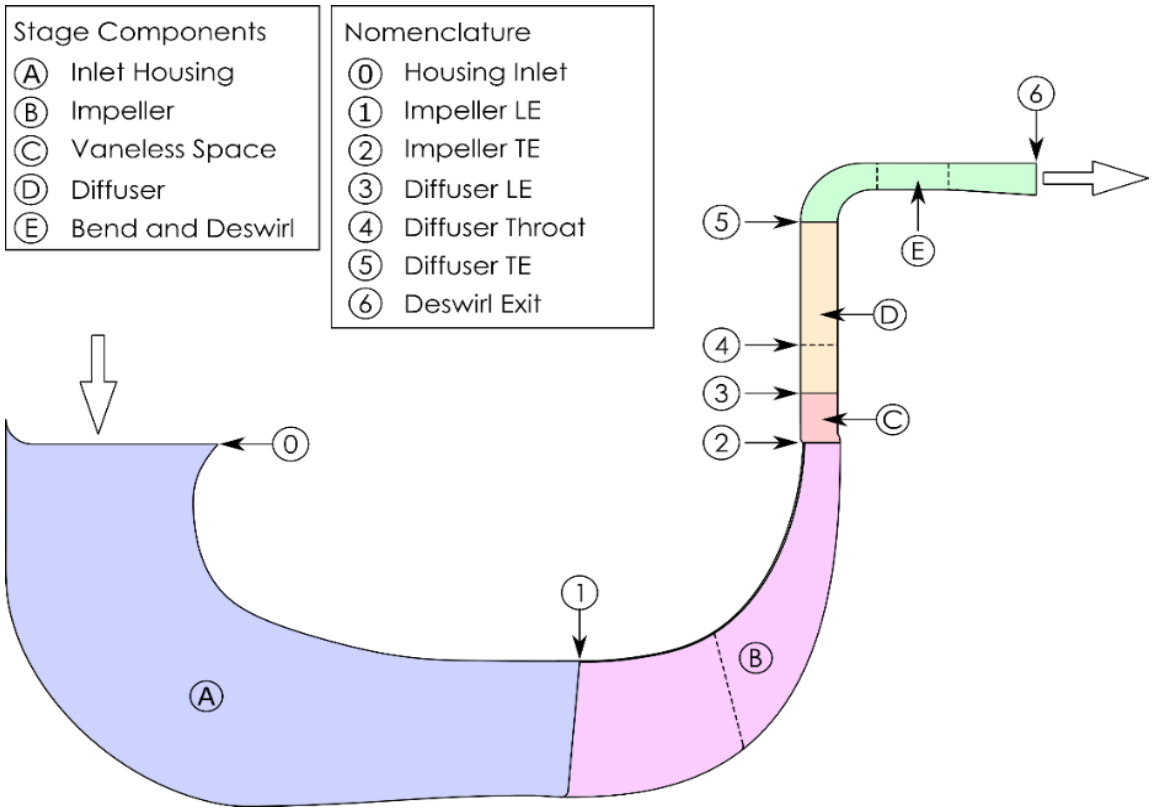

Figure 2.3 Compressor flow path meridional view

2.1.2 Compressor Instrumentation

The compressor flow path is outfitted with instrumentation in the inlet, impeller, diffuser, and deswirl. These measurements are used to calculate both stage and component performance parameters, which will be discussed in Sections 2.1.3 and 2.1.4. Figure 2.4 shows the meridional view of the stage with the steady instrumentation locations overlaid at approximate locations in each component.

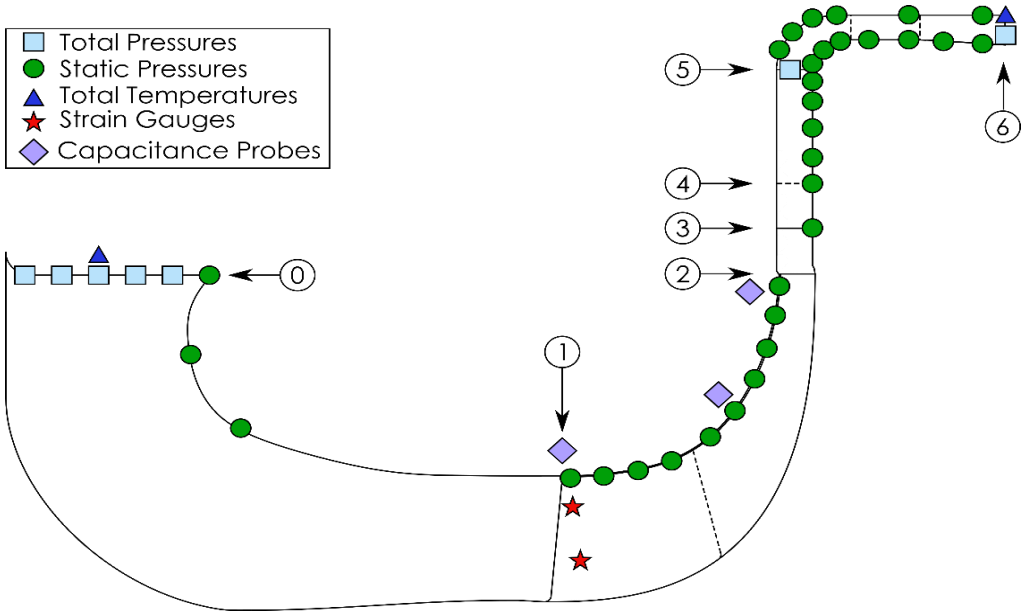

Figure 2.4 Steady instrumentation overview

There are four inlet rakes equally spaced circumferentially (at station 0) that each have five total pressure elements and a total temperature element. Total pressure and total temperature values from these rakes are used for the calculations to correct the mechanical speed and mass flow rate to standard day conditions.

In the impeller, there are ten static pressure taps at the same circumferential location and equally spaced along the shroud to provide the static pressure rise through the impeller. There are three additional static pressure taps at the leading edge location that are equally spaced circumferentially. At the trailing edge, there are nine additional static pressure taps around the circumference of the impeller. To provide an accurate leading and trailing edge static pressure, each set of measurements is area averaged. Overall, the instrumentation in the inlet housing and impeller is summarized in Table 2.1.

Table 2.1 Steady instrumentation in inlet housing and impeller

	Total Pressure	Total Temperature	Static Pressure
Quantity	20	4	28

Impeller tip clearance is measured by 12 capacitance probes, four each located circumferentially at the inducer (inlet), the knee (middle), and exducer (exit) of the impeller. Tip clearance measurements are averaged at each location to provide a representative tip clearance. In addition, the raw signal of each capacitance probe is available to examine the confidence of the tip clearance readings. If it is determined that the raw signal is not suitable for use, the measurement from that probe can be excluded from the average in LabView. The tip clearance can be changed by moving the rotating group axially with a high-precision stepper motor that can provide adjustment within 0.0001 inches.

The diffuser is instrumented with static pressure measurements in three passages, except for the diffuser leading edge static pressure taps, which are in various passages and at different pitchwise locations. Each of the three diffuser passages has three static pressure taps across the diffuser throat, four static pressure taps in the streamwise direction, three static pressure taps covering the exit, and three static pressure taps at the trailing edge. The static pressure passage instrumentation is illustrated in Figure 2.5. There are also six total pressure rakes in the diffuser, located at three different pitchwise locations. The rakes are placed at radial locations just behind the diffuser trailing edge static pressure taps.

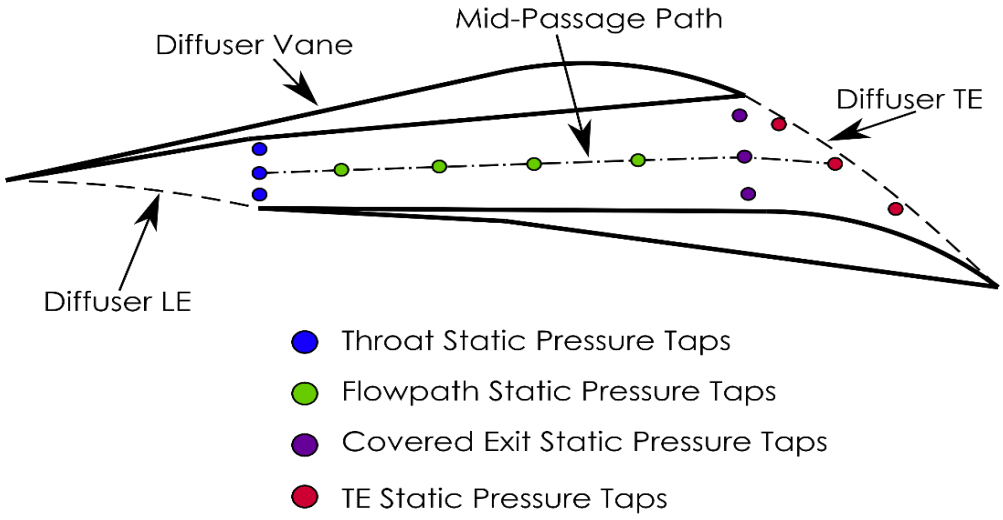

Figure 2.5 Static pressure measurements in the diffuser

The diffuser leading edge static pressure measurement locations are spread circumferentially around the annulus corresponding to a variety of diffuser passages. There is one

measurement each at 10%, 20%, 30%, 40%, 50%, 60%, 70%, 80%, and 90% pitch. The steady measurements in the diffuser are summarized in Table 2.2.

Table 2.2 Steady instrumentation in diffuser

	Total Pressure	Static Pressure
Quantity	18	56

Instrumentation in the bend and deswirl consists of static pressure taps throughout and the exit rakes, which are used for stage performance calculations. There are eight deswirl exit total pressure rakes, each with three elements, located at four unique pitchwise locations with respect to the deswirl blade. There are also four deswirl exit total temperature rakes, each also containing three elements and located at four unique pitchwise locations with respect to the deswirl blade. The bend and deswirl instrumentation is summarized in Table 2.3.

Table 2.3 Steady instrumentation in the bend and deswirl

	Total Pressure	Total Temperature	Static Pressure
Quantity	24	12	36

The data acquisition system is controlled through LabView for all health monitoring, steady performance, and unsteady data collection. Two Scanivalve DSA 4000 enclosures housing 16 DSA3016 pressure modules measure all the steady pressures. The inlet housing pressures are measured with a module with a range of either 2.5 psid or 5.0 psid, and all other pressures are measured using modules with a 100 psid range. The uncertainty is ±0.12% full scale for the modules with a range of 2.5 psid and ±0.05% full scale uncertainty for the modules with ranges of 5.0 psid and 100 psid. An Agilent 34980 enclosure measures the voltage signals from the capacitance probe conditioning system, thermocouples, pressure transducers, and a relative humidity sensor. Temperature measurements are taken with an uncertainty of 2.2°C. More details regarding the facility, the setup, and preliminary testing can be found in Lou (2016).

2.1.3 Stage Performance Analysis

The stage total pressure ratio is calculated by

$$TPR = \frac{P_{06}}{P_{00}} \tag{2.1}$$

where the measured total pressure at the deswirl exit, denoted by station 6, is divided by the inlet total pressure measured at station 0, with station numbers referenced to Figure 2.3. The elements on each total pressure rake were area-averaged first, and then each rake was area-averaged to provide a representative mean for total pressure at each station.

The stage total temperature rise ratio is calculated like the stage total pressure ratio. The total temperature rakes were averaged at the inlet and the deswirl exit and used to calculate the stage total temperature rise ratio

$$TTR = \frac{T_{06} - T_{00}}{T_{00}} \tag{2.2}$$

where the difference in total temperature between the inlet and deswirl exit divided by the inlet total temperature.

Stage isentropic efficiency is calculated as the ideal work divided by the real work, using the enthalpies at the inlet and exit of the compressor

$$\eta = (h_{06,s} - h_{00})/(h_{06} - h_{00}) \tag{2.3}$$

with the subscript s representing the enthalpy calculated assuming isentropic work. The total enthalpy information at the inlet and deswirl exit was retrieved via REFPROP using the total temperature and total pressure as well as the mass fraction of air, assuming dry air composition of nitrogen, oxygen, argon, and carbon dioxide and including the amount of water vapor in the air, calculated using the relative humidity measured from the experiment. The inlet entropy was also calculated in the same way. The isentropic enthalpy at the deswirl exit was then calculated using REFPROP by specifying the exit total pressure and the inlet entropy.

A venturi flow meter with a calibrated discharge coefficient of 0.992 is used to calculate the mass flow rate through the compressor

$$\dot{m} = \frac{\pi}{4}\, d^2 C_d \epsilon X \sqrt{\frac{2\rho(\Delta P)}{1-\beta^4}} \tag{2.4}$$

with supporting equations (2.5) - (2.7)

$$\epsilon = \sqrt{\left(\frac{\gamma}{\gamma-1}\right)\left(\frac{P_{throat}}{P_{upstream}}\right)^{\frac{2}{\gamma}}\left(\frac{1-\left(\frac{P_{throat}}{P_{upstream}}\right)^{\frac{\gamma-1}{\gamma}}}{1-\frac{P_{throat}}{P_{upstream}}}\right)} \tag{2.5}$$

$$X = \sqrt{\frac{1-\beta^4}{1-\beta^4\left(\frac{P_{throat}}{P_{upstream}}\right)^{\frac{2}{\gamma}}}} \tag{2.6}$$

$$\beta = \frac{D_{throat}}{D_{inlet}} \tag{2.7}$$

The pressure is measured upstream of the throat and the differential pressure between the throat and upstream of the throat is also measured. The throat pressure is then calculated by subtracting the differential pressure from the upstream pressure. In equation (2.4), d is the throat diameter and equation (2.7) defines a ratio of the throat diameter to the upstream, or inlet, diameter. The diameters (and the ratio) are corrected for thermal expansion using thermocouples mounted on the venturi inlet and throat. Corrected mass flow rate (corrected to standard day conditions) is calculated with equation (2.8)

$$\dot{m}_{corr} = \frac{\dot{m}\left(\rho_{ref} a_{ref}\right)}{\rho_{00} a_{00}} \tag{2.8}$$

using the area-averaged total temperature and total pressure from the inlet rakes at station 0 and REFPROP to calculate the density and the speed of sound at station 0. The values of ρ_{ref} and a_{ref}

are calculated assuming a reference temperature and pressure of 59°F and 14.7psi, respectively and zero relative humidity. This method accounts for the changes in properties due to relative humidity. More information can be found in Berdanier et al. (2015).

Finally, the work factor for the stage is calculated with equation (2.9)

$$\psi = (h_{06} - h_{00})/U_2^2 \tag{2.9}$$

where the total enthalpy at the inlet and exit of the stage is calculated using REFPROP with the area-averaged total temperature and total pressure at each station and the air mass fraction. The work factor provides a measure of the work done by the stage divided by the potential work available.

2.1.4 Component Performance Analysis

Component performance can be divided into two main parts, the impeller and the diffuser. A component analysis is critical to understanding the effects of tip clearance and which components are the most sensitive to changes in tip clearance. An overview of the various parameters used to characterize the performance of each component is given in this section.

Many of the impeller performance quantities use the impeller exit total pressure. Because the static pressure is the only quantity measured at the impeller exit, the impeller exit total pressure can only be solved for by using an iterative procedure from conservation of mass and the Euler turbomachinery equation with the assumption of a constant blockage factor at the impeller exit. An adiabatic process is assumed through the diffuser and deswirl so that the deswirl exit total temperature is equal to the impeller exit total temperature. First, the impeller exit tangential flow velocity ($V_{\theta 2}$) is calculated from equation (2.10)

$$h_{06} - h_{00} = U_2 V_{\theta 2} - U_1 V_{\theta 1} \tag{2.10}$$

which is the Euler turbomachinery equation. In the axisymmetric inlet configuration, the tangential velocity at the inlet to the impeller ($V_{\theta 1}$) is assumed to be zero. The enthalpies are calculated as before, using REFPROP with total pressure, total temperature, and air mass fraction. The effective area at the impeller exit is then calculated using equation (2.11)

$$A_{eff,2} = 2\pi R(b_w + Cl_{ax})K_{bar} \tag{2.11}$$

where b_w is the blade height, Cl_{ax} is the impeller axial clearance measured during testing, and K_{bar} is the blockage factor. The assumed value for the blockage factor is 0.9 for all data presented, but a variation of 0.87 to 0.93 was also used to assess the magnitude of the effect on the processed parameters. This will be discussed in Chapter 3.

The iterative process uses equations (2.12) - (2.15)

$$V_{m2} = \frac{\dot{m}}{\rho_2 A_{eff,2}} \tag{2.12}$$

$$V_{abs,2} = \sqrt{V_{\theta 2}^2 + V_{m2}^2} \tag{2.13}$$

$$M_2 = \frac{V_{abs,2}}{\sqrt{\gamma_2 R T_2}} \tag{2.14}$$

$$h_2 = h_{02} - \frac{1}{2}V_{abs,2}^2 \tag{2.15}$$

where equation (2.12) defines the meridional component of velocity. To start each iteration, ρ is calculated using the measured deswirl exit total temperature and the area-averaged static pressure at the impeller trailing edge input into REFPROP with the air mass fraction. The local speed of sound is also calculated using REFPROP with the area-averaged static pressure at the impeller trailing edge, the density, and the air mass fraction. After that, the process is completed using the order of the equations above. This process is repeated but with an updated value for density using the enthalpy at the impeller trailing edge instead of the total temperature at the deswirl exit. This yields two calculations of the Mach number of the flow at the impeller trailing edge which are compared to compute a tolerance. The iteration continues until a value for the impeller exit Mach number is converged upon. The iteration is complete once the tolerance (difference in Mach numbers calculated each iteration) is less than 0.0001.

Once a converged value of impeller exit Mach number has been found, the total pressure at the impeller exit can be calculated using the final values for static enthalpy and area-averaged

impeller trailing edge static pressure by inputting those values into REFPROP along with the mass fraction of air.

The impeller total pressure ratio can then be calculated in the same way as the stage total pressure ratio. The total temperature is assumed to be constant through the diffuser and deswirl meaning that the impeller total temperature rise ratio is the same as the stage total temperature rise ratio. The impeller efficiency is also calculated the same way as the stage efficiency but using the total temperature and total pressure at the impeller exit instead of the stage exit to calculate the corresponding enthalpies using REFPROP.

In the diffuser, the main performance metrics relate to the static pressure recovery and the total pressure loss through the component. All equations for the analysis of the diffuser can be found in Japikse and Baines (1998). The static pressure recovery coefficient is defined such that a value of unity would be recovery of all total pressure into static pressure for that component. The static pressure recovery coefficient for the diffuser is defined in equation (2.16)

$$C_p = \frac{P_5 - P_2}{P_{02} - P_2} \tag{2.16}$$

with the station numbers corresponding to those in Figure 2.3. The total pressure loss through the diffuser can be calculated by equation (2.17)

$$K = \left| \frac{P_{05} - P_{02}}{P_{02} - P_2} \right| \tag{2.17}$$

And finally, diffuser effectiveness can be calculated by using equation (2.18):

$$\eta_{diff} = \frac{C_p}{C_{p,ideal}} \approx \frac{C_p}{C_p + K} \tag{2.18}$$

where the ideal static pressure recovery coefficient is approximated as the addition of the actual static pressure recovery coefficient and the total pressure loss coefficient.

All three of the diffuser parameters will be affected by the blockage factor from the impeller total pressure calculation because the static pressure recovery and total pressure loss coefficients are both normalized by the impeller dynamic pressure. The total pressure loss

coefficient will also be affected by that calculation in the numerator when determining the total pressure loss through the diffuser. In this case, the impeller total pressure ratio and impeller efficiency will increase with an increased blockage (decreased K_{bar}) while the diffuser total pressure loss will decrease, leading to a balance between the two parameters based on the choice of blockage factor.

2.1.5 Compressor Operating Conditions

Compressor performance data were collected at seven different corrected speeds (60%, 70%, 80%, 85%, 90%, 95%, and 100%) and at two different tip clearances for each speed. Corrected speed is calculated with equation (2.19)

$$N_{corr} = \frac{N_{mech}}{a_{00}/a_{ref}} \tag{2.19}$$

which can be reversed to calculate the mechanical speed required to meet a certain corrected speed on a given day. The reference speed of sound is calculated by inputting the reference temperature of 59°F, the reference pressure of 14.7psi, and no relative humidity into REFPROP. The speed of sound at station 0 is calculated similarly but with the total temperature and total pressure measured at station 0 and the relative humidity measured during the experiment. More information about this correction can be found in Berdanier et al. (2015).

Two different axial tip clearances were tested to compare the performance and trends. The nominal axial tip clearance and a tip clearance with a 66.67% increase were both tested. When comparing the size of the tip clearance to other published results, though, the tip clearance divided by the blade height (t/b_2) at the impeller exit is typically used. The axial tip clearances tested on the SSCC correspond to tip clearance ratios of 4.46% for the nominal tip clearance and 7.44% for the larger tip clearance.

The normalized total pressure ratio map for the seven speedlines at each tip clearance is shown in Figure 2.6, and the efficiency map is shown in Figure 2.7. Data were acquired to the surge point for the larger tip clearance speedlines whereas, in general, data were only taken to a few points past peak efficiency for the nominal tip clearance. The “X” inside the data marker on the orange speedlines represents the last steady point taken before surge occurred. All data were

normalized using the values at design point, which is the peak efficiency point using nominal tip clearance at 100% corrected speed.

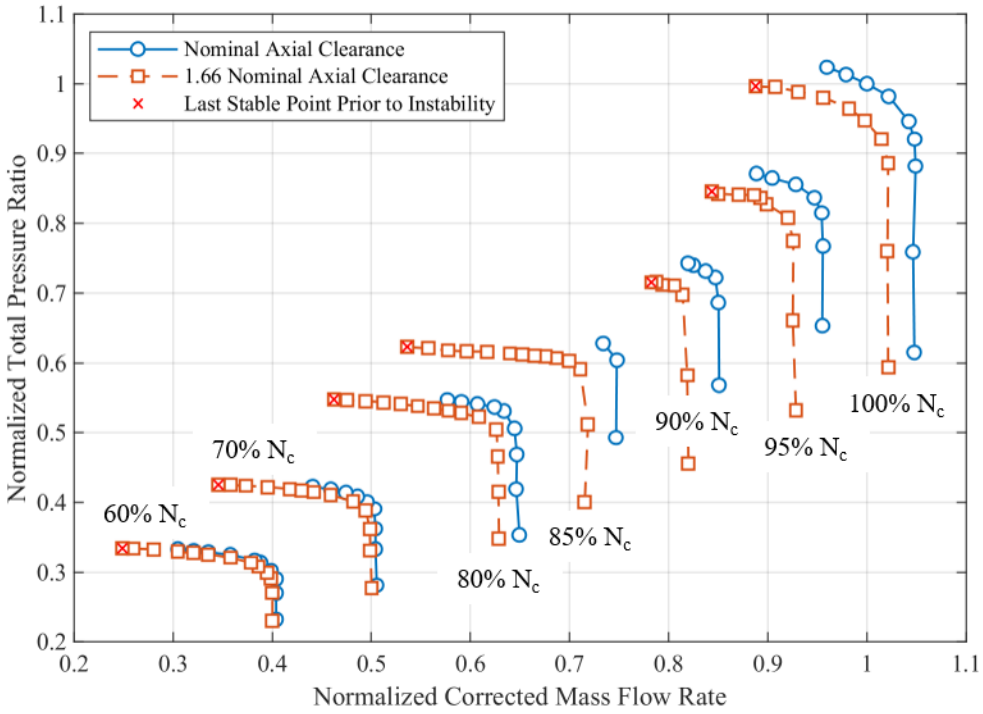

Figure 2.6 Normalized total pressure ratio compressor map

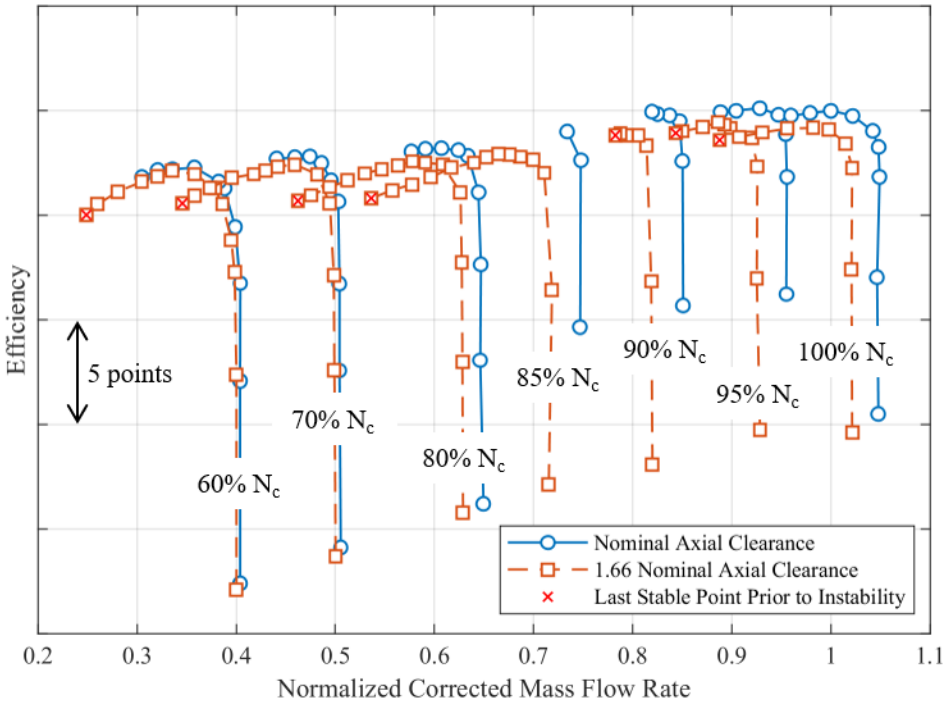

Figure 2.7 Efficiency compressor map

The experimental data shown in Figure 2.6 and Figure 2.7 were used to conduct analyses of tip clearances trends and sensitivity because such analyses required multiple speeds. However, when comparing the experimental data to the numerical simulations, only the 100% speedline was computed and will be the focal point of the comparison between experiment and CFD.

2.2 Computational Model Development

A computational model was developed to simulate the SSCC at the two tip clearances and assess the performance of the model in predicting the effects of tip clearance. ANSYS CFX, a commercially available CFD software, was used for all setup and simulations. The ANSYS CFX software suite contains ANSYS TurboGrid, used for generating meshes for each domain, CFX-Pre, used to import the meshes and define all boundary conditions, interfaces, and solver conditions, CFX Solver, which solved the simulation, and CFD-Post, where the results were loaded after the simulation completed and the results could be processed.

ANSYS TurboGrid was used for meshing the domains because it is specifically designed for rotating machinery simulations. Three .curve files (one each for the hub, the shroud, and the blade profiles of each domain) are used for each domain to import the geometry into the software. The SSCC .curve files are split into three domains, the impeller (which includes the inlet housing), the diffuser, and the deswirl. The software automatically selects a topology to use for the grid generation based on the geometry, and then, various parameters can be set to determine the mesh. The option to include an inlet and outlet domain as part of the mesh is included and used to generate the mesh in the inlet section of the impeller domain. A target mesh size is specified, as well as settings for boundary layer refinement control. The 3D mesh is then generated using these settings and can be saved and imported into CFX-Pre for implementation into the entire simulation.

As stated earlier, CFX-Pre is used to combine all meshes and set boundary conditions and domain interfaces, which will be detailed for each domain. The CFX Solver conditions are also set in CFX-Pre before the simulation is executed using the CFX Solver. The SSCC simulations were solved using the Purdue University Research Computing clusters. Finally, CFD-Post was used for post processing of the results. The results file is loaded into the software where the results could be analyzed and exported for use in other programs, such as MATLAB.

2.2.1 Discretization and Boundary Conditions

The SSCC was divided into three main domains for the numerical simulation, the inlet and impeller, the diffuser, and the deswirl. Figure 2.8 shows the entire domain being used in ANSYS for the simulations. All the presented images of the ANSYS model are skewed to obscure the geometry. The first domain shown includes the inlet and the impeller, which were meshed in the same TurboGrid file. The inlet of the computational domain is located at station 0 in Figure 2.3, where the inlet rakes are located so that standard corrected conditions (total temperature equal to 59°F and total pressure equal to 14.7 psi) could be used for the inlet boundary condition, and the rotational speed used could be the design speed at corrected conditions. An outlet domain extends approximately twelve deswirl main blade chord lengths downstream. The outlet domain was added to the end of the deswirl to allow any wakes to dissipate before the domain exit. The outlet domain was meshed with cells that slightly increase in size from the deswirl to the end of the domain to facilitate the dissipation of the wakes. The outlet boundary condition used was either a mass flow rate condition or a static pressure condition. A mass flow rate boundary condition was used through

the upper half of the speedline while the static pressure condition was used in the lower half of the speedline, in the choke condition.

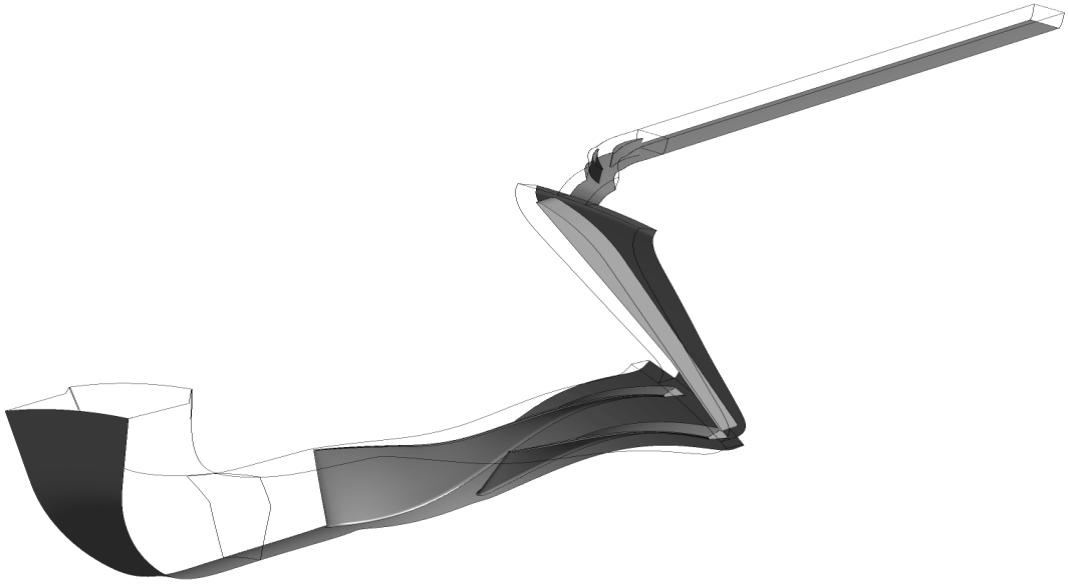

Figure 2.8 SSCC geometric domain

The hub and blades of each domain are modeled as adiabatic, no slip walls with a specified roughness, except for the outlet domain, which was modeled with smooth walls. This choice was made because the outlet domain was added for computational purposes only, so it was desired to be an ideal wall that introduced as little loss as possible to the flow.

Air modeled as an ideal gas is being used for all simulations. Discussion on the differences between using air modeled as an ideal gas and air modeled as a perfect gas is in the Appendix. For ideal air properties, the NASA format for the polynomial curve fits for specific heat, static enthalpy, and static entropy is being used and the format for each is listed in equations (2.20) - (2.22)

$$\frac{C_P^0}{R} = a_1 + a_2 T + a_3 T^2 + a_4 T^3 + a_5 T^4 \tag{2.20}$$

$$\frac{H^0}{R} = a_1 T + \frac{a_2}{2} T^2 + \frac{a_3}{3} T^3 + \frac{a_4}{4} T^4 + \frac{a_5}{5} T^5 + a_6 \tag{2.21}$$

$$\frac{S^0}{R} = a_1 lnT + a_2 T + \frac{a_3}{2}T^2 + \frac{a_4}{3}T^3 + \frac{a_5}{4}T^4 + a_7 \tag{2.22}$$

with the values for the coefficients listed in Burcat and Ruscic (2005).

Surface roughness was included in the numerical model for all surfaces, except the outlet domain. The centerline average roughness (R_a) for each component was specified on the corresponding drawing. However, surface roughness in ANSYS CFX-Pre is specified as equivalent sand grain roughness. The sand grain roughness model is a model consisting of spheres of a certain radius that provide the same effects on the boundary layer as a real surface (Hummel et al., 2005). Rather than being a directly measurable quantity, the sand grain roughness model is used for computational purposes only, and the equivalent sand grain roughness must be computed from the centerline average roughness using a correlation of the form

$$k_s = A\, R_a \tag{2.23}$$

where k_s is the sand grain roughness, A is a constant, and R_a is the centerline average roughness.

Because there is no universal roughness correlation, four different correlations were averaged to determine the equivalent sand grain roughness. Bunker (2003) used an value of 10 for A because he suggested that values range from 2 to 10 and he wanted to take the conservative approach. Shabbir and Turner (2004) suggested a value of 8.9 for their tests on a linear compressor cascade. Koch and Smith (1976) used a value of 6.2 for determining the sand grain roughness when modeling axial compressors. And, Hummel et al. (2005) performed a parametric study to find the roughness value that matched the trend of their experimental data the best and found a constant of 5.2 for A. Averaging these four values together gives an A value equal to 7.575 that was used to convert the centerline average roughness to equivalent sand grain roughness for use in the CFX simulations.

A turbulence model and heat transfer were both incorporated into the model. The turbulence model used for all simulations is the BSL turbulence model, which is a model that combines the $k-\omega$ model for use near surfaces and the $k-\epsilon$ model in the freestream region (*ANSYS CFX-Solver Theory Guide*, 2019). Heat transfer in the model was determined by setting the shrouds of the impeller and the diffuser to a fixed temperature. To measure the temperature along the impeller shroud, there are six embedded thermocouples in the impeller shroud, two at

the leading edge, two at the knee, and two at the trailing edge. For an experimental data point, a linear curve fit with respect to radius was applied to the temperatures from these thermocouples. The linear equation for temperature as a function of radius was used calculate the temperature at all points along the shroud in ANSYS to impose the wall temperature boundary condition. This process was completed for each experimental data point because the shroud temperature changes significantly along a speedline, so a new shroud temperature boundary condition was generated for each data point. An example of the shroud temperatures and the corresponding linear function is illustrated in Figure 2.9. The wall temperature of the shroud of the diffuser was also specified but as there are no thermocouples in the shroud, the temperature was assumed to be slightly lower than the impeller trailing edge temperature because it is a uniform boundary condition. The deswirl hub and shroud are both exposed to the dump area where the hot air collects and exits through the exhaust plenum. Due to the small thickness of the hub and shroud and the hot air surrounding both, the walls are assumed to be adiabatic in the numerical model.

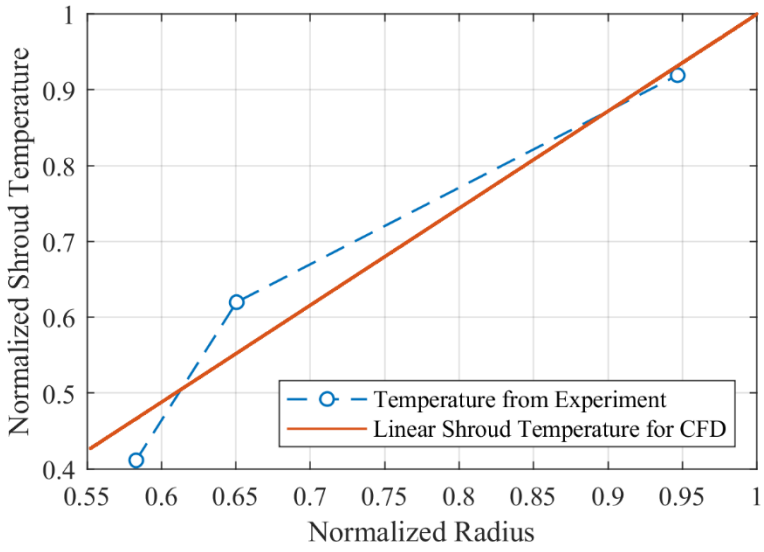

Figure 2.9 Impeller shroud temperature linear function example

Lastly, the tip clearance was changed by altering the impeller shroud .curve file to match the capacitance probe measurements from the experiment with the closest point in the .curve file. Between the locations of capacitance probe measurements, the tip clearance was assumed to have a linear trend. The impeller shroud .curve file was then altered to account for the change in tip

clearance by moving each point the correct amount based on the capacitance probes and the linear trend. Once the impeller .curve files were loaded into TurboGrid, the tip clearance region was treated separately from the main flow so that the number of elements between the top of the blade and the shroud could be specified.

2.2.2 Domain Interfaces

All simulations presented here were completed using a steady state analysis in the ANSYS software leading to certain domain interfaces being required. Because the simulation is steady state, a frame/pitch change model is required so that a domain that is rotating can be interfaced with a domain that is stationary. A model is also required for a pitch change, where the angular pitch changes from one domain to the next. The frame/pitch change model used for these simulations is the Mixing-Plane model. This model does not assume a fixed relative position of two components (such as the Frozen Rotor model) but instead, circumferentially averages the fluxes leaving one domain along different circumferential bands and uses that as the inlet condition for the next domain (*CFX-Solver Modeling Guide*, 2019). The highlighted planes in Figure 2.10 show the domain connections being used in the model. The three blue planes represent where the Mixing-Plane model is being implemented. The first is where the stationary inlet domain connects to the rotating impeller domain because there is a frame change. The second is where the rotating impeller domain connects to the stationary diffuser domain because there is a frame change and a pitch change. And the third is where the stationary diffuser domain connects to the stationary deswirl domain, which does not contain a frame change but only a pitch change. The green plane shown in Figure 2.10 represents a general connection between the deswirl domain and the outlet domain. The general connection being utilized here is only to connect the two domains and does not contain any frame change or pitch change models.

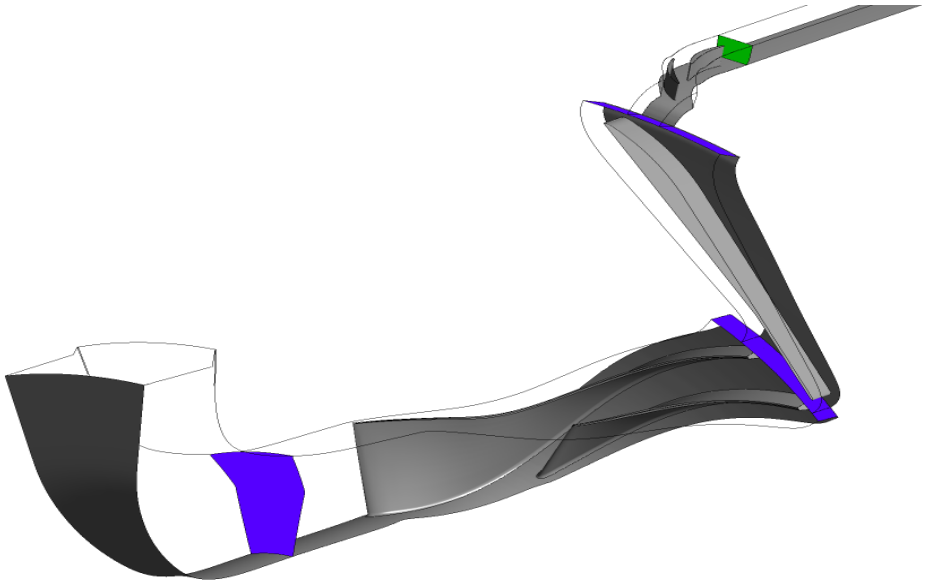

Figure 2.10 Domain connections in SSCC numerical model

To reduce the computational time required even further, only one passage per domain was simulated. A rotational periodicity boundary condition was applied on either side of each domain and the specification of how many passages per domain was made so that the solver knew angular pitch of each domain. Figure 2.11 shows the periodic interfaces in the numerical model colored in blue.

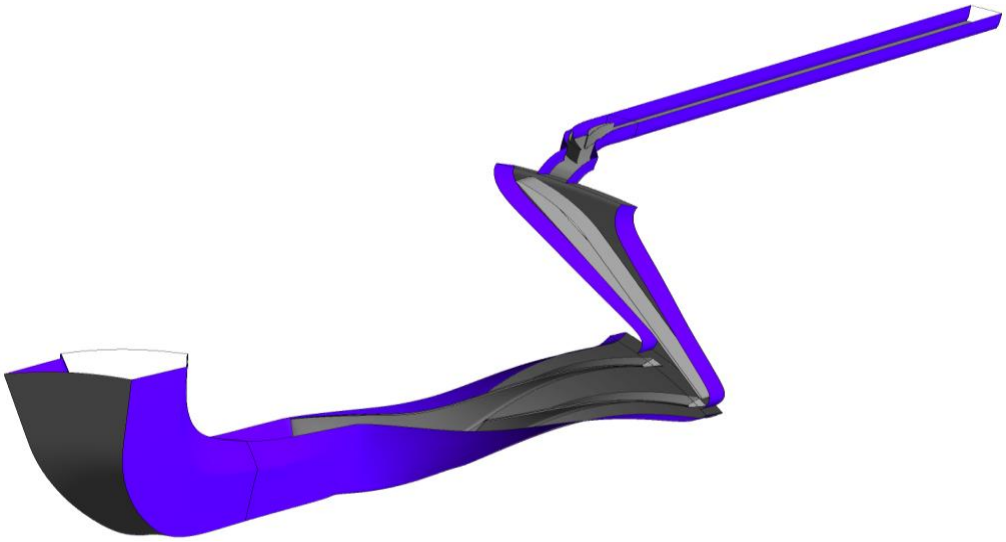

Figure 2.11 Periodic interfaces in SSCC numerical model

2.2.3 Experimental Measurement Locations

To make a fair comparison between the experimental data and the numerical results, the locations of instrumentation from the experiment were input into the CFD software. Static pressure taps and total pressure and total temperature elements were simulated at the correct locations and the results from the numerical simulation at those locations were then used in the same processing methods that are used for experimental data. While this was a nontrivial process, it was essential to be able to provide the best comparison possible between the experiment and the CFD.

Figure 2.12 shows the location of all the steady instrumentation being used for this study. Because the compressor has been modeled as one passage per domain, there will be no circumferential variation in the numerical results. Experimentally, locations with multiple static pressure taps or total pressure or total temperature elements were averaged around the circumference to provide a representative mean value for comparison with the numerical results.

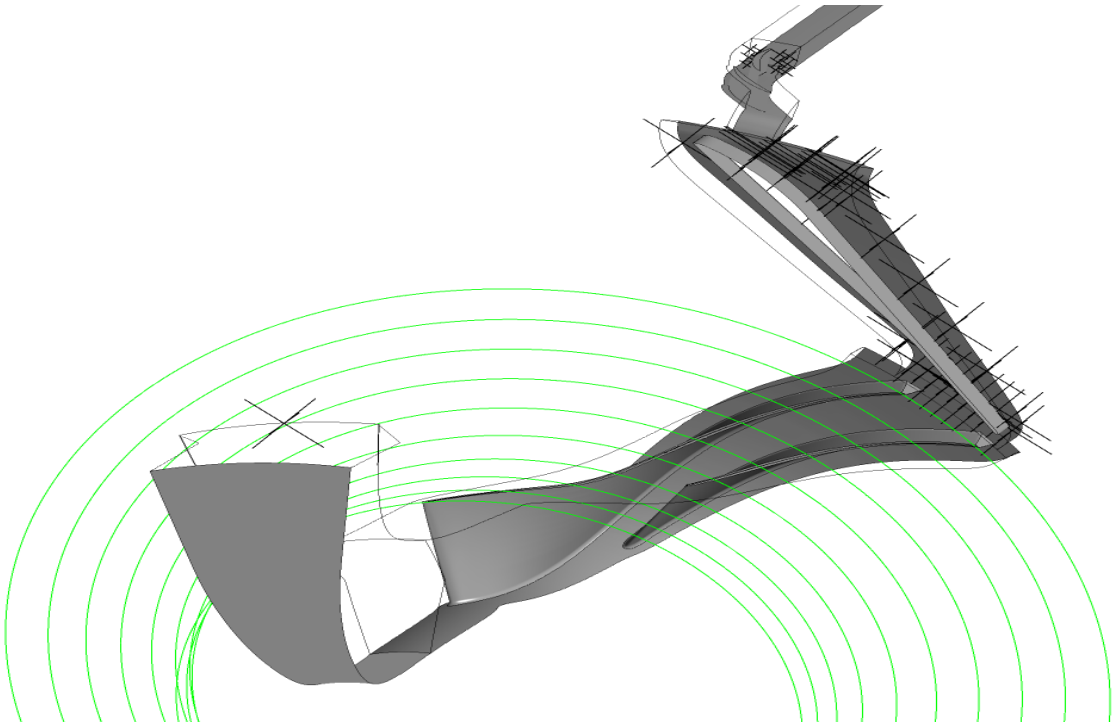

Figure 2.12 Locations of experimental measurement locations

In the impeller, circles of the correct radius and at the correct axial location were used for the static pressure taps. Pressure results only exist on each circle when it passes through the

simulated domain. Therefore, the pressure was averaged across each circle to obtain the static pressure at that location.

The diffuser and deswirl locations were added as points that corresponded to the static pressure tap or total pressure or total temperature element. The diffuser leading edge static pressure taps are located around the circumference experimentally but are all located in one passage numerically. The other static pressure taps – throat, flow path, covered exit, and trailing edge – are all located in one passage as they are experimentally. However, three passages are instrumented in this way experimentally, so they were averaged for comparison to the numerical results. The total pressure rakes at the diffuser exit and the total pressure and total temperature rakes at the deswirl exit are located circumferentially as well but have been simulated in one passage. The pitch locations with respect to the diffuser blade or the deswirl blade have been duplicated though.

2.2.4 Grid Convergence Study

After completion of the numerical domain, a grid convergence study was carried out to quantify the numerical uncertainty of the grid while evaluating that uncertainty against the computational expense required. The method used for the study was the Grid Convergence Method that is based on a Richardson extrapolation and is detailed in Celik et al. (2008). This method is designed to calculate the numerical uncertainty of the three grids being used against a grid with an infinite number of nodes whose performance parameters are calculated using a Richardson extrapolation. The number of nodes in each grid being used is summarized in Table 2.4.

Table 2.4 Nodes used in each domain and each grid for the grid independence study

	Grid 1	Grid 2	Grid 3
Inlet/Impeller	19,921,165	8,703,496	3,733,177
Diffuser	13,929,000	6,165,250	2,661,606
Deswirl/Outlet	6,320,340	2,789,836	1,240,371
Total	**40,170,505**	**17,658,582**	**7,635,154**
Normalized Grid Spacing	**1**	**2.275**	**5.261**

The process was completed for both the efficiency and the total pressure ratio for a given set of parameters. The factor in the equation to convert centerline average roughness to equivalent sand grain roughness is six for this study, the operating point for this study is near the peak

efficiency point, and the larger tip clearance is incorporated for the purposes of this study. The efficiency and the total pressure ratio are plotted for each of the three grids, as well as the Richardson extrapolation value, in Figure 2.13 and Figure 2.14, respectively.

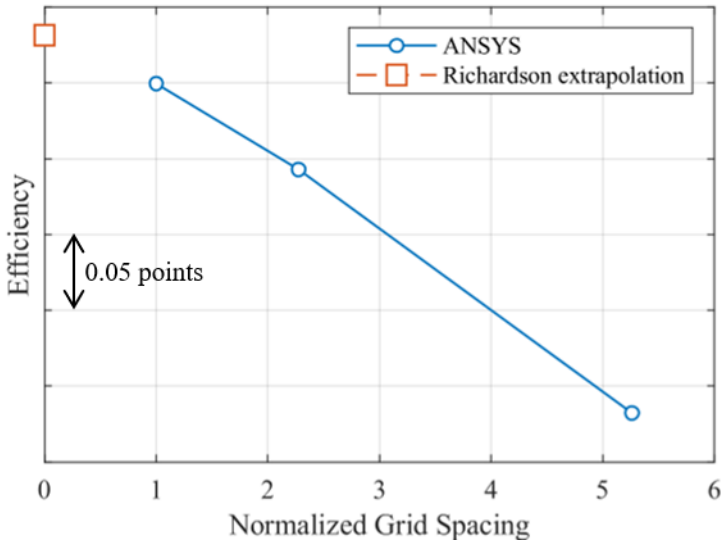

Figure 2.13 Efficiency for grid convergence study

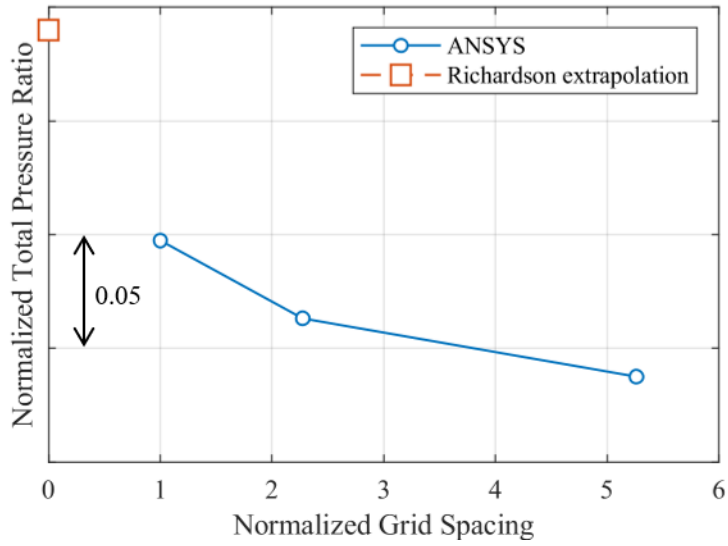

Figure 2.14 Total pressure ratio for grid convergence study

The errors of the three grids were calculated with respect to each other and the extrapolated point for both the efficiency and total pressure ratio, and the time it took each simulation to run on

the same number of nodes on one of the Purdue University research computing clusters was recorded. The approximate relative error, e_a^{21}, is the error of the performance parameter between grids 1 and 2. The extrapolated relative error, e_{ext}^{21}, is the error calculated between grid 1 and the extrapolated value. And the grid convergence index, GCI^{21}, is the numerical uncertainty in the fine grid solution, calculated using the approximate relative error between the medium and fine grids (grids 1 and 2), the ratio of representative cell size between grids, and a factor of safety. The factor of safety used is 1.25 because three grids were used for the procedure. More details about the calculation of errors can be found in Celik et al. (2008).

Table 2.5 lists the errors calculated for this study. The apparent order of the Richardson extrapolation for the efficiency calculations is 3.7279 and for the total pressure calculations, 1.1511. And finally, Table 2.6 lists the solver time per iteration needed for each grid. The time being used for this calculation does not include the time that the computer takes to discretize and set up the simulation, only the time spent iterating to a solution. There is a benefit of increasing the resolution from grid 3 to grid 2 without much of an increase in computational cost. However, despite the larger numerical uncertainty in the total pressure ratio, the increase in computation time from grid 2 to grid 1 outweighs the benefit of increased resolution in the solution, thus grid 2 was chosen for the computational study.

Table 2.5 Fine grid numerical error calculations

	Efficiency	**Total Pressure Ratio**
$\boldsymbol{e_a^{21}}$	0.0717%	0.4973%
$\boldsymbol{e_{ext}^{21}}$	0.0403%	1.3235%
$\boldsymbol{GCI^{21}}$	0.0504%	1.6765%

Table 2.6 Computational time

Grid	**Solver time per iteration (sec)**
Grid 1	25.137
Grid 2	11.653
Grid 3	8.517

3. COMPARISON AND VALIDATION OF THE NUMERICAL MODEL

Once the grid convergence study was complete, validation of the numerical model took place using the experimental data and the numerical results for the larger tip clearance case. Results on a stage and component level are compared to assess the validity and accuracy of the model. The numerical results presented are calculated with the same measurement locations and methods as the experimental results. For example, the total pressure ratio is calculated by first area averaging each element on a total pressure rake to obtain a rake average and then area averaging each rake average to calculate a total pressure at the deswirl exit. The same process was followed numerically by locating each instrumentation location and exporting the variable to follow the experimental procedure. Because the simulation only includes one passage for each domain, there is no circumferential variation like there is in the experiment.

3.1 Stage Performance

The stage performance consists of the total pressure ratio, total temperature rise ratio, and stage efficiency. There are some minor differences between the numerical model and the experimental data but overall, the numerical model captures the stage performance well.

The total pressure ratio for both the experimental and computational results is shown in Figure 3.1. The abscissa is the mass flow rate normalized by the mass flow rate at the peak efficiency point. The total pressure ratio is overpredicted by the numerical model for the entire speedline but matches the general shape of the speedline. The main differences between the experimental and numerical results is in knee of the speedline and the choked mass flow rate. The numerical simulation does not quite capture the quick bend in the knee of the speedline and predicts a more gradual transition from the choked mass flow to the peak efficiency point. The choked mass flow rate is overpredicted by the numerical results by about 1.8%. At the peak efficiency point from the experimental data, the percent difference in the total pressure ratio between the experimental data and the computational results is 2.8%. The uncertainty in the experimental total pressure ratio is within the size of the symbol and the uncertainty in the choked mass flow rate is about as wide as the symbol. For the computational results, the numerical uncertainty in total pressure ratio was quantified during the grid convergence study in Section 2.2.4.

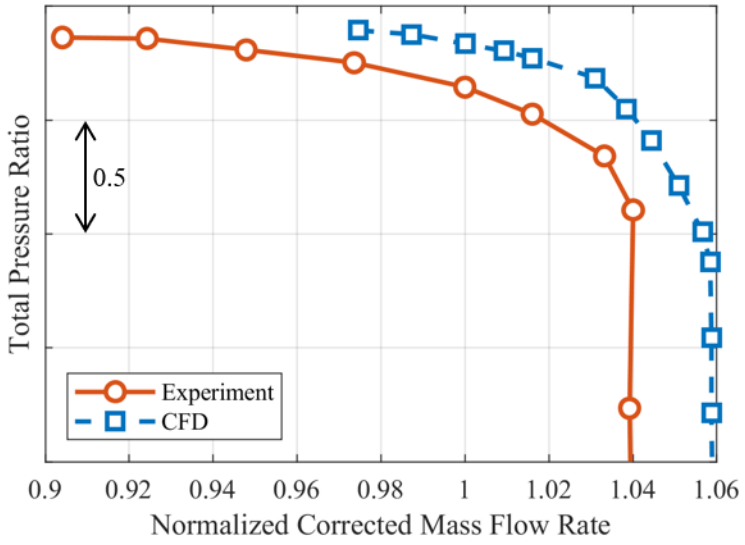

Figure 3.1 Total pressure ratio comparison at design speed for the larger tip clearance

The differences in the total pressure at the deswirl exit plane at the peak efficiency point between the numerical model and the experiment are depicted in Figure 3.2. The contours are shown with the suction surface of the deswirl blade on the right and the pressure surface on the left. This orientation means that the contours are oriented such that the observer would be upstream of the plane and looking in the same direction that the flow is traveling. Because Figure 3.1 shows that the total pressure is different between the numerical simulation and the experiment, the contours in Figure 3.2 are each normalized by their respective maximum so that they can be plotted on the same scale and differences in the total pressure profile can be shown. Despite the absolute values of total pressure being too different to plot on the same color scale, the variations in total pressure at the deswirl exit plane for both the experiment and the numerical simulation are about 1.5 psi, respectively.

From Figure 3.2, the contours of total pressure at the deswirl exit plane are significantly different. The experiment predicts a lower total pressure region near shroud and closer to the suction surface while the numerical simulation predicts that the lower total pressure region is closer to the hub and extends more across the pitch. The experiment also shows a low-pressure region at about 60% pitch from the hub up to about 60% span. This area of low pressure is not captured by the numerical simulation but rather a pitchwise band of low pressure at 20% span is predicted. The

high-pressure regions are also not accurately simulated as the experiment shows a high-pressure region forming near the hub at 20% pitch and a high-pressure region near 80% pitch at all spans that likely continues to increase in pressure moving towards the pressure surface. At 40% pitch and 80% span, a smaller region of higher pressure exists in the experimental data, and this is overpredicted by the numerical model, which shows a larger region of higher pressure than the experiment. These differences are likely emanating from the use of mixing planes throughout the model for reference frame changes and pitch changes between the domains.

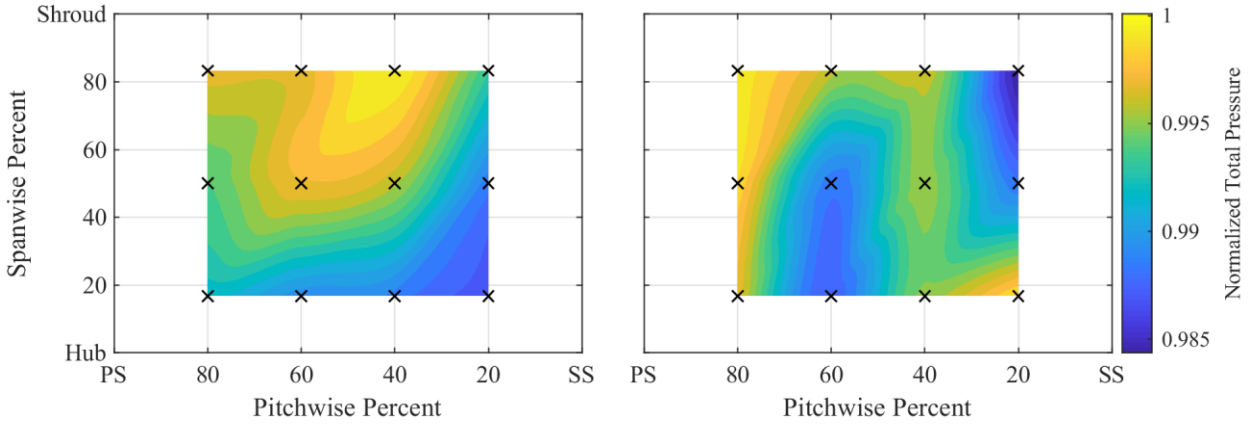

Figure 3.2 Total pressure contours at the deswirl exit for the numerical simulation (left) and the experiment (right)

The comparison of total temperature rise ratio matches better than the total pressure ratio, but there is still a slight overprediction. Figure 3.3 shows the total temperature rise ratio for the experimental data and the numerical simulation. When the compressor is operating in the choked condition, there is no change to the work input, and consequently, there is no change to the total temperature rise ratio. Examining the cluster of data points that were acquired while in the choked condition shows that the main difference between the numerical simulation and the experimental data is a shift towards increased mass flow rate for the computational results. As mentioned above, the numerical simulation overpredicts the choked mass flow rate but the total temperature rise ratio is predicted well. There is about a 0.2% difference in total temperature rise ratio between the experiment and the CFD results at the peak efficiency point from the experimental data. However, when comparing the speedlines and accounting for the difference in choked flow rate, the numerical results are underpredicted. The points closer to choke show better agreement indicating

that as the mass flow rate is decreased, the prediction of total temperature rise ratio by the numerical simulation occurs at a slightly different slope than the numerical data.

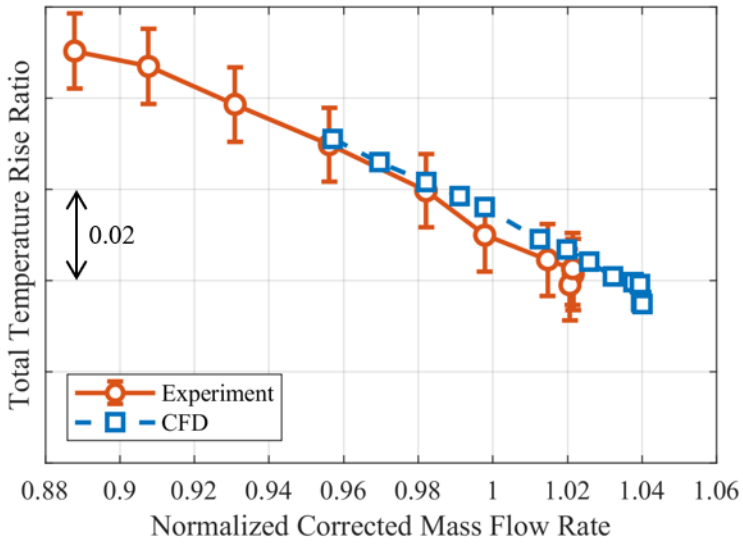

Figure 3.3 Total temperature rise ratio comparison at the design speed for the larger tip clearance

The total temperature contours as measured from the experiment and the numerical simulation at the deswirl exit plane are shown in Figure 3.4. The contours shown here are in the same orientation as those for the total pressure, but the scale is slightly different. Because the differences in the exit total temperature normalized by the inlet total temperature are much smaller between the experiment and the numerical simulation, they can be presented on the same scale to show both the differences in absolute measurements but also the differences in the profiles at that plane. It also should be noted that in either case, the differences in total temperature measured at the rake locations vary about 5 degrees Rankine (about 0.5% of deswirl exit total temperature) for both the experimental data and the numerical results, respectively.

While the total temperature rise ratio is predicted very well, the contour at the exit plane is different between the experiment and the numerical simulation. A high-temperature region exists in the pressure surface shroud corner for the experiment that is correctly predicted by the simulation, however, the simulation predicts that the extent of the high temperature region is much larger than it is. Because of the overprediction of the area of high-temperature, this leads to an underprediction of the low-temperature area. The numerical simulation shows that the area of

lowest temperature exists in the suction surface hub corner whereas the lowest total temperature for the experiment occurs close to the suction surface shroud corner. The experimental total temperature contour shows a nearly vertical pitchwise gradient in total temperature near the middle of the passage while the numerical results show a diagonal gradient from the pressure surface hub corner to the suction surface shroud corner. Overall, the total temperature is predicted well as the variations in total temperature across the deswirl exit plane are small and the total temperature rise ratio prediction matches well with the experiment.

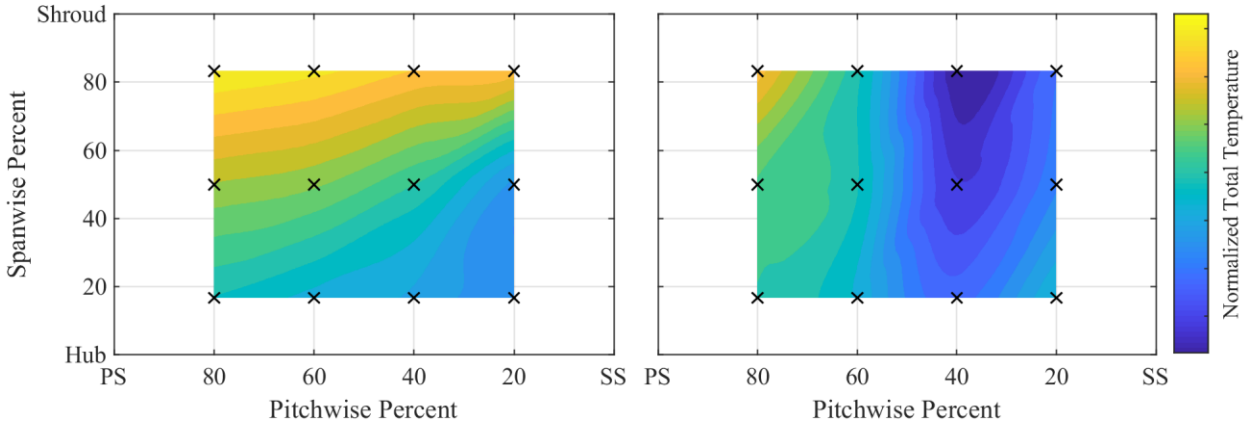

Figure 3.4 Total temperature contours at the deswirl exit for the numerical simulation (left) and the experiment (right)

The numerical prediction of efficiency is similar to that of the total pressure ratio. Shown in Figure 3.5, the numerical results are overpredicting the efficiency but matching the shape of the speedline well. The overprediction in efficiency is caused by an accurate prediction work input but an underprediction in loss. By accounting for the difference in choked mass flow rate, an underprediction in work input was found and this could also be contributing to the overprediction in efficiency. Again, the simulation cannot achieve the same shape around the knee but does well in the upper part of the speedline. Intermediate points were simulated to better facilitate the changing of boundary conditions when mapping the speedline, but the experimental peak efficiency point is also considered the numerical best efficiency point in the analysis. The percent difference between the experimental data and the numerical simulation at this best efficiency point is about 1.8%.

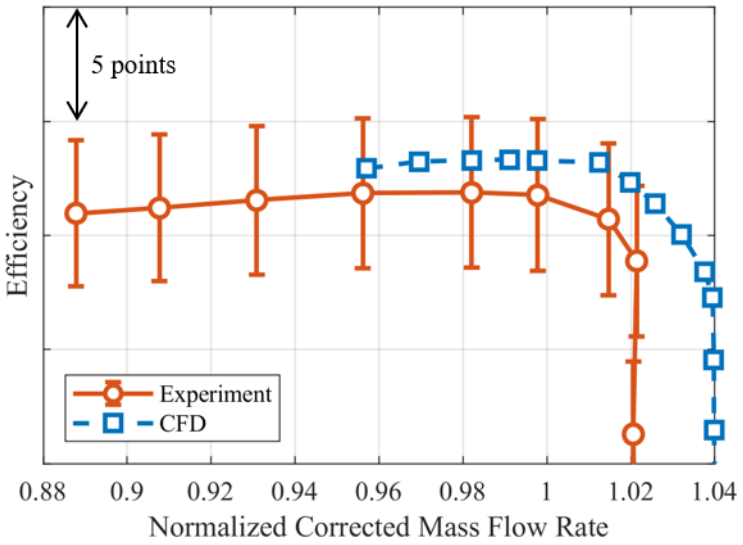

Figure 3.5 Efficiency comparison at design speed for the larger tip clearance

The efficiency calculated from the CFD results is within the uncertainty range of the experimental efficiency. However, due to the range of uncertainty, it is difficult to draw a conclusion regarding the absolute values of numerical and experimental efficiency. Despite the uncertainty in experimental efficiency, the data points are repeatable between different tests. A health check data point is taken during each test at the design speed and near the peak efficiency point. From the six health check points that were taken during this testing campaign, the standard deviation in efficiency was 0.06 points and the range was 0.14 points.

3.2 Impeller Performance

The impeller is one of the main components for the simulation to correctly predict for the stage performance to be accurate. The impeller performance is quantified through the impeller total pressure ratio, the impeller efficiency, and the static pressure rise through the impeller.

The impeller total pressure ratio for the experiment and the numerical simulation is depicted in Figure 3.6. The impeller total pressure ratio from the numerical solution was calculated using the same method as the experimental data, and is the iterative method outlined in Section 2.1.4. The numerical simulation slightly underpredicts the impeller total pressure ratio with -0.8% difference at the peak efficiency point. The numerical speedline is also shifted to the right due to

the increased choked flow being overpredicted. Accounting for this shift in choked flow would result in a larger underprediction at all points simulated.

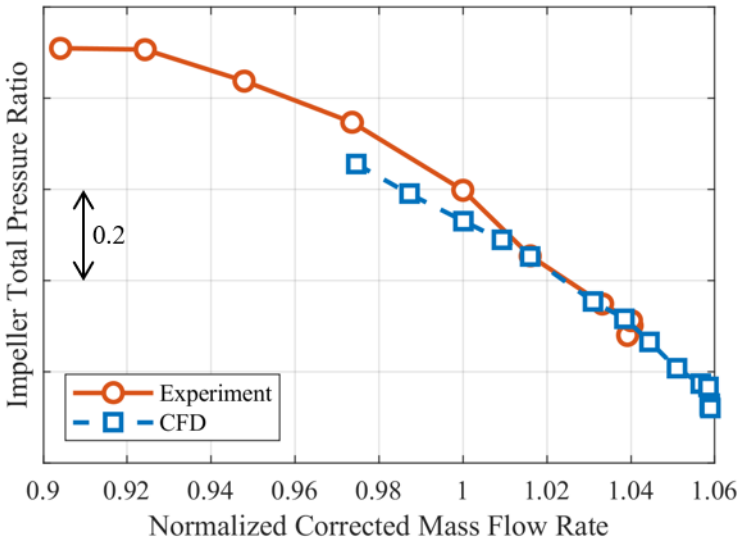

Figure 3.6 Impeller total pressure ratio comparison at the larger tip clearance

Because of the use of an iterative procedure to calculate the total pressure at the impeller exit (and subsequently, the impeller total pressure ratio), the numerical results are used to provide an area average and a mass flow average of the impeller exit total pressure for comparison. There is a -0.8% difference between the experimental data and the numerical results for the impeller total pressure ratio when using the iterative scheme for both calculations. Using only the results from the numerical simulation, there is about 0.01% difference between the impeller total pressure ratio calculated with the iterative procedure and that calculated using the area average of the total pressure at the impeller exit plane. However, when using a mass flow average at the impeller exit plane and comparing to the iterative procedure, the percent difference increases to about 0.35%. The iterative procedure is providing similar results to the area-averaged impeller total pressure ratio. Though the iterative method differs more when compared to the mass flow averaged results, this difference is relatively small.

The impeller efficiency is also predicted well by the numerical model. The impeller efficiency speedlines are shown in Figure 3.7 and both are calculated with the experimental method. A similar trend exists for the impeller efficiency as for the impeller total pressure ratio. The

numerical simulation is slightly underpredicting the impeller efficiency and overpredicting the choked mass flow rate. The experimental data also shows a strong peak and then a decrease of about 1 point to the last steady point before the compressor becomes unstable. The numerical simulation can predict the increase in impeller efficiency from choke to near the stage peak efficiency point but the values for the numerical simulation decrease at a much lower rate than those from the experiment. Additionally, the percent difference between the experimental data and the numerical simulation at the peak stage efficiency point is -0.6%.

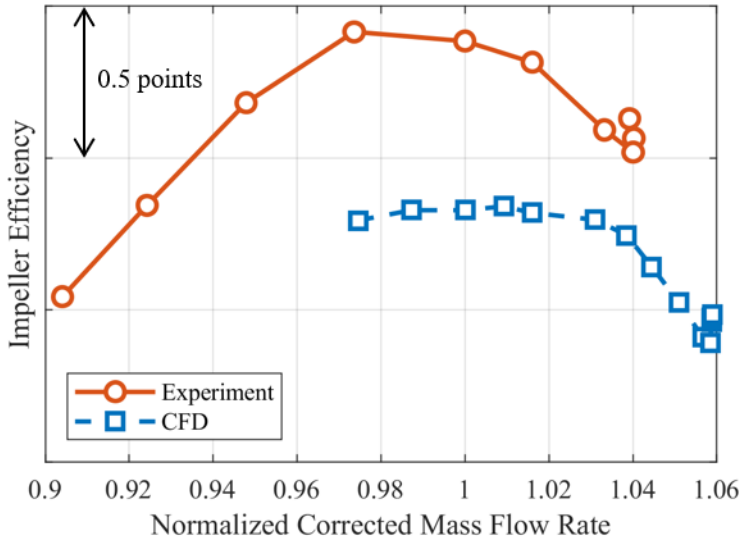

Figure 3.7 Impeller efficiency comparison at the larger tip clearance

The amount of blockage assumed in the iterative calculation for impeller exit total pressure will affect the results for the impeller total pressure ratio and impeller efficiency. As the same blockage is used for both the experimental data and the CFD results, the comparison between the two will not change with blockage, rather the overall value of the impeller total pressure ratio or impeller efficiency will be affected. A blockage of 10% is used for the speedlines in Figure 3.6 and Figure 3.7 but cases with blockages of 7% and 13% were also computed with the CFD results to assess its impact on the final results. Changing the blockage results in a near constant vertical shift of the speedline for both impeller parameters and both clearances. The variation in impeller total pressure ratio is about 0.045 points between 7% and 13% blockage while the variation in

impeller efficiency is about 0.33 points for the same blockage range. These variations are both at or less than 0.5% of the total value of each parameter.

Finally, the static pressure rise through the impeller is compared between the numerical simulation and the experimental data. The static pressure is plotted with each point being a different static pressure tap in the impeller and those locations replicated in the numerical post-processing. The static pressure is also normalized by the total pressure measured at the inlet rakes to make the data between that taken from the experiment and the numerical simulation results comparable.

Figure 3.8 illustrates the static pressure rise through the impeller for the peak efficiency point for both the experimental data and the numerical results. The static pressure rise is predicted by the numerical simulation very well through the impeller. In the inducer, the measurements are close to identical, but there is some deviation around the knee. As the static pressure rise starts to increase more rapidly in the knee, the numerical solution struggles and underpredicts the static pressure at those points. But, near the exducer of the impeller, the static pressure at those points becomes closer to the experimental data. Overall, the numerical simulation closely matches the experimentally measured static pressure rise through the impeller.

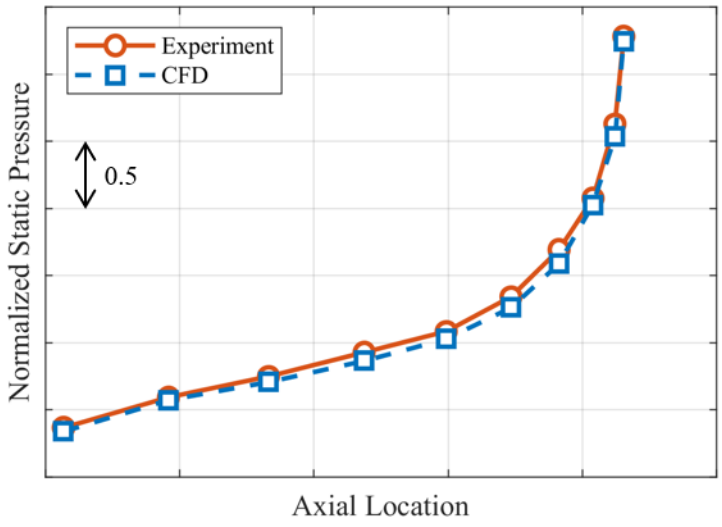

Figure 3.8 Impeller static pressure rise comparison for the larger tip clearance

3.3 Diffuser Performance

The numerical results in the diffuser do not match the experimental data as well as the match that was presented for the impeller. The diffuser performance is typically characterized by the static pressure rise coefficient, the total pressure loss coefficient, and the diffuser effectiveness. Additionally, the static pressure through the diffuser will be analyzed as well as the total pressure results from the diffuser exit total pressure rakes.

First, the diffuser static pressure rise coefficient, for both the experimental data and the numerical results, is shown in Figure 3.9. The numerical model is overpredicting the static pressure rise coefficient by 11.1% at the peak efficiency point compared to the experimental data. From equation (2.16), the static pressure rise is normalized by the dynamic pressure at the impeller exit, however, both the impeller total pressure and impeller static pressure rise are predicted well so a majority of the difference is attributed to the static pressure rise in the diffuser. A steady simulation is being used for the numerical results which means that a mixing plane is placed between the impeller exit and the diffuser inlet due to the reference frame change. Because the mixing plane circumferentially averages the fluxes, certain flow features that significantly affect the diffuser flow field are averaged out, such as the jet and the wake from the impeller outflow. While necessary for the steady simulation, the mixing plane prevents these flow features from being modeled, and thus, the simulation overpredicts the amount of static pressure gained through the diffuser. The speedlines for the static pressure rise coefficient will also be affected by the choice of blockage factor in the impeller exit iterative calculation. Using the same ranges as before, the variation in the static pressure rise coefficient is about 0.007 points, or slightly above 1% of the value of C_p, for the 6-point change in blockage.

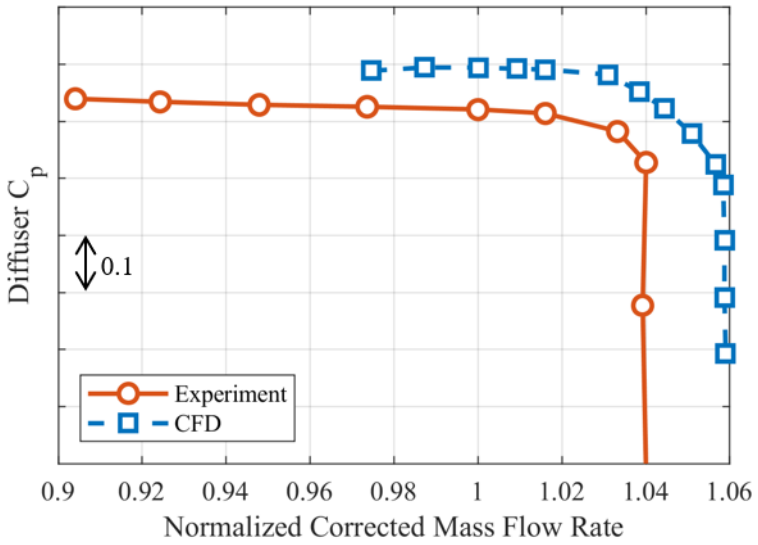

Figure 3.9 Diffuser static pressure rise coefficient comparison for the larger tip clearance

Because of the differences in the static pressure rise coefficient, the pressure distribution is analyzed at various points throughout the diffuser. There are three instrumented diffuser passages around the annulus and each of the measurements is averaged to provide a representative value at that location. Figure 3.10 depicts the static pressure at each instrumentation location at the peak efficiency point normalized by the inlet total pressure for both the experiment and the numerical simulation. The uncertainty of each experimental static pressure measurement is within the size of the symbol. Station 2 is the impeller trailing edge and the pressures match well. However, crossing the mixing plane between the impeller trailing edge and the diffuser leading edge (station 3), there is more of an increase in static pressure for the numerical simulation. This trend continues through the throat of the diffuser and the first half of the diffuser flow path static pressures. Near the trailing edge, the difference between the experiment and the numerical simulation is approximately constant. The numerical simulation struggles to accurately capture the flow physics at the leading edge, throat, and downstream of the throat in the diffuser. This is critical because most of the static pressure rise and flow features important to determining the performance occur in the diffuser.

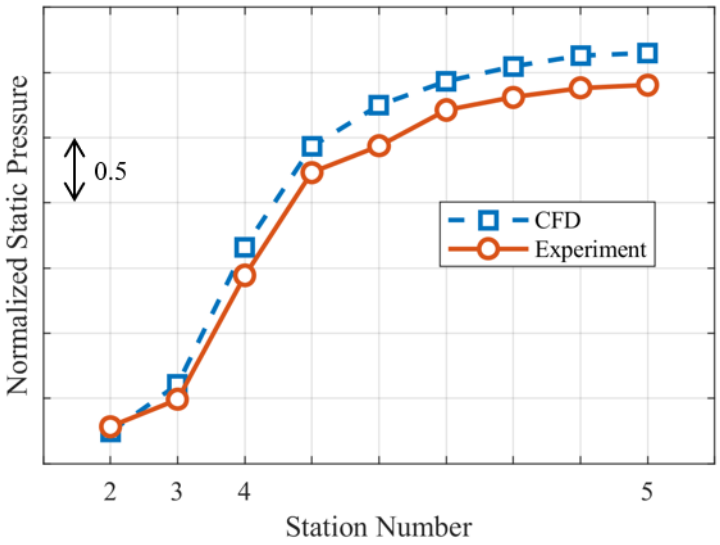

Figure 3.10 Static pressure through the diffuser at the larger tip clearance best efficiency point

Figure 3.11 shows the static pressure distributions at the diffuser leading edge and the diffuser throat for both the experiment and the numerical simulation on the same scale and normalized by the inlet total pressure. Again, the experimental uncertainty is within the size of the symbol. The trend at the diffuser leading edge is reasonably well predicted, but there are some distinct features that the numerical simulation fails to capture. In the middle of the pitch, the pressures are of similar magnitude with the minimum occurring slightly off from the experiment, but near the suction surface (SS) and pressure surface (PS), there is a significant deviation of the numerical model from the experiment. On the pressure surface, the increase in static pressure is overpredicted by the numerical model with almost twice the increase from 80% to 90% pitch. On the suction surface, the experimental data shows a low-pressure region forming near the leading edge of the blade, but the numerical model fails to accurately predict this as the pressure continues to increase at 10% pitch instead of decreasing. The incidence of the flow on to the diffuser vane is causing the decrease in pressure from 20% to 10% pitch in the experimental data. Because the pressure continues to increase in that same pitch range for the numerical results, the incidence is not being predicted correctly and the flow features are different from the experiment. In the diffuser throat, the static pressure is overpredicted at all points by the numerical model, but the trend is consistent. The flow in the passage between 25% and 75% pitch has experienced a large increase in static pressure, and the numerical simulation is able to capture this but with an overprediction.

At the diffuser leading edge, the numerical simulation underpredicts the static pressure between 50% and 75% pitch and overpredicts it between 25% and 50% pitch. However, at the diffuser throat, the static pressure is overpredicted at all three points. The mixing plane between the impeller trailing edge and the diffuser leading edge and the single passage simplification is causing an adverse effect in the ability of the numerical model to accurately predict the flow distributions. In addition to the mixing plane not being realistic of the actual flow features, the close proximity of it to the diffuser leading edge and throat, where significant changes in the flow field occur, is also negatively affecting the numerical model performance.

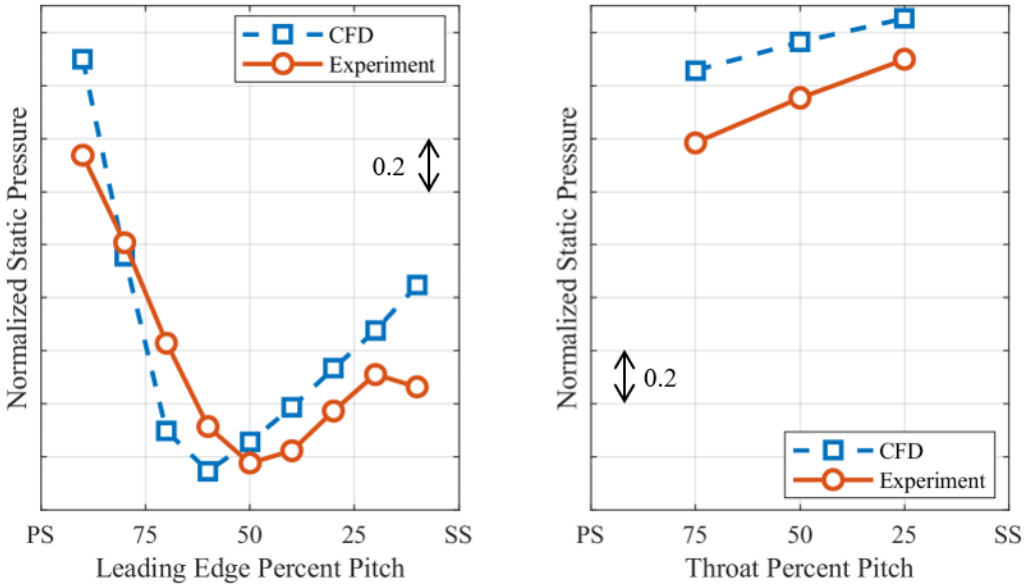

Figure 3.11 Diffuser leading edge (left) and throat (right) static pressure distributions

The differences in prediction of static pressure across the passage continue to propagate through the passage, as shown in Figure 3.12 with the covered exit and trailing edge static pressure distributions that are shown on the same scale and with experimental uncertainties within the size of the symbol. At the diffuser covered exit, the numerical model overpredicts the value of pressure, like the pressure distribution in the diffuser throat. The numerical results also indicate an upward trend in pressure from 75% to 25% pitch whereas the experimental data show an almost constant pitchwise pressure. At the trailing edge, the experimental static pressure distribution is similar to that at the covered exit as there is not much change with pitchwise position. The numerical model

fails to predict this as the increase in static pressure across the pitch is larger than that at the covered exit. A significant part of the differences in these pressure distributions originate near the leading edge and throat of the diffuser in the model and grow slightly from the throat to the trailing edge. The trend in static pressure across the passage is consistent up to the trailing edge where 25% and 50% pitch static pressures increase drastically in the numerical results causing a significant difference across the passage whereas the experimental data show an almost constant distribution between 25% and 75% pitch. Overall, the static pressure through the diffuser is overpredicted while the impeller trailing edge static and total pressures are predicted very well, leading to the discrepancy in the static pressure rise coefficient in the diffuser between the experimental data and the numerical simulation.

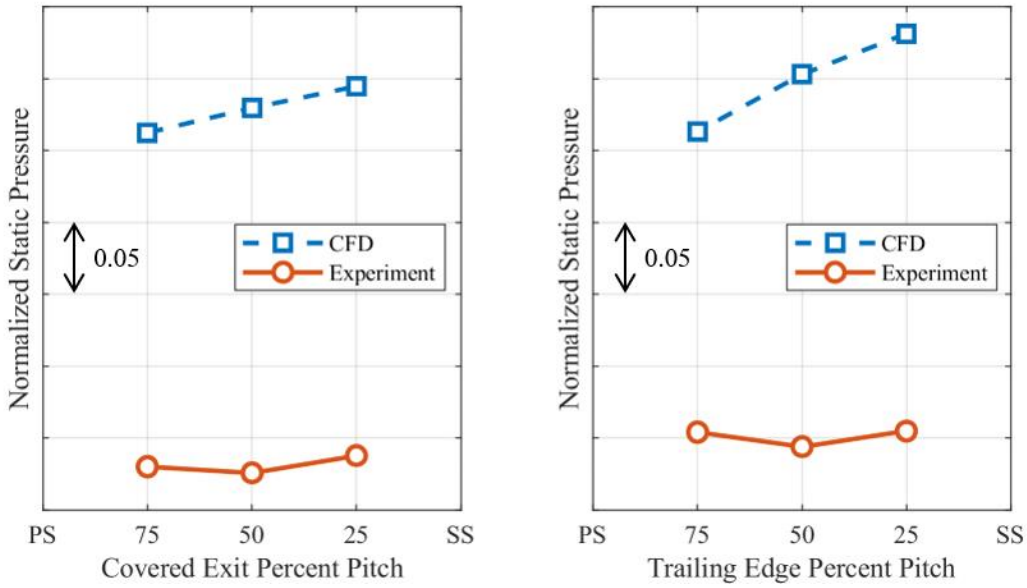

Figure 3.12 Diffuser covered exit (left) and trailing edge (right) static pressure distributions

Like the static pressure rise coefficient, the total pressure loss coefficient is also overpredicted by the numerical model. The comparison between the experiment and the simulation is shown in Figure 3.13 and while the shape of the two speedlines is similar, the total pressure loss coefficient is overpredicted by 5.9% at the peak efficiency point. The total pressure loss coefficient is also divided by the dynamic pressure at the impeller exit and both the static and total pressures at the impeller exit are reasonably well predicted. The main source of disagreement between the

experimental data and the numerical results is the loss of total pressure through the diffuser. The mixing plane between the impeller and diffuser is causing unrealistic flow patterns and too much total pressure loss compared to the experiment. The total pressure loss is also more significantly impacted by the blockage factor from the impeller exit total pressure calculation, although still a nearly linear vertical shift in the speed line. The 6-point change in blockage resulted in about a 0.007-point change in the total pressure loss coefficient, over 2% of the total loss near the minimum loss point.

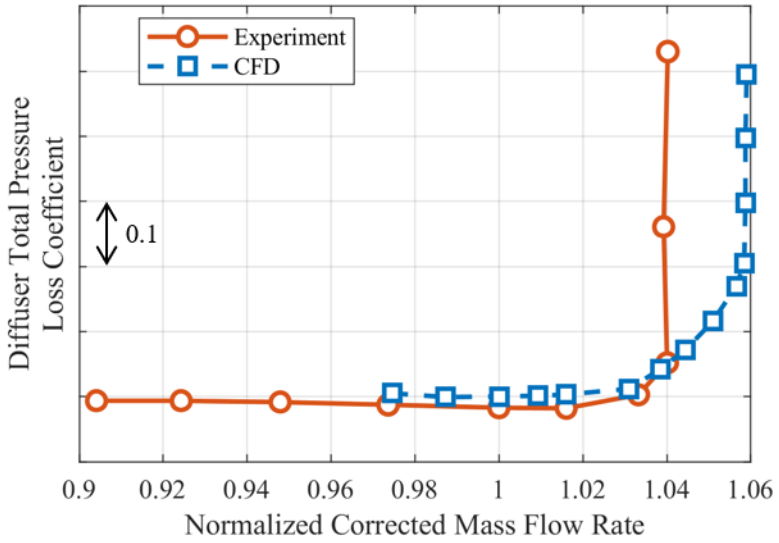

Figure 3.13 Diffuser total pressure loss coefficient comparison for the larger tip clearance

Total pressure contours at the diffuser exit depicted in Figure 3.14 provide valuable insight into the flow leaving the diffuser. With the three total pressure rakes (each with three elements), the contours were generated the same way for both the experiment and the numerical simulation and are shown on the same scale with the same number of color levels. The total pressure is also normalized by the inlet total pressure for comparable results between the experiment and the numerical simulation. The orientation is the same as the total pressure and total temperature contours at the deswirl exit such that the suction surface of the diffuser blade is on the right and the pressure surface is on the left. An observer would be upstream, near the diffuser throat, looking in the same direction as the flow.

The contour on the left shows the numerical simulation results while the right contour shows the experimental data, and there are distinct differences between them. The minimum total pressure for the experiment is much lower than that from the numerical simulation. This corresponds to previous trends of pressure distributions in the diffuser where the impeller total pressure was more closely matched but slightly underpredicted, and in this case, the total pressure at the diffuser exit is overpredicted. Also noticeable from the contours is the difference in concentration of high and low pressure. In the experiment, the high-pressure region is near the center of the span but shifted towards the suction surface with the total pressure decreasing towards the pressure surface at all spans. In the numerical simulation, however, the high-pressure region is concentrated more towards the shroud but still shifted towards the suction surface. The high-pressure region also extends further towards the pressure surface above 50% span in the numerical simulation than it does in the experiment.

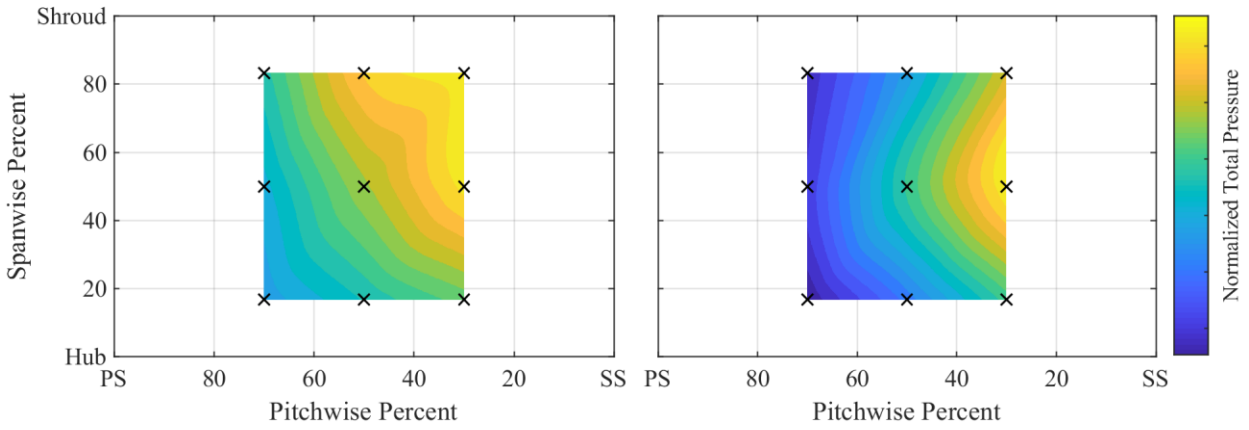

Figure 3.14 Diffuser exit total pressure contour for the numerical simulation (left) and the experiment (right)

The diffuser effectiveness, a measure of how well the diffuser is converting total pressure into static pressure, is shown in Figure 3.15. Diffuser effectiveness is a function of both the static pressure rise coefficient and the total pressure loss coefficient and while both are overpredicted significantly, the diffuser effectiveness is only overpredicted by 1.6% compared to the experiment. The simulation is able to more closely match the diffuser effectiveness and the ability of the diffuser to diffuse the flow for a given total pressure, but the values of static pressure rise and total pressure loss are not predicted correctly. The mixing plane between the impeller and diffuser is

likely causing the differences in static and total pressures. Considering only the diffuser downstream of the mixing plane, the overall performance trends are better simulated than the raw values of static pressure and the contours of total pressure.

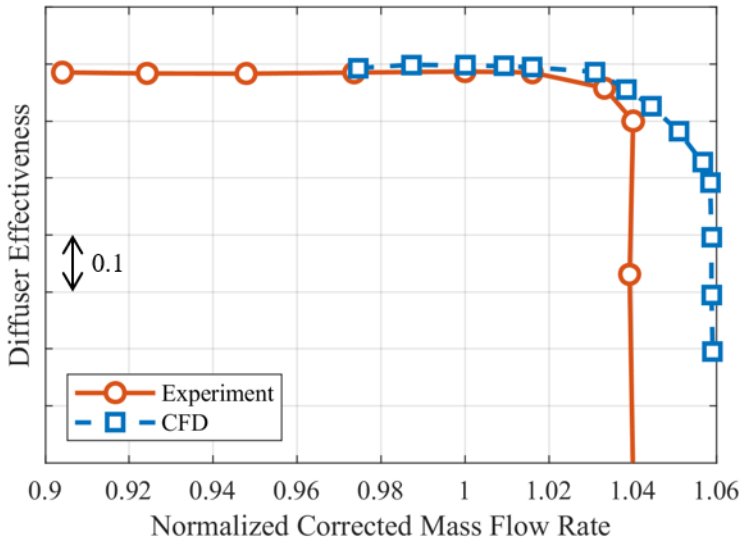

Figure 3.15 Diffuser effectiveness comparison for the larger tip clearance

3.4 Summary of Model Performance

Overall, the results of the numerical model match well with the experimental data. The numerical model can capture the qualitative nature of the stage and component performance but is unable to predict the quantitative nature of performance in some cases. The model is also not suitable for investigation of the detailed flow features in the diffuser and deswirl components. At a stage level, the model slightly overpredicts the total pressure ratio and efficiency but provides an accurate prediction of the total temperature rise ratio. The model also overpredicts the choked mass flow rate, so the total temperature rise ratio is underpredicted when accounting for the difference in choked mass flow rate. The performance prediction in the impeller is very similar to the experimental data. Not only are the impeller total pressure ratio and impeller efficiency matched well, but the static pressure rise through the impeller at the peak efficiency point is also closely matched. Similar to the total temperature rise ratio though, the difference in choked mass flow rate reveals that both impeller performance parameters are underpredicted by more than they appear. These results show that the numerical model is predicting impeller performance well and that the

flow features can be investigated. In the diffuser, however, the performance is overpredicted and the diffuser exit total pressure rakes illustrate that the flow features are not being captured accurately. This is also the case at the deswirl exit, where the total pressure and total temperature contours are different between the experiment and the numerical simulation. The steady numerical model can predict the performance of the stage, impeller, and diffuser, but should not be used for detailed flow investigations in the diffuser.

4. QUANTIFYING AND PREDICTING THE EFFECTS OF TIP CLEARANCE ON PERFORMANCE

After validation of the numerical model to the experimental data, using both functions in the ANSYS CFD-Post software and the physical locations of instrumentation with the experimental methodology, the ability of the model to predict tip clearance effects and sensitivities is evaluated and compared to the experimental data. First, various methods for analyzing the tip clearances effects and sensitivities are presented and examined to determine the best parameter to use when comparing data collected using multiple tip clearances. Using the recommended method, the experimental tip clearance effects and sensitivities at multiple speeds are presented at both a stage and component level. And lastly, the design speed experimental tip clearance effects are compared to those from the computational model at a stage and component level to assess the accuracy of the computational model on predicting the effects on performance due to the tip clearance.

4.1 Methods for Comparing Data with Different Clearances

To compare data acquired at two different exducer tip clearances, a point must be selected from the data for each axial tip clearance, essentially data on two different speedlines, for determination of tip clearance effects. Ideally, the points chosen will represent similar operating conditions so that a comparison and assessment can be made. Previously, authors have chosen a point, the design point or peak efficiency point (PE), with one tip clearance and then chosen the closest point with respect to inlet corrected mass flow rate for the second tip clearance. Then, by using each of these points, the sensitivity of each performance parameter can be compared. This method is used in Lou et al. (2018) for many published centrifugal compressors, where the authors assume a linear trend of the form in equation (1.5). Figure 4.1 shows the results when this method is applied to published centrifugal compressor data. The horizontal axis is the tip clearance ratio, computed by dividing the tip clearance by the blade height. The vertical axis is the change in efficiency from the efficiency extrapolated to zero tip clearance. Lou et al. (2018) show that assuming a linear trend with tip clearance is accurate by performing a regression analysis on each of the compressors used and reporting the coefficient of determination for each case. By using a

linear trend, the efficiency at zero tip clearance can be extrapolated and then the change in efficiency with increasing tip clearance can be calculated and plotted.

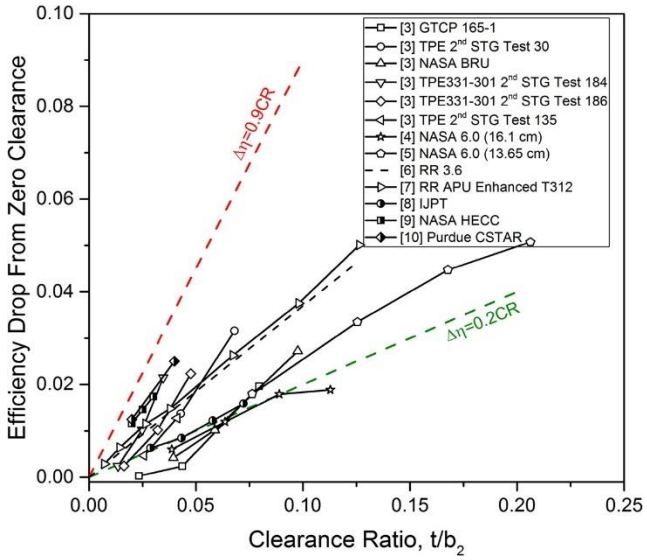

Figure 4.1 Efficiency trends from published centrifugal compressors (from Lou et al., 2018)

However, using data points with different tip clearances and the same inlet corrected mass flow rate may not accurately capture data points that represent similar operating conditions. Compressors operating at a higher mass flow rate and a lower total pressure ratio are operating in the choke condition, where the compressor is flowing as much air as physically possible. Choke can occur anywhere in the compressor, and it varies between designs. A compressor choking in the impeller will not experience any change in choke mass flow rate with varying tip clearance. But a compressor that chokes in the diffuser will have an increase in the choke mass flow rate as the tip clearance is decreased. Klassen (1977) discusses the data he presents and shows that the 90% speedline choke mass flow rate varies for different tip clearances, but the 100% speedline shows all tip clearance speedlines collapsing to one choke mass flow rate. Because different tip clearances can have the same choke mass flow rates, comparing data points with different tip clearances using the same inlet corrected mass flow rate was a straightforward method as there was only a vertical shift in the speedline. However, as illustrated in Figure 2.6 and Figure 2.7, the choke mass flow rate increases on the SSCC so attempting to compare data points with different clearances and similar inlet corrected mass flow rates may result in an unfair comparison due to the difference in operating condition.

To find a representative method for comparing data acquired using multiple tip clearances, three parameters were used to choose the data points, and the results were compared to those that matched inlet corrected mass flow rate. Parameters chosen were: exit corrected mass flow rate, a loading factor defined by $TPR/\dot{m}_{inlet\ corr.}$, and the work factor, ψ. Exit corrected mass flow rate is most representative of a constant throttle line and uses the exit total temperature and total pressure to correct the physical mass flow rate to corrected conditions. The next parameter, $TPR/\dot{m}_{inlet\ corr.}$, is calculated by dividing the total pressure ratio of the stage by the inlet corrected mass flow rate and defines a loading condition for the compressor. Points with similar values of $TPR/\dot{m}_{inlet\ corr.}$ and exit corrected mass flow rate will have similar incidence angles. And the last parameter is the work factor, defined in equation (2.9), which is the work done by the stage divided by the square of the wheel speed based on impeller exit diameter.

To pick the data points to compare, an anchor point was first chosen on the nominal tip clearance speedline, and then the closest point using one of the four parameters was chosen on the open tip clearance speedline. The peak efficiency point on the nominal tip clearance speedline was chosen as the anchor point. The closest point on the open tip clearance speedline with respect to the four parameters was chosen as the comparison point. To illustrate this, Figure 4.2 and Figure 4.3 show the efficiency and total pressure ratio maps for the design speed with the corresponding points marked. The peak efficiency point on the nominal tip clearance speedline is marked with an "x", and the closest points on the open tip clearance speedline are marked with different symbols regarding which parameter was used, a diamond for inlet corrected mass flow rate, an asterisk for exit corrected mass flow rate, a star for $TPR/\dot{m}_{inlet\ corr.}$, and a triangle for work factor, ψ.

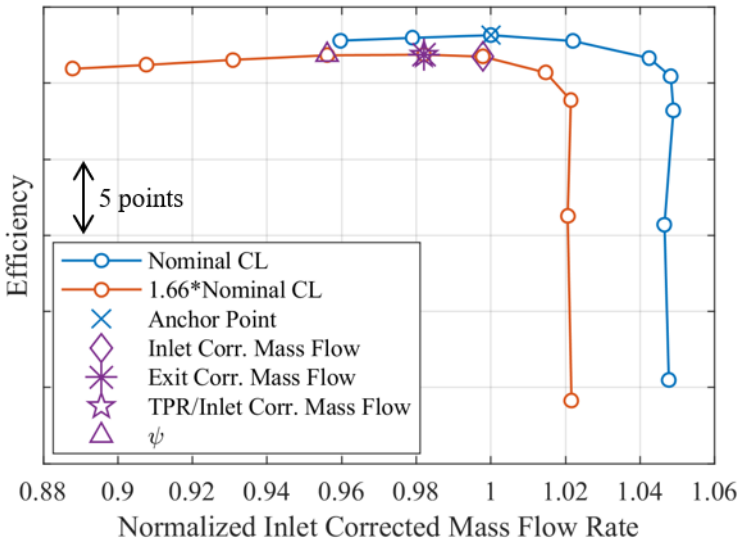

Figure 4.2 Efficiency compressor map with matching points marked

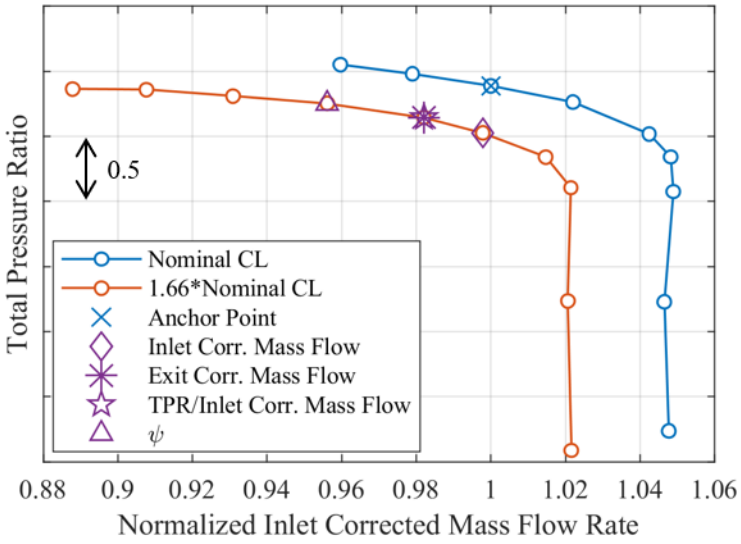

Figure 4.3 Total pressure ratio compressor map with matching points marked

The closest points on the larger tip clearance speedline with respect to exit corrected mass flow rate and $TPR/\dot{m}_{inlet\ corr.}$ are the same point so exit corrected mass flow rate will not be included in the analysis because the point using $TPR/\dot{m}_{inlet\ corr.}$ will yield the same results. Exit corrected mass flow rate requires additional information to calculate as the total temperature at the exit of the stage is needed whereas $TPR/\dot{m}_{inlet\ corr.}$ only requires total pressure ratio and mass

flow rate calculations. Therefore, while exit corrected mass flow rate can be calculated on the SSCC, it may not always be possible to calculate on other compressors so $TPR/\dot{m}_{inlet\ corr.}$ was chosen instead.

To compare the three parameters, the trends in stage efficiency were chosen to be used. The analysis of the efficiency trend with respect to the tip clearance will be discussed in Section 4.2.1 along with other stage performance parameters. The "efficiency percent decrease from zero clearance" is like that from Figure 4.1. A linear trend between tip clearance data points is still assumed and the efficiency at a zero tip clearance is extrapolated. However, this analysis will use the percent decrease from the extrapolated efficiency at zero clearance instead of the efficiency drop. The abscissa is the tip clearance ratio, the tip clearance divided by the blade height represented as a percentage, at the impeller exit. For the SSCC, the nominal axial tip clearance has a clearance ratio of 4.46% while the larger axial tip clearance ratio is 7.44%.

The efficiency sensitivity using the point selected with similar inlet corrected mass flow rates is shown in Figure 4.4. All speeds between 60% and 100% corrected speed (60%, 70%, 80%, 85%, 90%, 95%, and 100%) were intended to be used but there are not points with similar inlet corrected mass flow rates between 85% and 95% corrected speed. The closest points at those speeds were attempted to be used, but the difference in efficiency caused the trend to be unrealistically large due to very different operating conditions. Nonetheless, the sensitivity of efficiency increases from 60% to 70% corrected speed but is then approximately constant up to 100% corrected speed for the speeds shown.

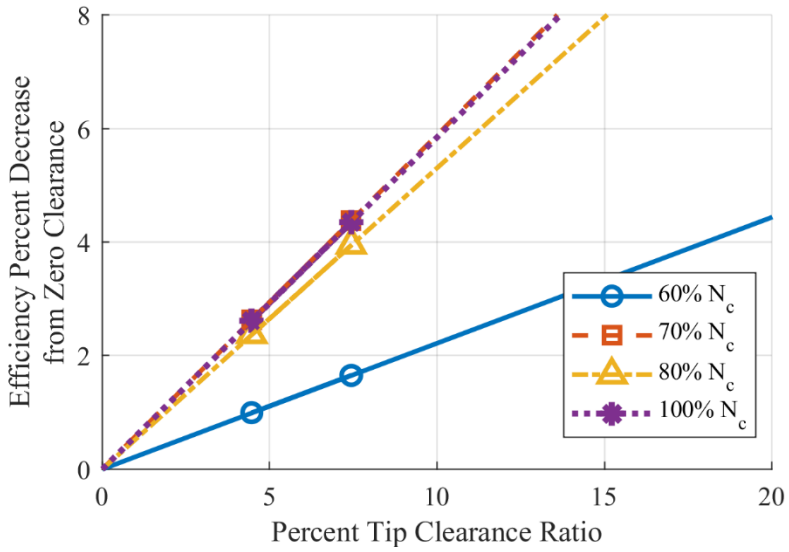

Figure 4.4 Efficiency sensitivity using inlet corrected mass flow rate

Figure 4.5 depicts the efficiency sensitivity but using $TPR/\dot{m}_{inlet\ corr.}$ as the method for obtaining the closest point on the open tip clearance speedline. This method shows all the speeds where data were collected from 60% to 100% corrected speed. The trend shows that the sensitivity increases from 60% to 80% corrected speed and then significantly increases at 85% corrected speed, where it is a maximum. Above 85% corrected speed though, the sensitivity decreases. This will be discussed in more detail in the next section, but a shock forms at the inducer of the impeller at about 85% corrected speed and becomes stronger as the speed increases. The formation of the shock wave causes the sensitivity of efficiency with respect to the tip clearance to increase but once the shock has formed, the sensitivity decreases meaning that the effect of the tip clearance on the efficiency is also decreasing.

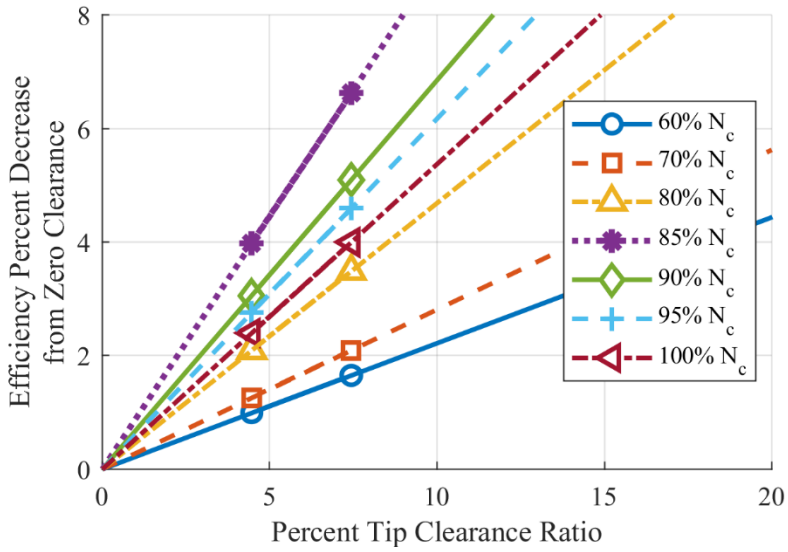

Figure 4.5 Efficiency sensitivity using TPR/inlet mass flow

Finally, the sensitivity of the efficiency using the work factor as a basis for choosing the open tip clearance data point is shown in Figure 4.6. The sensitivities start the same as in Figure 4.5 with it increasing from 60% to 80% corrected speed. A similar increase in the sensitivity occurs at 85% corrected speed but now there is a slight increase from 85% to 90% corrected speed. As before, the sensitivity decreases at 95% corrected speed but now increases to 100% corrected speed. This behavior is likely related to the shock formation in the inducer of the impeller, but the trends are not as clear as those from using $TPR/\dot{m}_{inlet\ corr.}$

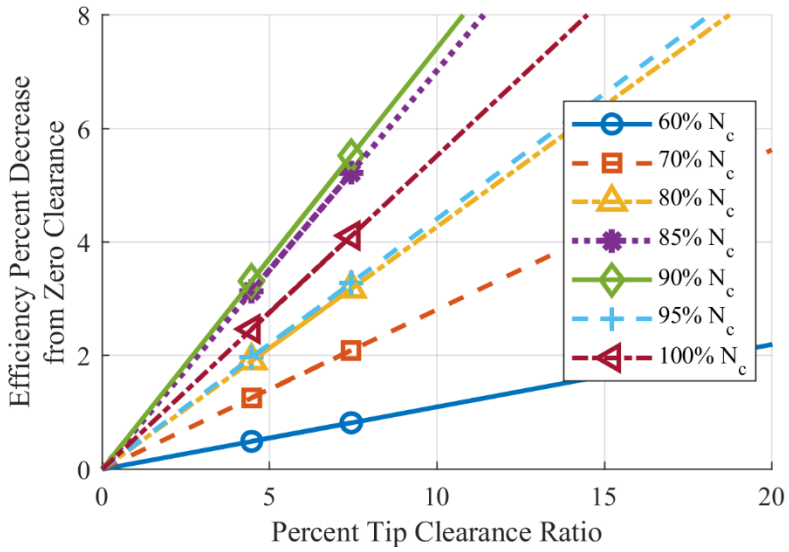

Figure 4.6 Efficiency sensitivity using work factor

Upon comparison of each of the three methods, the results from the method using inlet corrected mass flow rate do not accurately represent performance because the loading condition is not matched, and there are not points that are close enough using inlet corrected mass flow rate to provide an accurate analysis. However, using both $TPR/\dot{m}_{inlet\ corr.}$ and the work factor are viable options. The method using $TPR/\dot{m}_{inlet\ corr.}$ provides clearer trends as there is an obvious upward trend towards 85% corrected speed and then a decreasing trend to 100% corrected speed once the shock in the inducer has formed. For a better comparison between the two methods, Figure 4.7 shows the efficiency of the anchor point at the nominal clearance for each speed and the efficiency of the corresponding point at the larger tip clearance using both $TPR/\dot{m}_{inlet\ corr.}$ and work factor parameters to choose that point. The efficiency of the point chosen using work factor shows the same general trend as the nominal clearance efficiency, but there are some slight differences, such as the peak at 95% corrected speed and then the decrease to 100% corrected speed. The efficiency of the point chosen with $TPR/\dot{m}_{inlet\ corr.}$, however, shows a very similar trend to that of the nominal clearance. Because of this, $TPR/\dot{m}_{inlet\ corr.}$ was chosen as the parameter to use when selecting data points with two different tip clearances.

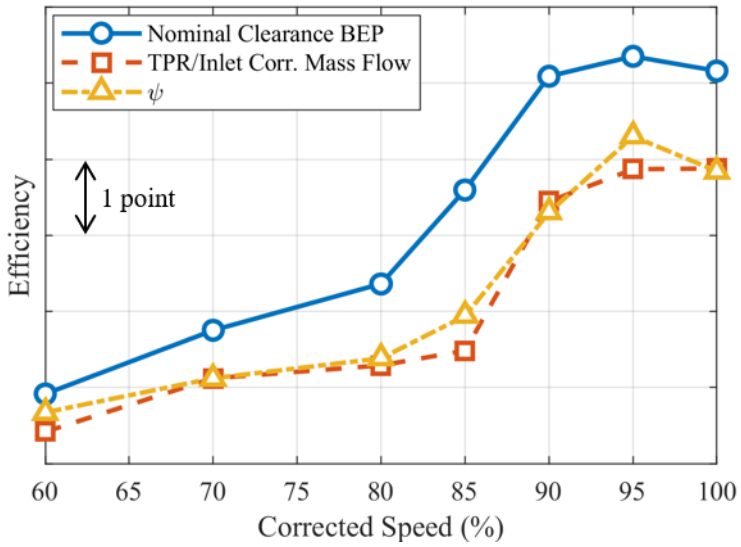

Figure 4.7 Points chosen at each speed using the closest points for TPR/inlet corrected mass flow and work factor

4.2 Experimental Tip Clearance Effects and Sensitivities

Using $TPR/\dot{m}_{inlet\ corr.}$ as the parameter to match when comparing points with different axial tip clearances, a stage and component performance analysis is performed to determine how the stage, impeller, and diffuser are affected by the change in tip clearance. The sensitivities for each parameter will all have the same general form

$$-\Delta B = k\ CR \tag{4.1}$$

where the variable B is the performance parameter, such as total pressure ratio, efficiency, or static pressure rise coefficient, CR is the tip clearance ratio defined by the tip clearance divided by the blade height at the impeller exit and given as a percent, and k is the slope of the line. This linear trend will define the change in the percent decrease of the performance parameter from the extrapolated value at a zero tip clearance as a function of the clearance ratio.

4.2.1 Stage Performance and Sensitivity

As noted in Section 1.3.1, the effects on performance have been well documented. With a decreasing tip clearance, the total pressure ratio and efficiency both increase while the work input,

represented as either a work factor or total temperature ratio, is constant with only a slight increase at speeds near the design speed. The SSCC follows the same trends in the literature, as shown by the total pressure map in Figure 2.6 and the efficiency map in Figure 2.7 in Section 2.1.5. However, the sensitivity of each parameter with respect to the tip clearance is also analyzed here.

For each speedline, the total pressure ratio increases as the tip clearance is decreased. At 60% corrected speed, there is a total pressure ratio increase of 1.3% when decreasing the tip clearance from the larger value to the nominal value. At 80% corrected speed, that percent increase in total pressure ratio is 2.4% and increases to a maximum increase of 4.2% at 85% corrected speed. The increase in total pressure ratio is consistently larger at the higher speeds and is 3.7% at the design speed of the compressor.

The total pressure ratio sensitivity to the tip clearance is shown in Figure 4.8 and illustrates the expected results. As the corrected speed increases up to 85% corrected speed, the total pressure ratio becomes more sensitive to changing tip clearance, with the exception at 70% speed, which has a lower sensitivity than all the other speeds. This is due to the experimental points being more sparsely spaced. Most of the other speeds have points on the larger clearance speedline that more closely match the $TPR/\dot{m}_{inlet\ corr.}$ value from the nominal clearance anchor point. The closest point with respect to $TPR/\dot{m}_{inlet\ corr.}$ on the larger clearance speedline at 70% is slightly farther away and has a higher value of the loading factor thus causing an artificially low trend with tip clearance. At 100% speed, the two data points are closer with respect to the loading factor than at 70% speed, but still farther apart than the other speeds. However, the closest larger clearance point to the nominal clearance anchor point at 100% speed has a lower value of loading factor, increasing the trend slightly from the trend if the loading factor were matched exactly.

Above 85% corrected speed, the trends are all very similar with slight changes. A smaller tip clearance at higher speeds will result in a more drastic change to the total pressure ratio than at lower speeds. The slopes of the lines – indicating exactly how sensitive the total pressure ratio is to the tip clearance ratio – are illustrated in Figure 4.11.

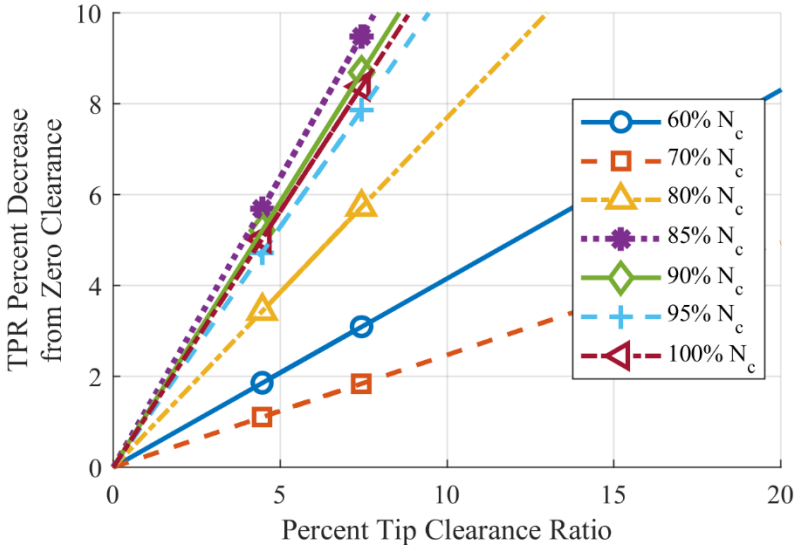

Figure 4.8 Total pressure ratio sensitivity at various corrected speeds

The noticeable increase in total pressure ratio sensitivity that occurs between 80% and 85% corrected speed is most likely due to the inducer of the compressor entering the transonic regime. A shock forms in the inducer around 85% corrected speed that significantly affects the internal flow field. The change in the flow field causes the shift in performance and sensitivity of the total pressure ratio. However, once the compressor has entered the transonic regime, the total pressure ratio sensitivity is approximately constant with small decreases through 95% corrected speed and then a small increase to 100% corrected speed.

Similar results exist for the stage efficiency as they do for the stage total pressure ratio. The efficiency is increased as the tip clearance is decreased for all speedlines, and the sensitivity of the efficiency shows a similar trend to the total pressure ratio. There is a percent increase in efficiency of 0.7% when decreasing the tip clearance from the larger value to the nominal value at 60% corrected speed. The percent increase continues to rise when it reaches its maximum at 85% corrected speed. At this speed, the efficiency is increased by 2.8% from the larger clearance to the nominal clearance. As the speed is then increased to 100% corrected speed, there is a decrease in the percent increase with the efficiency showing a 1.7% increase at the design speed. This is similar to the total pressure ratio because the maximum also occurs at 85% corrected speed. It is different though, because the percent increase in efficiency decreases more significantly between 85% and

100% corrected speed whereas the total pressure ratio decreases slightly and then stays approximately constant.

This trend is also depicted in Figure 4.9, the sensitivity of the efficiency to the tip clearance. The sensitivity increases between 60% and 80% corrected speed, increases sharply to 85% corrected speed, and then decreases to 100% corrected speed. This behavior is most likely occurring because of the shock formation in the inducer of the impeller at 85% corrected speed, which is causing the sensitivity of the efficiency to considerably increase. After the shock has formed and as it is becoming stronger however, the sensitivity then begins to decrease, and the tip clearance has less of an effect on the efficiency of the stage as the strength of the shock increases. The slopes of efficiency shown in Figure 4.11 also illustrate this point.

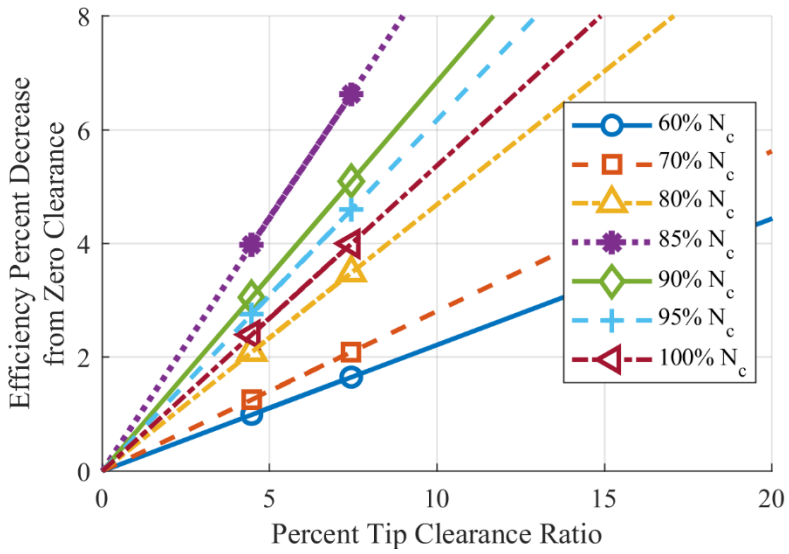

Figure 4.9 Efficiency sensitivity at various corrected speeds

The work input into the compressor is determined using the work factor, ψ. The work factor is consistent and does not change much with speed. The largest percent increase from the larger tip clearance to the nominal tip clearance is about 1%, which occurs at 60% corrected speed, although the change is very similar (0.9%) at 100% corrected speed. The smallest change happens at 70% corrected speed where the work factor decreases by 0.1%, staying approximately constant as the tip clearance is decreased. The other speeds all have similar percent increases that range from 0.5% to 0.75%.

The sensitivity in the work factor is shown in Figure 4.10 and the slopes for each speed are plotted in Figure 4.11. There is no discernible trend for the work factor with speed as the work factor is the most sensitive at 60% corrected speed, followed closely by 100% corrected speed. Because most of the percent changes between tip clearances at different speeds are very similar, the slopes in Figure 4.10 are also similar. The one exception is 70% corrected speed, where the slope is slightly negative, indicating that the work factor decreases a very small amount with decreasing tip clearance. This is due to the two tip clearance data points being used at 70% speed being slightly farther apart with respect to the loading factor, $TPR/\dot{m}_{inlet\ corr.}$. The other speeds though, show that more work is needed for smaller tip clearances. Lastly, the total pressure ratio and efficiency sensitivities showed a significant change when the shock in the inducer of the impeller formed, but the work factor shows no trends associated with that formation. Therefore, the work input is not affected by the shock like the total pressure ratio and efficiency.

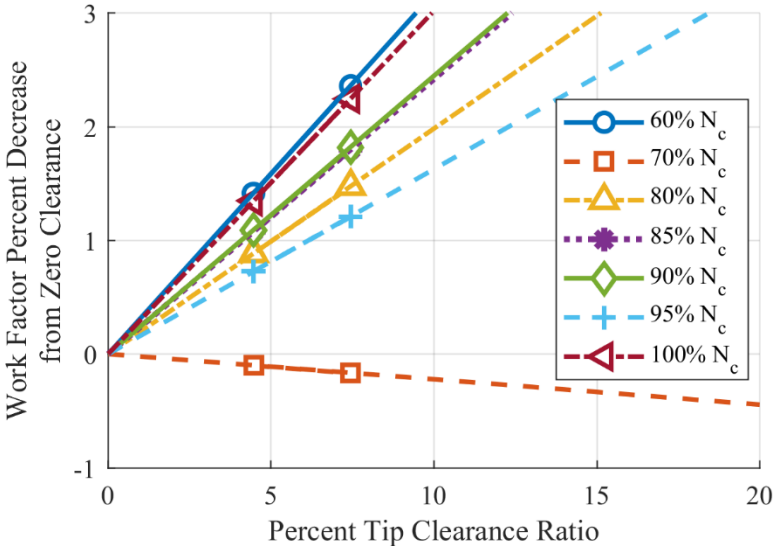

Figure 4.10 Work factor sensitivity at various corrected speeds

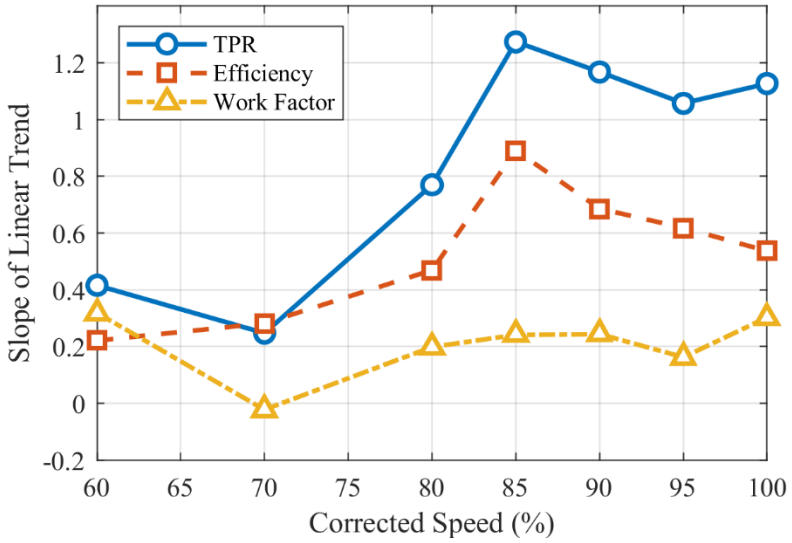

Figure 4.11 Sensitivity slopes for stage performance parameters

4.2.2 Impeller Performance and Sensitivity

A decreasing tip clearance improves the stage performance, but it is not clear how much each of the components contributes to this increase. This section will address the tip clearance effects on the impeller performance and the sensitivity of the impeller to the tip clearance.

The impeller performance is typically quantified by two parameters, the impeller total pressure ratio and the impeller efficiency. Details for these calculations are in Section 2.1.4 but as there are no total pressure or temperature probes at the exit of the impeller, each quantity is calculated from given information such as impeller trailing edge static pressure and the assumption that the total temperature does not change through the diffuser and deswirl during steady operation. Another characteristic to compare the impeller performance at different tip clearances is the static pressure rise through the impeller. As the speed increases and the tip clearance decreases, the static pressure rise through the impeller will increase.

The impeller total pressure ratio, like the stage total pressure ratio, increases with speed and decreasing tip clearance. The impeller total pressure ratio is significantly more sensitive than the stage total pressure ratio but shows the same trend. At 60% corrected speed, the impeller total pressure ratio increase is 1.7%, about a half percent higher than the stage at the same speed. The maximum percent difference for the impeller total pressure ratio also occurs at 85% corrected

speed but the increase is 5.3% whereas the stage increased about 4%. The increase at 100% corrected speed is 4.4% for the impeller total pressure ratio, slightly decreasing from maximum sensitivity in the same way that the stage total pressure ratio did.

These trends are also shown in Figure 4.12, illustrating the sensitivity of the impeller total pressure ratio. It is similar to the sensitivity plot for the stage total pressure ratio but with larger percent decreases from the zero tip clearance case. Consequently, the slopes of the impeller total pressure ratio sensitivity, which are shown in Figure 4.14, are larger. The sensitivity of the impeller total pressure ratio increases dramatically between 80% and 85% corrected speed, where it reaches a maximum. Beyond 85% corrected speed, similar results for the impeller total pressure ratio exist as they do for the stage total pressure ratio. While the sensitivity above 85% corrected speed slightly decreases, the slopes are all very similar magnitudes.

The effect of the shock in the inducer of the impeller is very strong on the impeller total pressure ratio. Once the shock forms, the sensitivity greatly increases to where the larger tip clearance is producing approximately 10% - 13% less of a total pressure rise than the extrapolated value at a zero tip clearance. However, Figure 4.12 shows that once the inducer is transonic, the sensitivity does not change much. There is a minor decrease as the strength of the shock increases, but the 95% and 100% corrected speed sensitivities are similar.

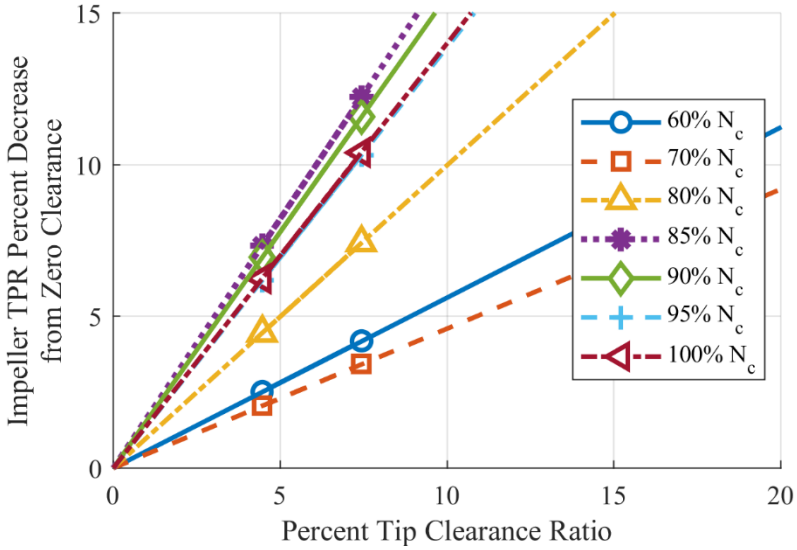

Figure 4.12 Impeller total pressure ratio sensitivity at various corrected speeds

The impeller efficiency compares to the stage efficiency in the same way that the impeller total pressure ratio compares to the stage total pressure ratio. The impeller efficiency shows similar trends to the stage efficiency but with increased sensitivity. A 1% increase in impeller efficiency is observed at 60% corrected speed by decreasing the tip clearance from the larger value to the nominal value, compared to a 0.7% increase in stage efficiency. The percent change continues to increase slowly until 80% corrected speed when the increase to 85% corrected speed is much larger. As with the stage efficiency, the impeller efficiency also experiences a maximum percent change at 85% corrected speed, but it is larger than that of the stage efficiency. There is a percent increase of 3.4% in impeller efficiency between the two tip clearances but only a 2.8% increase in stage efficiency. The percent change continues to decrease as the speed increases from 85% to 100% corrected speed. The percent increase at the design speed is 2.1% for the impeller efficiency compared to 1.6% for the stage efficiency.

The sensitivity of the impeller efficiency from a zero tip clearance shows the same trend as the stage efficiency too but with larger sensitivities. The sensitivities are shown in Figure 4.13 and the slopes in Figure 4.14. At 85% corrected speed, the sensitivity is the largest with about an 8% change for the larger clearance and a 5% change for the nominal clearance from the extrapolated impeller efficiency at a zero tip clearance. The shock formation in the inducer of the impeller also has a very strong effect on the impeller efficiency near the speed at which the shock forms. Once the shock has formed and becomes stronger though, the sensitivity at the design speed starts to decrease and is similar in value to the sensitivity at 80% corrected speed. This characteristic is very similar to that from the stage efficiency, where the sensitivity is a maximum at 85% corrected speed and then decreases similar amounts between each speed up to 100% corrected speed.

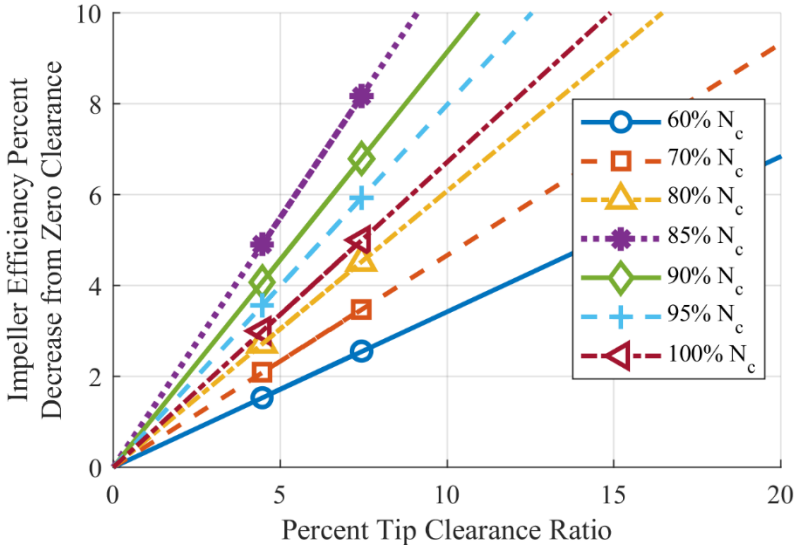

Figure 4.13 Impeller efficiency sensitivity at various corrected speeds

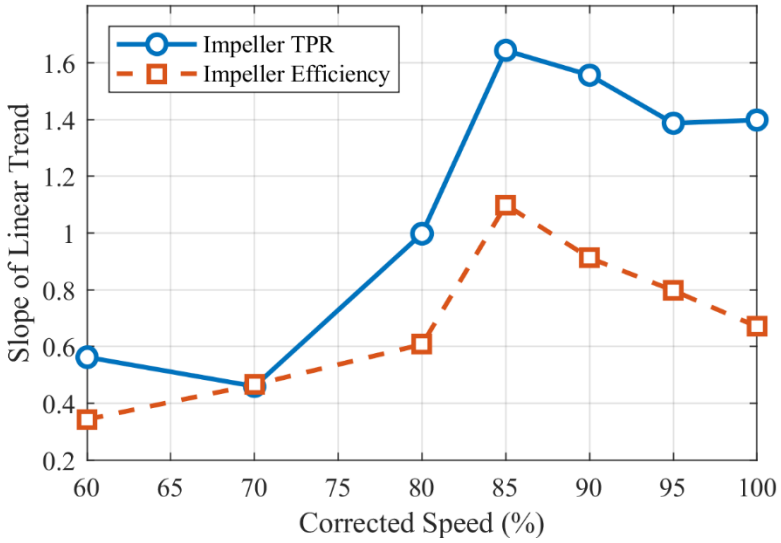

Figure 4.14 Sensitivity slopes for impeller performance parameters

Finally, the static pressure rise through the impeller is compared for each tip clearance. The static pressure rise distribution is shown in Figure 4.15. As expected, the smaller tip clearance results in a better static pressure rise through the impeller with a higher exit static pressure. Most of the additional static pressure gained occurs in the exducer of the impeller. Because the impeller is moved axially to set the desired tip clearance, there is not much change in the tip clearance at

the inducer of the impeller leading to similar static pressure distributions there. But by reducing the axial tip clearance, the effects of the tip leakage flow are reduced in the exducer resulting in better overall impeller performance and increased static pressure rise.

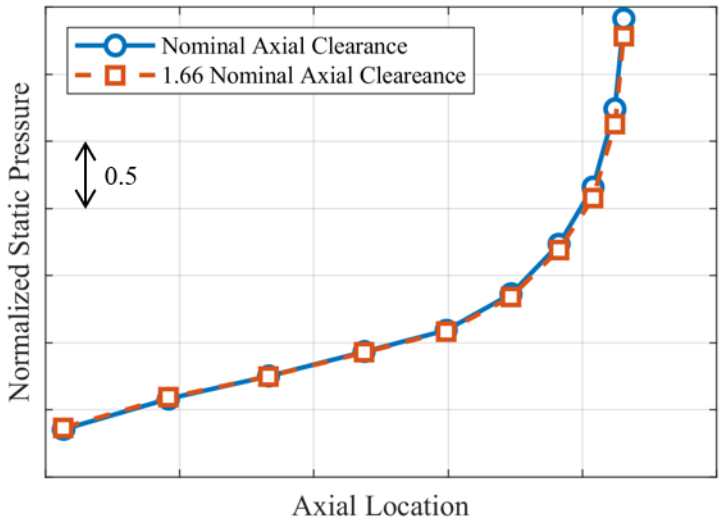

Figure 4.15 Comparison of impeller static pressure rise for each tip clearance

4.2.3 Diffuser Performance and Sensitivity

A smaller tip clearance increases the performance of the impeller, but its effect on the diffuser is important to understand because the flow exiting the diffuser (or the stationary diffusion system) will be entering the combustor in an engine. Providing a uniform flow with as few losses as possible and a greater static pressure will benefit the performance of the combustor. Diffuser performance is typically characterized by three coefficients, the diffuser static pressure recovery coefficient, the total pressure loss coefficient, and the diffuser effectiveness. Additionally, the rise in static pressure through the diffuser will also be compared.

The diffuser static pressure recovery coefficient (C_p) is a measure of the increase in static pressure through diffuser with respect to the dynamic pressure entering the diffuser. The static pressure rise shows the opposite trend from the impeller and the stage performance. For a given speed, the nominal tip clearance C_p is less than that of the larger tip clearance. At 60% corrected speed, the value of C_p decreases by 0.9% from the larger tip clearance to the nominal tip clearance. The percent change increases at 70% corrected speed but then decreases from 70% to 80%

corrected speed. Like the previous impeller and stage performance parameters, the percent change at 85% corrected speed is the maximum. The static pressure recovery is decreased by 4.7% from the larger to the nominal tip clearance at this maximum. The percent change at 90% corrected speed decreases by a small amount but is still a similar magnitude. From 90% to 100% corrected speed though, the percent decrease becomes significantly smaller.

Figure 4.16 illustrates these same trends but when compared to the extrapolated value at a zero tip clearance. The maximum sensitivity occurs at 85% corrected speed with the 90% corrected speed sensitivity slightly below. There are significant decreases between the sensitivities at 90% and 95% corrected speed and between 95% and 100% corrected speed. These trends are also shown in Figure 4.19, which plots the value of the slope for each speed. The transonic impeller flow significantly affects the diffuser performance as the sensitivities increase quickly once the shock has formed and then decrease again as the shock becomes stronger and more stable. However, the fact that the static pressure recovery is worse at the nominal tip clearance when compared to the larger tip clearance is not a byproduct of the impeller entering the transonic regime. At speeds both below and above the critical speed where the impeller becomes transonic, the value of C_p is better at the larger tip clearance.

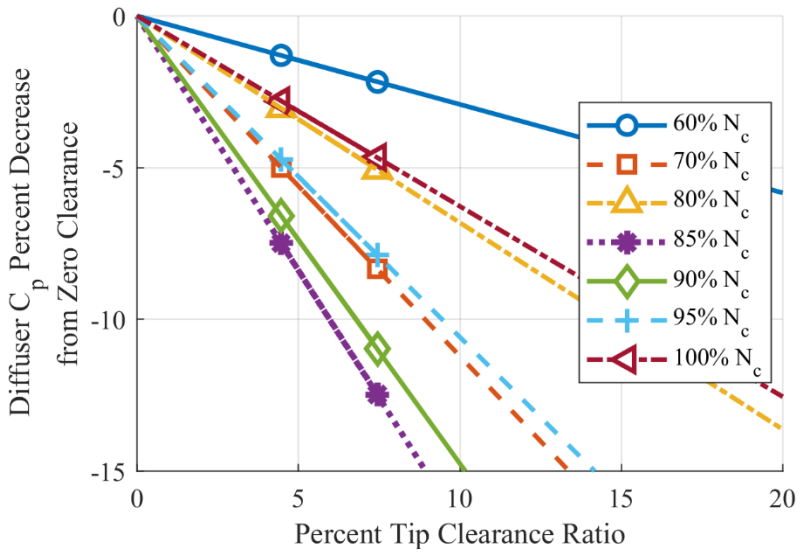

Figure 4.16 Diffuser C_p sensitivity at various corrected speeds

The total pressure loss coefficient (K) through the diffuser is calculated like the static pressure recovery but using the total pressure change between the impeller exit and diffuser exit instead of the static pressure change. The changes between the nominal and larger tip clearances also show the same trends too. At 60% corrected speed, the total pressure loss coefficient is 3.4% lower at the larger clearance than at the nominal clearance. The change in the value of K continues to increase to 4.1% at 80% corrected speed before the increase associated with the transonic impeller. The K value at the nominal clearance at 85% corrected speed is 6.7% larger than that at the larger tip clearance. There is then a small increase to 6.8% change at 90% corrected speed before decreasing to 95% and 100% corrected speed. At the design speed, the total pressure loss is 4.7% larger at the nominal clearance.

The sensitivity of the total pressure loss coefficient through the diffuser is depicted in Figure 4.17. The definition of K includes an absolute value of the difference of total pressures between the diffuser exit and the impeller exit so that while the total pressure loss increases with decreasing tip clearance, the slopes appear positive because the extrapolated value is greater than both of the measured values. The values of the slopes for K are illustrated in Figure 4.19. The lower speeds, 60% - 80% corrected speed, show very similar sensitivities on the lower end of the range presented. The sensitivities at 85% and 90% corrected speeds sharply increase but then decrease to 95% and 100% corrected speeds. The total pressure loss coefficient is also very sensitive around the speed where the impeller develops the shock in the inducer but becomes less sensitive as the impeller starts to become more stable in the transonic regime. Like the static pressure rise coefficient though, the impeller going from subsonic to transonic influences the sensitivity, but the total pressure loss coefficient increases with decreasing tip clearance both below and above the transition speed.

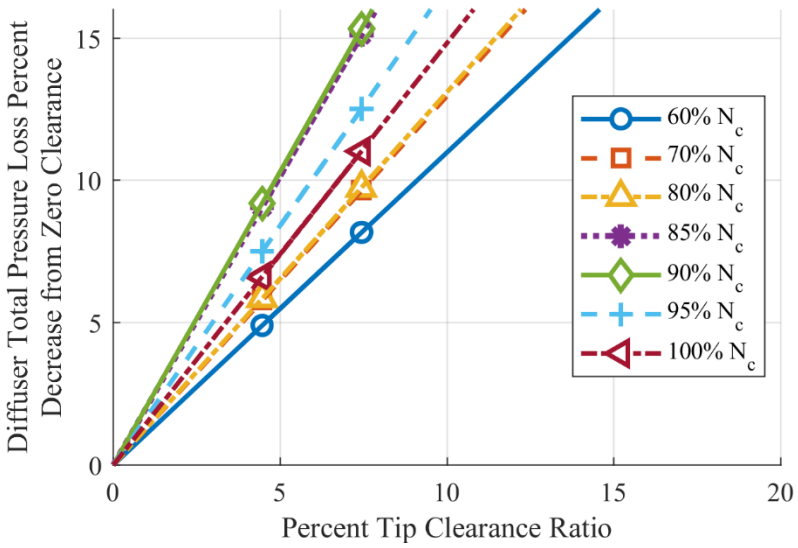

Figure 4.17 Diffuser total pressure loss sensitivity at various corrected speeds

Diffuser effectiveness (η_{diff}) is a measure of the actual static pressure recovery compared to the ideal static pressure recovery, which can be approximated by adding the actual static pressure recovery coefficient to the total pressure loss coefficient. The diffuser effectiveness follows similar trends to the static pressure rise coefficient. Because the static pressure recovery was better at the larger tip clearance, the diffuser is more effective at the larger tip clearance too. The percent decrease from the larger clearance to the nominal clearance ranges between 1.4% and 2.3% between 60% and 80% corrected speed. At 85% corrected speed, the diffuser effectiveness decreases by 4.2% between the two tip clearances, which is the maximum. A steady decrease in magnitude occurs from 85% to 100% corrected speed. The design speed percent decrease is 2.2%.

The sensitivity of the diffuser effectiveness to the decrease in tip clearance is shown in Figure 4.18. These trends are also similar to those from the static pressure rise coefficient. At the lower speeds, the sensitivity is smaller, but greatly increases between 80% and 85% corrected speed. At 90% corrected speed, the sensitivity is only slightly smaller than that at 85% corrected speed but increasing speed beyond 90% results in sizeable decreases to the sensitivity. The results here are expected because of the results from the static pressure recovery and the total pressure loss. Once the impeller is transonic, the sensitivity increases initially but then decreases as the shock becomes stronger. The slopes for the diffuser effectiveness sensitivity are shown in Figure 4.19.

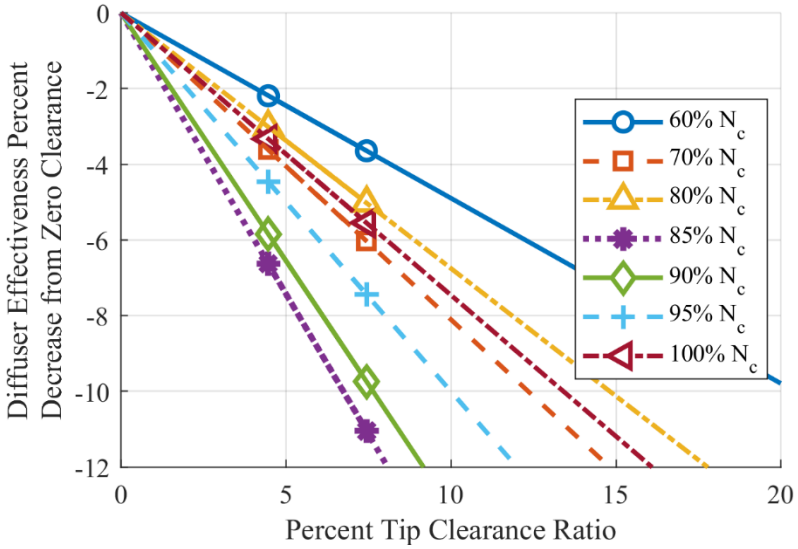

Figure 4.18 Diffuser effectiveness sensitivity at various corrected speeds

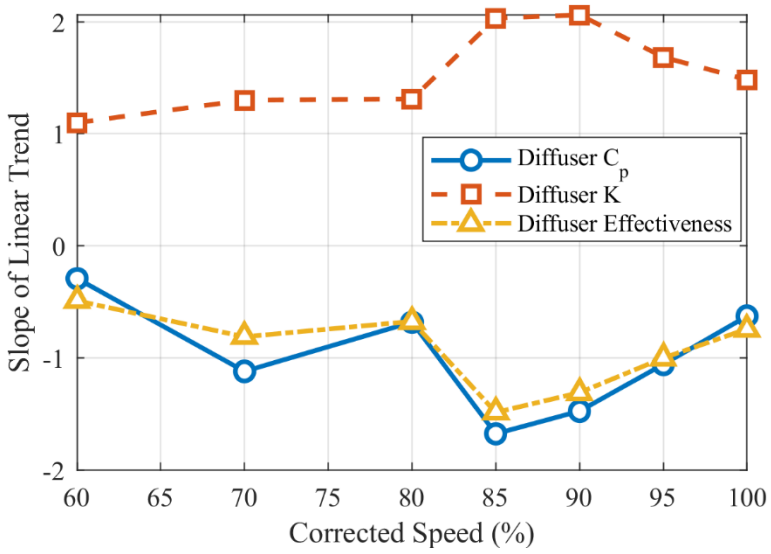

Figure 4.19 Sensitivity slopes for diffuser performance parameters

The static pressure rise through the diffuser at the various instrumented points from the impeller trailing edge through the diffuser trailing edge is shown in Figure 4.20. As stated in the previous section, operation at the nominal tip clearance provides a larger static pressure at the impeller exit, station 2. The static pressure rise through the vaneless space, from stations 2 to 3, is very similar for both tip clearances, but differences start to emerge when going from the diffuser

leading edge to the diffuser throat. There is a more substantial static pressure rise between the leading edge and throat when operating with the nominal tip clearance, and this difference stays nearly constant through the rest of the diffuser passage. One of the most important sections of the diffuser is shown to be between the leading edge and the throat as that is where a significant portion of the static pressure rise occurs. The diffuser inlet profile is also very important as a greater static pressure rise can be achieved by reducing the tip clearance thereby reducing the tip leakage flow and its effects on the overall impeller exit flow profile.

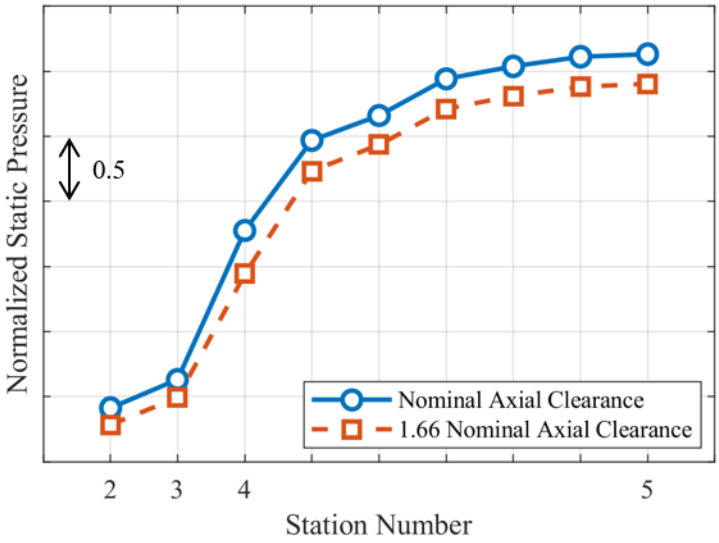

Figure 4.20 Diffuser static pressure rise comparison

The trends in the static pressure rise and total pressure loss coefficients as well as the diffuser effectiveness are opposite from the expected trends. As the impeller tip clearance is closed to a smaller value, the effect of the tip leakage flow on the impeller exit flow is reduced and performance of the diffuser increased, as evidenced by the diffuser static pressure rise in Figure 4.20. However, the diffuser performance coefficients decrease as the tip clearance decreases from the larger to the nominal tip clearance. Because the tip clearance affects the flow exiting the impeller and thus, the diffuser inlet flow field, the matching between the impeller and diffuser peak performance points is investigated.

Matching an impeller and a diffuser can be difficult as there are multiple methods for determining matching conditions. Many authors agree that the incidence on to the diffuser vane is

the most important factor when determining matching conditions and diffuser performance (Everitt et al., 2017; Shum et al., 2000). However, only an estimate of the diffuser incidence can be made with the experimental data by assuming an ideal impeller exit flow angle and no change in the angle through the vaneless space. Instead, a method proposed by Klassen (1977a) using the mass flow – speed parameter is used. The mass flow – speed parameter is defined as

$$\Omega = \frac{\dot{m}_c}{N_c} \tag{4.2}$$

where $\dot{m}_c$ is the inlet corrected mass flow rate and N_c is the corrected speed. The mass flow – speed parameter will be normalized by the value of the parameter at the design point.

To evaluate the matching of the impeller and the diffuser at the peak performance, the mass flow – speed parameter is evaluated at three points per speedline, the peak stage efficiency point, the peak impeller efficiency point, and the peak diffuser effectiveness point. The desired result is for each component and the stage to be operating at the peak performance at the same point on the speedline. Figure 4.21 shows the normalized mass flow – speed parameter for each peak performance point for the nominal clearance on the left and the larger clearance on the right. The nominal clearance shows that the impeller peak efficiency point occurs at a higher mass flow rate (for a given speed) than the peak stage efficiency and that the peak diffuser effectiveness point occurs at a lower mass flow rate. This trend continues until 85% corrected speed where the stage and diffuser points are the same, but the impeller peak efficiency is still occurring at a higher mass flow rate. However, at 100% corrected speed, the peak points for the stage, impeller, and diffuser are all the same point, indicating that the impeller and diffuser are both operating at peak performance at the same point. The same plot for the larger tip clearance case is also shown on the right of Figure 4.21. The impeller peak efficiency point is also occurring at a higher mass flow rate for the entire range of speeds except for at 100% corrected speed, where it occurs at a lower mass flow rate than both the stage and diffuser peak points. The stage and diffuser peak points match at some speeds between 60% and 100% corrected speed, but all three points never match using the larger tip clearance. These results confirm that the impeller and diffuser are operating near the peak efficiency point and the peak effectiveness point, respectively, at the design point and that this is not causing the diffuser to operate more effectively at the larger impeller tip clearance.

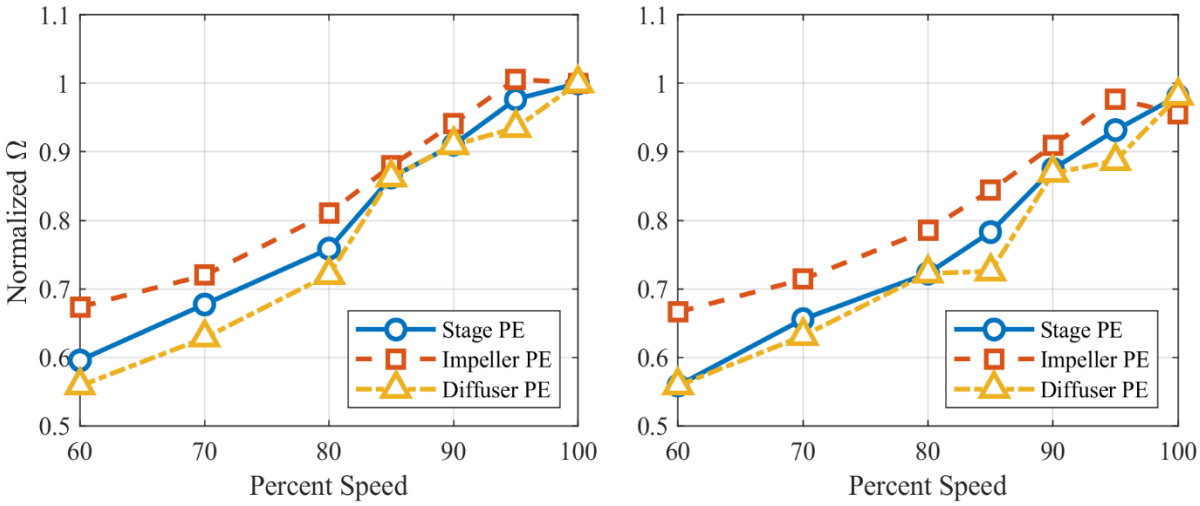

Figure 4.21 Mass flow - speed parameter evaluation for the nominal clearance (left) and the larger clearance (right)

Because the impeller is operating at the maximum efficiency at the same point that the diffuser is operating at minimum loss, the quantities in the numerator and the denominator of the diffuser static pressure rise coefficient are examined. The numerator is the static pressure rise between the diffuser trailing edge and the impeller trailing edge and the denominator is the impeller exit dynamic pressure. The diffuser provides a better static pressure rise at the nominal tip clearance, but the impeller dynamic pressure also increases with decreasing tip clearance. Figure 4.22 shows the size of the change in the impeller dynamic pressure and the diffuser static pressure rise between tip clearances. Changing the tip clearance from the larger clearance to the nominal clearance results in an increase of about 1.35 psi in the diffuser static pressure rise, however, that same change in tip clearance increases the impeller dynamic pressure by over 3 psi. Therefore, the decrease in the diffuser C_p between tip clearances is being caused by a larger increase in the impeller dynamic pressure than the increase in diffuser static pressure rise. At the larger tip clearance, the impeller performance suffers so the diffuser must do more to diffuse the flow. At the nominal tip clearance, the impeller is doing more of the static pressure rise so the diffuser does not have to do as much. The same is true for the diffuser total pressure loss coefficient. It is also normalized by the impeller dynamic pressure and its increase is larger than the decreased total pressure loss between tip clearances. In addition, the diffuser effectiveness is smaller at the nominal tip clearance because the impeller dynamic pressure is increased, and the diffuser is

converting a smaller percentage of the total pressure to static pressure. However, the overall static pressure rise increases in both the impeller and the diffuser. At the nominal clearance, the impeller diffuses the flow more and generates more static pressure leaving the diffuser needing to provide less static pressure rise to accomplish the overall performance of the compressor.

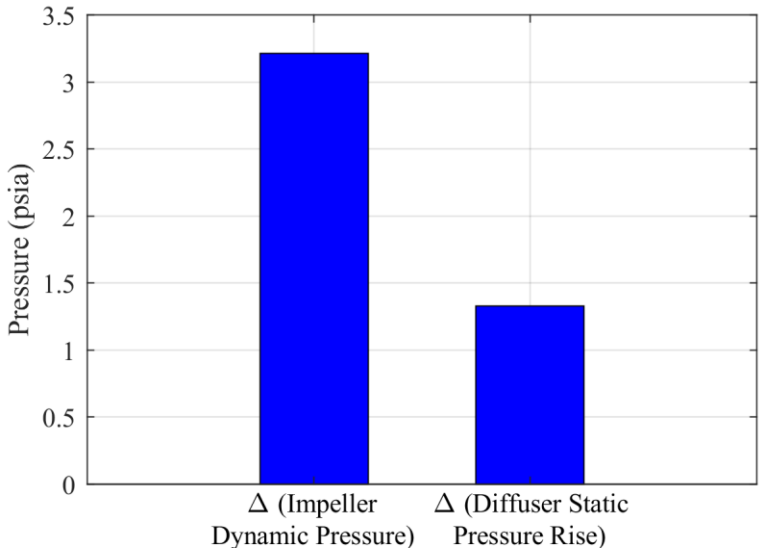

Figure 4.22 Tip clearance differences in diffuser pressure quantities

4.3 Experimental and Computational Tip Clearance Comparison

The ability of the computational model to predict the change in performance and trends in tip clearance sensitivity at the design speed will now be evaluated against the experimental data. The same method that is used in the previous section will be used here, following the same general form as equation (4.1). Because the clearance ratio is the same between the experiment and the numerical model, the slope will be the most important comparison. For the evaluation of the trends, the same points used for the experimental comparison will also be used for the numerical comparison. All sensitivity plots are shown on the same scale as those from the previous sections.

4.3.1 Stage Performance and Sensitivity

Tip clearance effects on the stage total pressure ratio are predicted well by the numerical simulation. Figure 4.23 shows the total pressure ratio map for both tip clearances for the experimental data and the numerical simulation. The total pressure ratio and the choked mass flow

rate are overpredicted for both tip clearances but the change in total pressure ratio between the two tip clearances for the numerical results and the experimental data is very similar. The shape of the upper half of the speedline from the numerical simulation appears to be a little flatter than that from the experiment, but it still matches well. Figure 4.24 depicts the total pressure ratio percent decrease from the extrapolated value at zero tip clearance for both the numerical simulation and the experiment. The trend for the numerical simulation matches well with that from the experiment. The slope is 1.127 for the experiment at the design speed and the numerical simulation predicts a slope of 1.196. There is a slight overprediction in the sensitivity, but the results are very close.

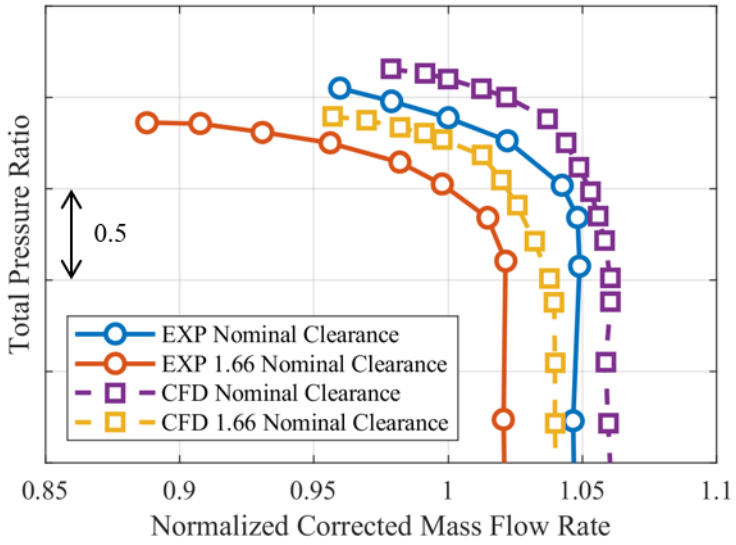

Figure 4.23 Stage total pressure ratio map comparison

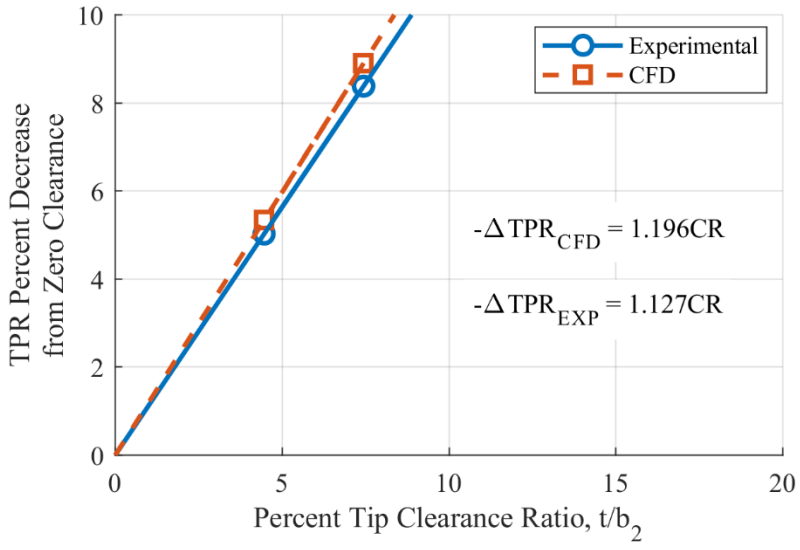

Figure 4.24 Total pressure ratio sensitivity at design speed

The effects of tip clearance on the efficiency are also similarly predicted. As with the total pressure ratio, the stage efficiency is also overpredicted for both tip clearances, as shown in Figure 4.25. The shape of each efficiency speedline is not predicted as well. The sharp knee in the experimental speedlines is not replicated by the numerical simulation and the upper half of the experimental speedline shows an increase to and a decrease from the peak efficiency point whereas the numerical simulation shows a flatter efficiency around the peak efficiency point before decreasing. The numerical simulation for the larger tip clearance is predicting an efficiency that is very close to the nominal tip clearance experimental efficiency. The nominal tip clearance numerical simulation efficiency is also increased by a similar amount. This trend is better illustrated in Figure 4.26, where the percent decrease in efficiency from the extrapolated efficiency at a zero tip clearance is plotted. The efficiency trend is slightly underpredicted by the numerical simulation, a slope of 0.465 compared to 0.537 for the experiment. Therefore, the numerical simulation is predicting that the decrease in stage efficiency due to increasing tip clearance is smaller than the experimental decrease.

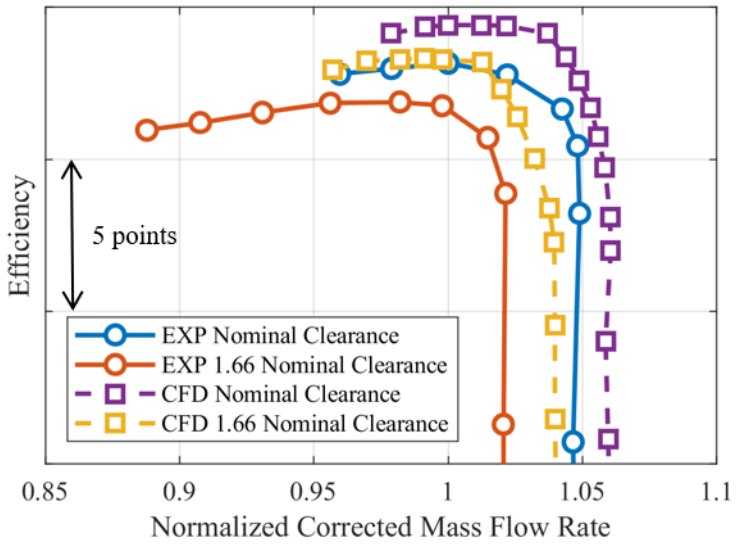

Figure 4.25 Stage efficiency map comparison

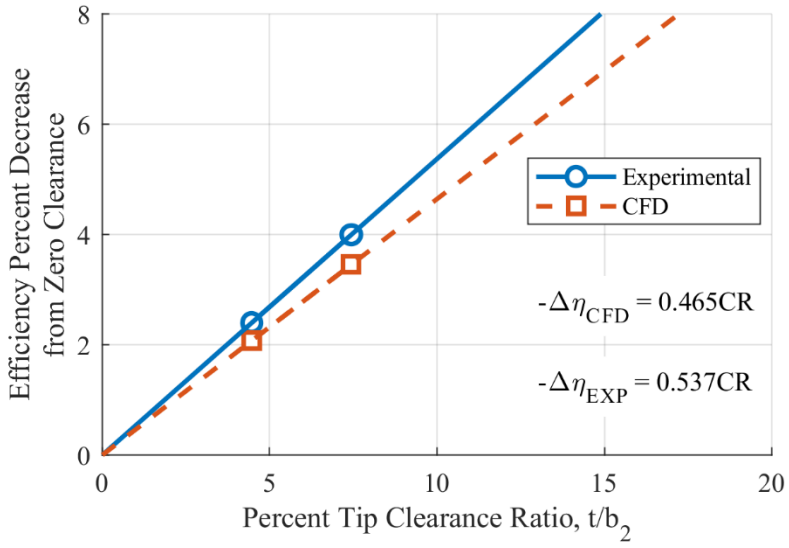

Figure 4.26 Efficiency sensitivity at design speed

The final stage performance parameter is the work factor. The tip clearance effects on the work factor are predicted well by the numerical simulation. The speedline for work factor is a straight line and the numerical simulation can predict this well, as evidenced by Figure 4.27. There is a minimal underprediction when comparing the work factor for the data points in the choked flow part of the speedline. This suggests that the work factor is underpredicted by a small amount

for both tip clearances using the numerical simulation. However, the trend of work factor decrease with increasing tip clearance is overpredicted according to Figure 4.28. The slope of the work factor decrease is 0.377 for the numerical simulation but 0.302 for the experiment. The numerical simulation predicts that increasing the tip clearance has a greater effect than it does in the experiment. Additionally, the work factor is the stage performance parameter that is the least sensitive to changes in tip clearance. This is proven by both the experimental data and the numerical model.

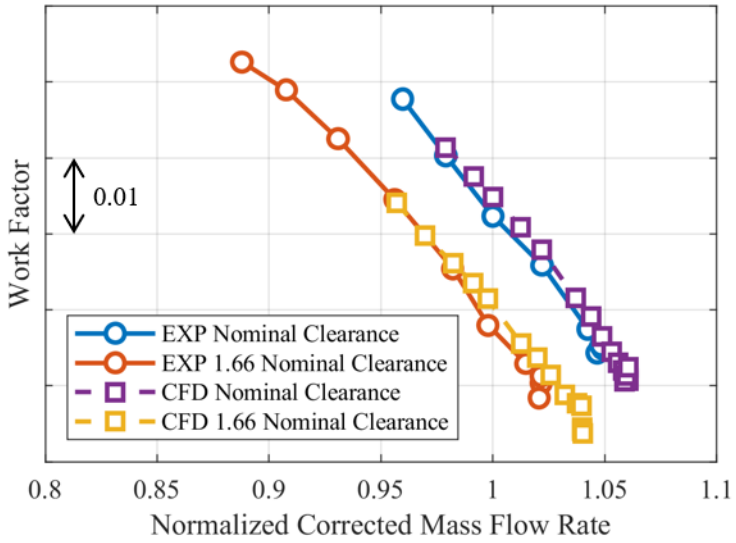

Figure 4.27 Work factor map comparison

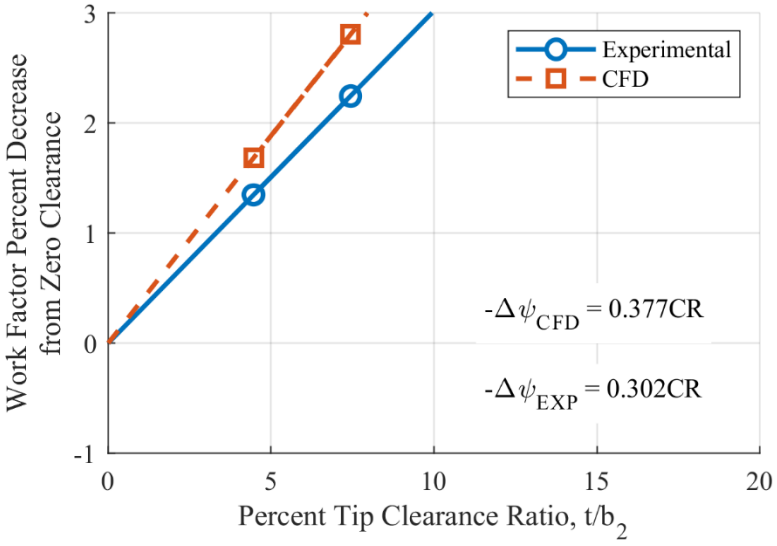

Figure 4.28 Work factor sensitivity at design speed

4.3.2 Impeller Performance and Sensitivity

The tip clearance effects on the impeller performance and sensitivity are predicted well by the numerical model. The impeller total pressure ratio speedlines for both tip clearances for the experiment and for the numerical simulation are shown in Figure 4.29. There is a small underprediction by the numerical simulation for both tip clearances, but the general shape of the speedline is matched well. Because the diffuser is controlling the choked flow, the impeller performance is constant in choke. As with the work factor, comparing the points in choke shows there is an underprediction in the impeller total pressure ratio. Due to the overprediction in mass flow rate though, the numerical and experimental speedlines appear to line up very well. The sensitivity of the impeller total pressure ratio to the tip clearance is predicted exactly, as shown in Figure 4.30. The slope for both the experiment and the numerical simulation is 1.398. Although the actual impeller performance is not quite simulated correctly, the impeller total pressure ratio percent decrease due to increasing tip clearance is matched exactly.

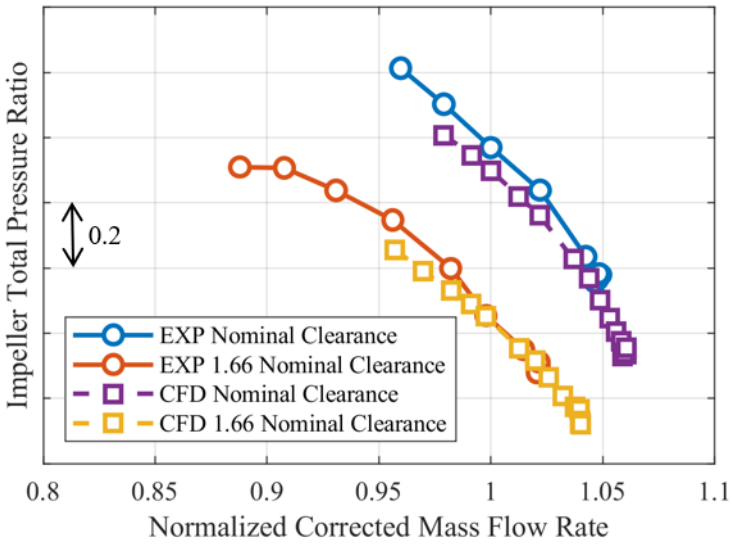

Figure 4.29 Impeller total pressure ratio map comparison

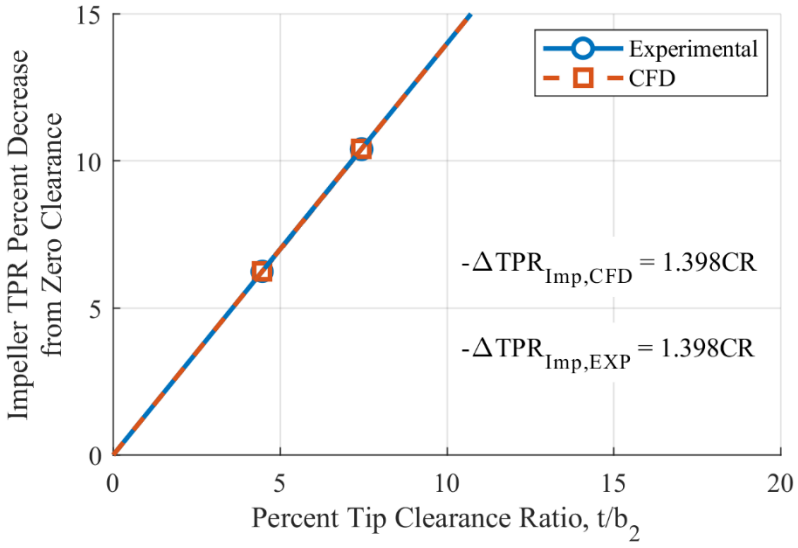

Figure 4.30 Impeller total pressure ratio sensitivity at design speed

The impeller efficiency is predicted well, but not quite as well as the impeller total pressure ratio. Figure 4.31 shows that both tip clearance speedlines are underpredicted by the numerical simulation, but the underprediction at the nominal clearance is larger. The shape of each speedline is also reasonably well predicted. There is an increase in efficiency from choke up to the point of peak efficiency and then a decrease with decreasing mass flow rate. The numerical simulation

predicts the increase in impeller efficiency from choke up to the peak efficiency point but as the experimental impeller efficiency drops, the numerical simulation predicts nearly constant efficiency. Because the impeller efficiency is more closely predicted at the larger clearance than at the nominal clearance, the trend of the impeller efficiency with tip clearance is also underpredicted. Figure 4.32 illustrates this, where the trend of the impeller efficiency from the extrapolated value at zero clearance is shown. The slope from the experimental data is 0.671 but the slope is only 0.562 for the numerical simulation. The decrease in impeller efficiency from a zero clearance is, therefore, underpredicted by the numerical simulation.

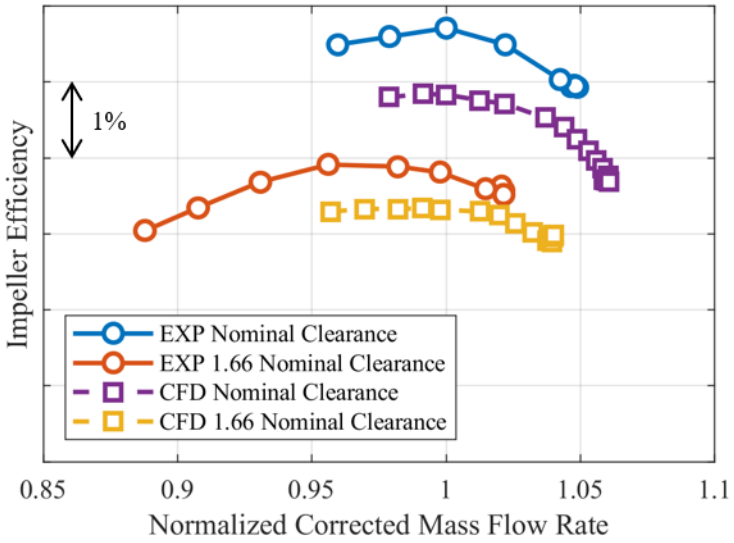

Figure 4.31 Impeller efficiency map comparison

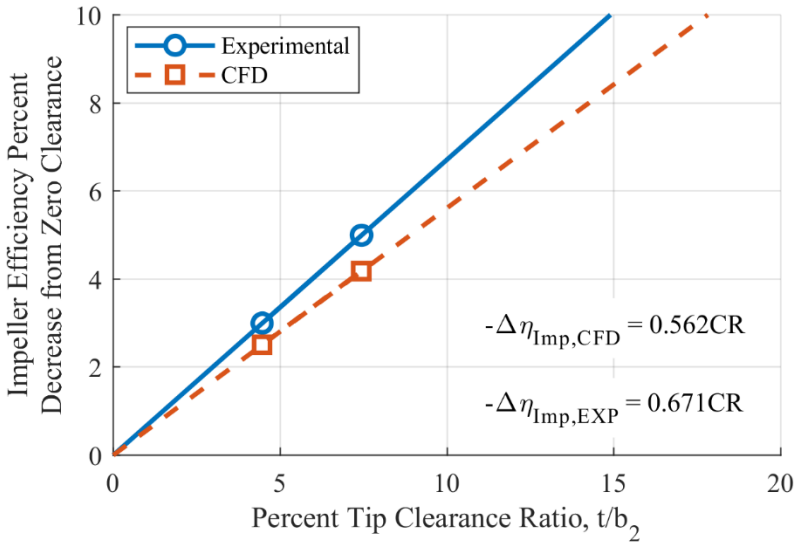

Figure 4.32 Impeller efficiency sensitivity at design speed

Additionally, the static pressure rise through the impeller for both tip clearances for the experiment and the numerical simulation is plotted on the same scales in Figure 4.33. Each static pressure rise distribution is from the operating points being used in the sensitivity analysis. There is very good agreement between both the experiment and the numerical simulation for the absolute pressure rise and the effects of the change in tip clearance. The numerical simulation marginally underpredicts the overall static pressure rise, but it matches well with the experiment. As discussed earlier, there are no changes in the pressure rise through the first half of the impeller because the tip clearance is not affected that much in the inducer. The differences start to become visible in the knee of the impeller and are most pronounced at the exducer of the impeller. This is captured very well in the numerical simulation where the differences in normalized static pressure rise between tip clearances at each point match well with those from the experiment.

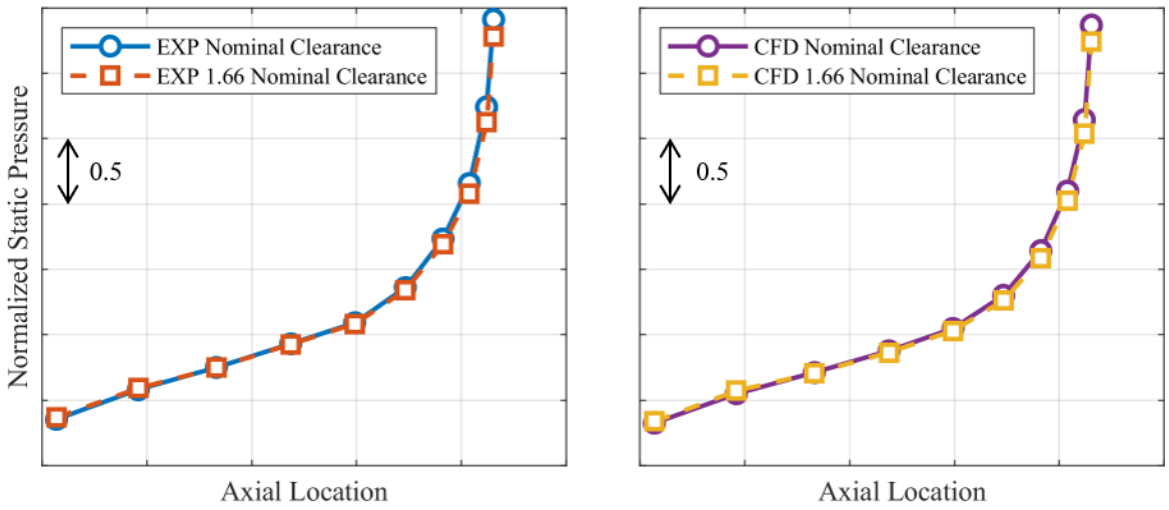

Figure 4.33 Comparison of impeller static pressure rise for the experiment (left) and numerical simulation (right)

Because the experimental data and the numerical simulation agree very well, some of the flow features in the impeller that are not accessible to instrumentation are investigated using the numerical model results. There was a significant increase in the impeller total pressure ratio by decreasing the tip clearance. Figure 4.34 shows the relative total pressure contours at the plane where the total pressure ratio is calculated experimentally. The nominal clearance is shown on the left and the larger clearance on the right. The scales for both graphs are the same. The main differences between the two exit profiles are mainly above 50% span. The hub regions in both passages one and two do not change much when changing the axial clearance. Near the shroud and blade tip regions though, there are significant differences. In passage one, there is a greater relative total pressure on the main blade side of the passage near the shroud region and a reduction in the lower relative total pressure region on the splitter blade side of the passage. Nominal tip clearance operation increases the size of the jet and decreases the size of the wake leaving each impeller passage. In passage two, there are similar results, but the differences are not as pronounced as those in passage one. There is an increased high-pressure region on the splitter blade side of passage two as well as a decreased low-pressure region on the main blade surface. The middle region is also increased in size indicating the expansion of the jet with the nominal tip clearance. Comparing the two passages for one clearance, the total pressure deficit in passage one is much larger than that in passage two, and one possible explanation is the tip leakage flow from the splitter

blade. When plotting streamlines that start in the tip clearance gap above both blades, a majority of the streamlines continue to circle the impeller in the tip gap, making it visually difficult to see the streamlines in each passage, but some do enter the main flow. The streamlines from the splitter blade tip gap mostly stay in passage one and exit the impeller in the upper half of the passage and closer to the suction surface of the splitter blade, leading to a larger total pressure deficit and a larger effect from reducing the tip clearance in this region. Below 50% span, each profile is very similar in both passages. While the axial clearance at the impeller exit is changed, the clearance in the inducer of the impeller does not change much with the axial movement of the impeller. Because of this, the formation of the tip leakage vortex at the leading edge of the blade is also not significantly affected. Therefore, the differences in relative total pressure resulting from the tip clearance are likely more evident in passage one than in passage two because most of the leading-edge tip leakage vortex will remain in passage two.

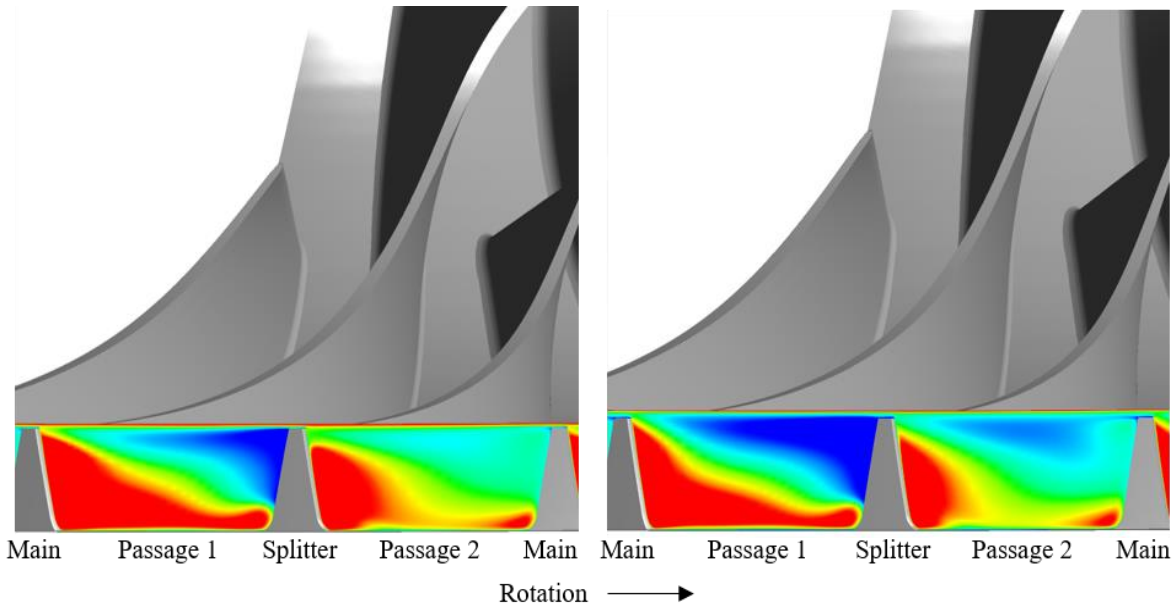

Figure 4.34 Impeller exit relative total pressure contours for the nominal clearance (left) and the larger clearance (right)

Figure 4.35 depicts the tip leakage vortex formation for both the nominal clearance on the left and the larger clearance on the right. The contours shown in the passage are static entropy, each using the same color scale so the entropy generation due to the tip leakage vortex can be identified. The results from each tip clearance are very similar because, as mentioned previously,

the tip clearance in the inducer does not change much with axial movement of the impeller. The tip leakage flow forms at the leading edge of the impeller and rolls up into a vortex very quickly, forming a small region of higher entropy near the shroud in the first plane. As the vortex progresses through the passage and reaches the second plane, the increased entropy has spread more circumferentially and stretches almost the entire passage instead of just the localized area as in the first plane. Continuing to follow the tip leakage vortex streamlines in Figure 4.36, oriented the same way and with the same color levels as Figure 4.35, the tip leakage flows are very similar through the rest of the passage. One of the main differences is the number of streamlines going to the right of the splitter blade. The nominal clearance has less streamlines crossing into the neighboring passage at the leading edge of the splitter blade, leading to the indication that the angle at which the tip leakage vortex is forming is changing between tip clearances. Following the contours of static entropy through the knee and exducer, the tip leakage vortex streamlines are increasing the entropy in the passage as they travel through and move towards the hub. At the first plane, the vortex is near the pressure surface of the splitter blade and causing the region of higher entropy to move into the main passage flow. In the middle plane, the vortex is about in the center of the passage, both pitchwise and spanwise, and again, increasing the entropy of the flow around it. And finally, near the exducer at the third plane, the vortex has moved closer to the hub and suction surface of the main blade as it traversed through the passage. The higher region of entropy around the vortex has somewhat separated from the highest entropy regions near the shroud. The flow closest to the shroud is now creating the highest entropy whereas the entropy generation from the vortex is smaller in amplitude but still forming part of the wake in the jet-wake structure at the exit of each impeller passage.

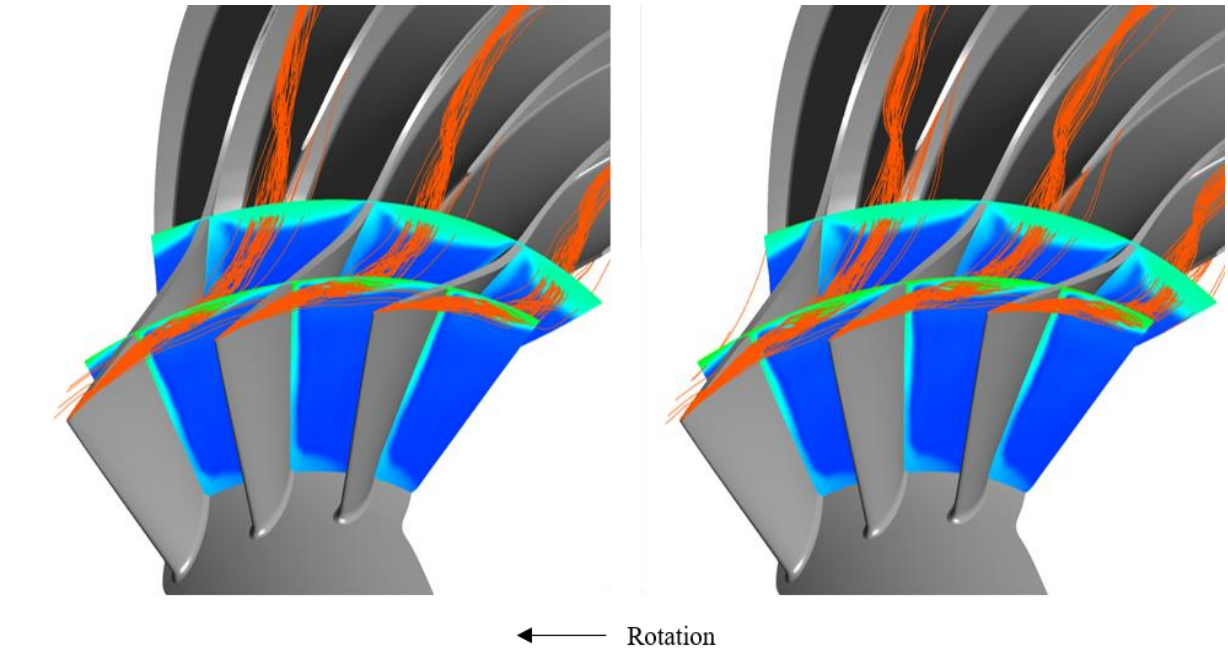

Figure 4.35 Tip leakage vortex trajectory and entropy contours in the inducer for the nominal clearance (left) and the larger clearance (right)

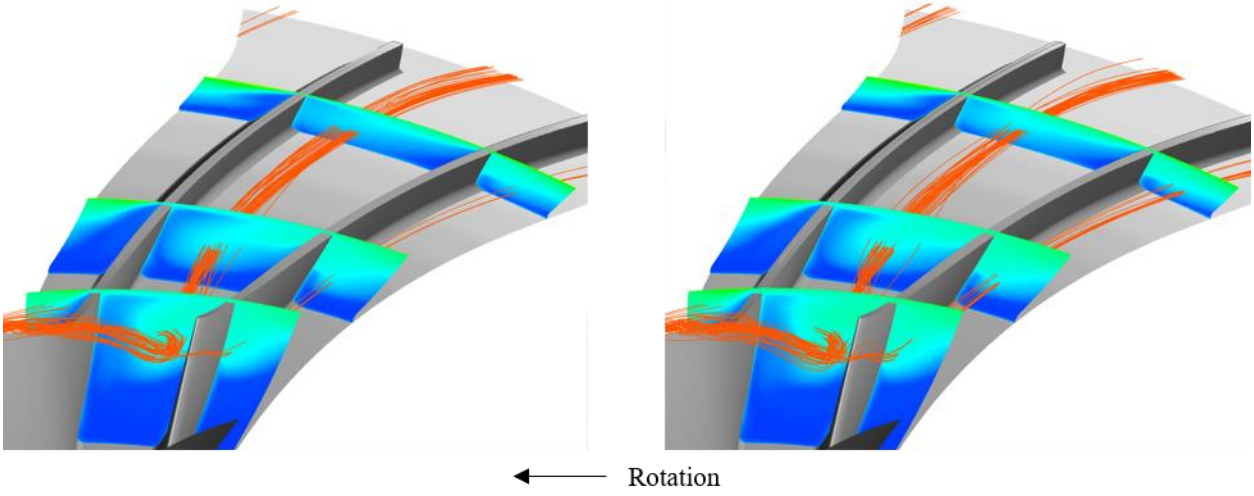

Figure 4.36 Tip leakage vortex trajectory and entropy contours in the knee and exducer for the nominal clearance (left) and the larger clearance (right)

A top-down view of the leading edge of the impeller main blades is shown in Figure 4.37 with the tip leakage vortex streamlines originating from the tip gap above the leading edge. Each streamline is colored with the magnitude of velocity at each point in the flow. From this view,

there is a small change in the angle at which the vortex forms when it sheds off the leading edge. The vortex from the nominal clearance simulation develops in a slightly more streamwise direction than the vortex from the simulation with the larger clearance. The increase in angle likely causes more of the vortex to divert around the splitter blade in the larger clearance simulation. The tip clearance in the inducer does not change much due to the axial movement of the impeller to adjust the clearance, but the nominal clearance has a larger mass flow for this similar loading condition. The similar loading condition indicates that the incidence into the impeller should be closely matched but with increased mass flow rate for the nominal clearance. The increase in mass flow rate is likely causing the slight shift in the angle of the tip leakage vortex and the altered trajectory through the passage.

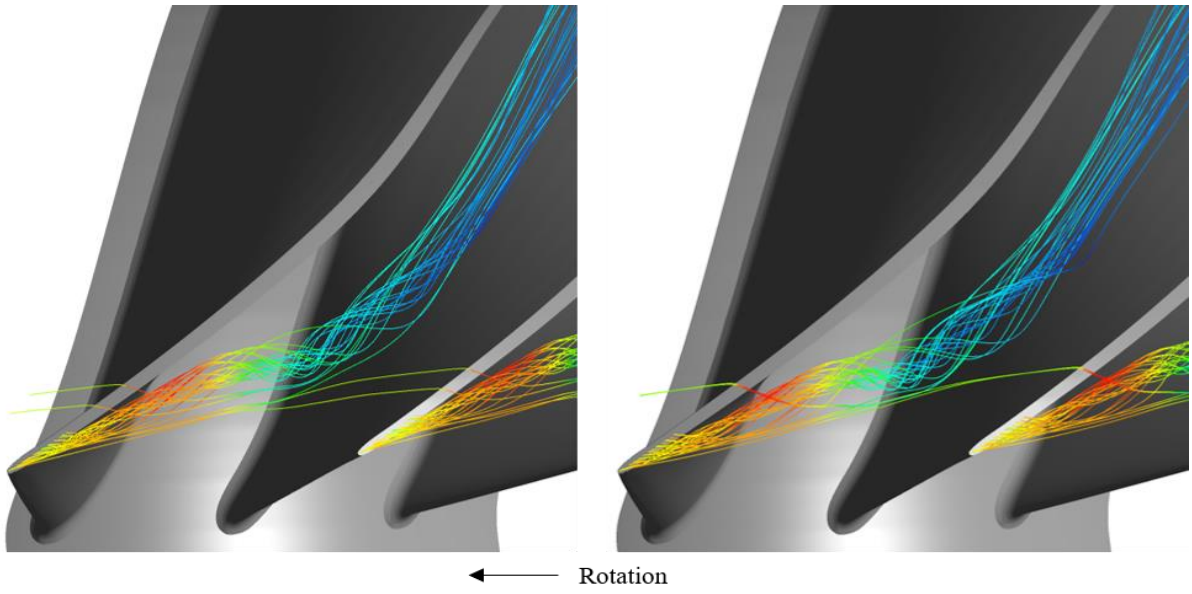

Figure 4.37 Tip leakage vortex formation at the leading edge of the main blade for the nominal clearance (left) and the larger clearance (right)

4.3.3 Diffuser Performance and Sensitivity

The tip clearance effects on the diffuser performance are a bit different from those for the stage and the impeller. As the experimental data showed in Section 4.2.3, the diffuser provides better static pressure rise overall but the static pressure rise coefficient and the total pressure loss coefficient both show decreased performance with nominal tip clearance. This leads to the conclusion that the diffuser effectiveness is better when operating with the larger tip clearance.

However, at the nominal tip clearance, the impeller and the diffuser still achieve a better static pressure rise. Because the impeller is doing more of the static pressure rise at the nominal clearance, the diffuser does not have to, and this causes the effectiveness to be lower at the nominal tip clearance. While the performance of the diffuser in the numerical simulation does not match the experimental data well, the tip clearance trends are captured.

Figure 4.38 shows the diffuser static pressure rise coefficient for both tip clearances from the experimental data and the numerical simulation. As discussed earlier, the value of C_p is higher for the larger tip clearance and this trend is captured by the numerical simulation. In the upper part of the speedline, the larger tip clearance C_p value increases past that value for the nominal clearance. The increase in C_p continues for all points from the experimental data as the mass flow is decreased, but the numerical simulation predicts a nearly constant value with a slight decrease for both tip clearances. When comparing the points of similar incidence, the trend is matched well between the experiment and the numerical simulation. Figure 4.39 compares the two trends at the design speed. The numerical simulation underpredicts the effects of increasing tip clearance, but the slopes are still comparable. The experimental data show a slope of -0.628 while the numerical simulation predicts the slope to be -0.55. Despite the overprediction in the static pressure rise coefficient through the diffuser, the numerical simulation is still able to capture trend of decreasing C_p with decreasing tip clearance.

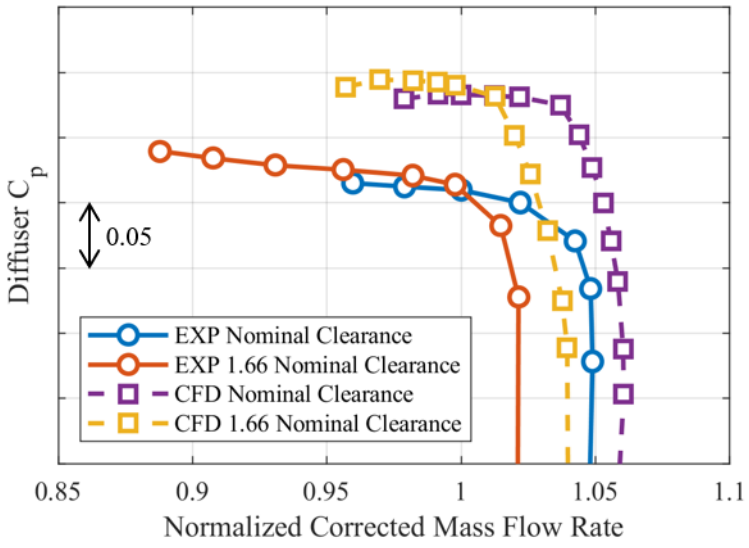

Figure 4.38 Diffuser C_p map comparison

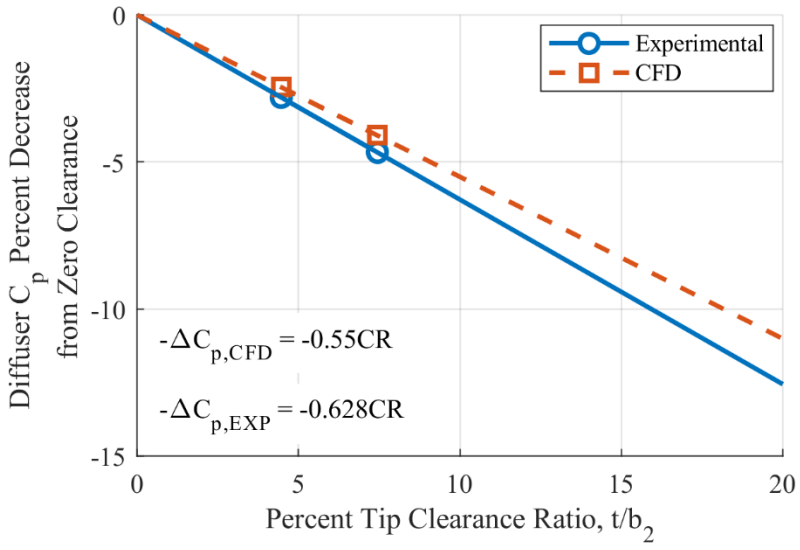

Figure 4.39 Diffuser C_p sensitivity at design speed

The total pressure loss coefficient is predicted similarly to the static pressure rise coefficient. Depicted in Figure 4.40 is the total pressure loss coefficient for both tip clearances calculated from the experiment and the numerical simulation. The prediction from the numerical simulation is higher for both tip clearances but matches the general shape of the speedline well. The top of the graph is not shown so that it could be zoomed in to near the operating point. Because the numerical simulation predicts a higher C_p through the diffuser, a higher total pressure loss is also expected because more diffusion is being done. The numerical simulation also captures the bucket shape of the graph, but the minimum is shown to be a different point in the numerical simulation than in the experiment. The increase in total pressure loss resulting from decreasing the tip clearance to the nominal value is underpredicted by the numerical simulation, as shown in Figure 4.41. The experimental slope is 1.481 whereas the slope for the results from the numerical simulation is only 1.184. Therefore, the numerical simulation is underpredicting the effect of the tip clearance on the total pressure loss coefficient, but it does match the result that the diffuser total pressure loss increases at the nominal clearance.

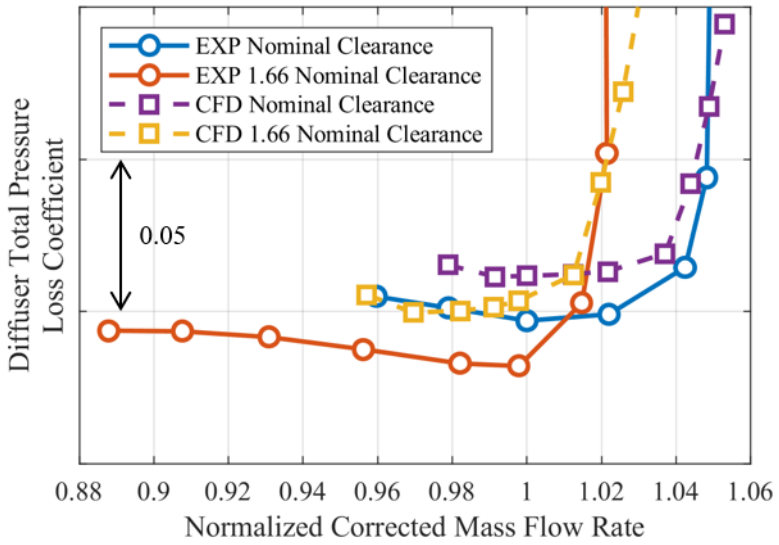

Figure 4.40 Diffuser total pressure loss coefficient map comparison

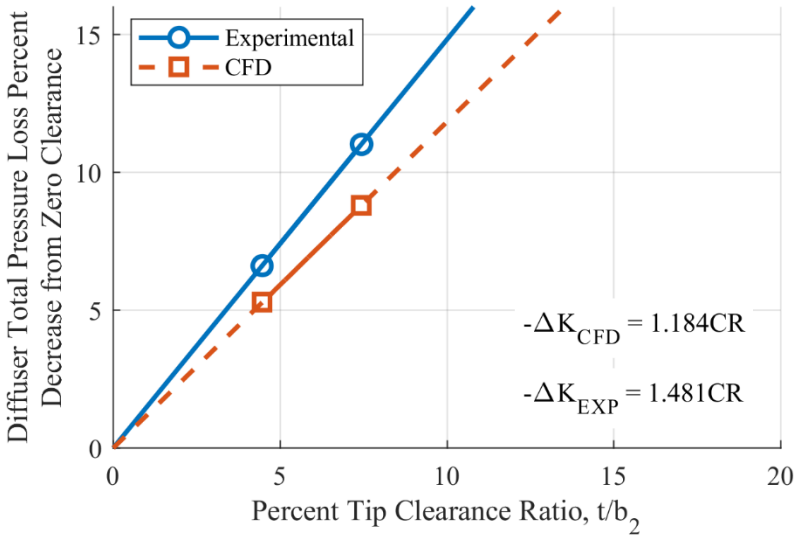

Figure 4.41 Diffuser total pressure loss coefficient sensitivity at design speed

The final performance parameter is the diffuser effectiveness, which is a function of both the static pressure rise coefficient and the total pressure loss coefficient. Since the numerical model overpredicts both coefficients, it is expected that the effectiveness prediction will be closer, as illustrated by Figure 4.42. The diffuser effectiveness is slightly overpredicted by the numerical model but matches better than C_p or K. The shape of the upper part of the speedline is also matched

by the numerical simulation, where the diffuser effectiveness is nearly constant with decreasing mass flow rate. Also as expected, the numerical simulation predicts that the diffuser is more effective at the larger tip clearance. However, the magnitude of the decrease in effectiveness is underpredicted by the numerical model. Figure 4.43 shows both trends from the experiment and the numerical simulation. The experimental slope is -0.746 while the slope from the numerical simulation is only -0.575. Despite the effectiveness being the most closely predicted to the values from the experiment, the trend is not as good as that from the static pressure rise coefficient.

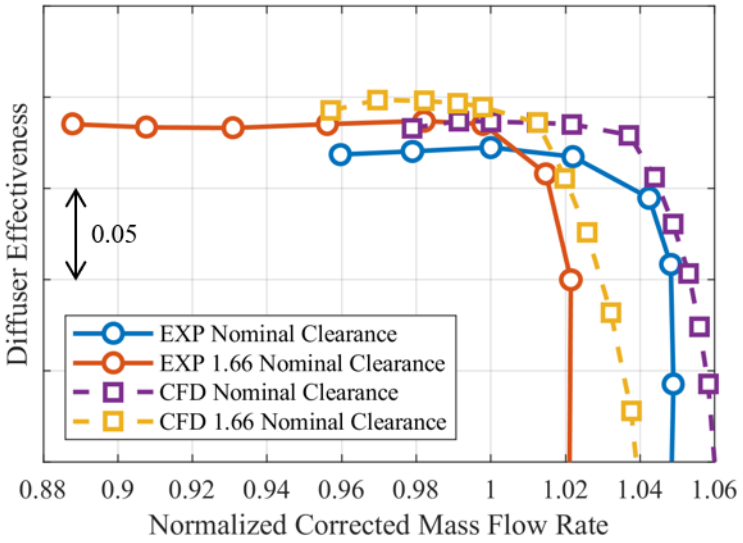

Figure 4.42 Diffuser effectiveness map comparison

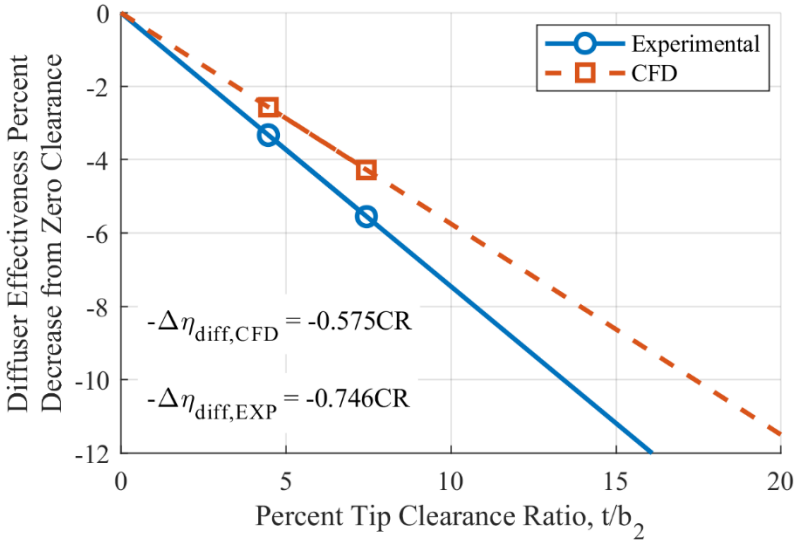

Figure 4.43 Diffuser effectiveness sensitivity at design speed

The static pressure rise through the diffuser for both the experiment and the numerical simulation is compared in Figure 4.44. The impeller exit static pressure, station 2, matches well between the experiment and numerical simulation for both tip clearances. However, the differences become evident immediately at station 3. In the numerical simulation, the mixing plane is placed between stations 2 and 3. Because of this, the static pressure rise across the vaneless space is overpredicted. The increase in static pressure from station 3 to station 4 is predicted well by the numerical model but the actual value is still overpredicted due to the effects of the mixing plane. Between stations 4 and 5, the differences in static pressure rise between the experiment and the numerical simulation continue to grow incrementally. The numerical simulation is overpredicting the static pressure at each point for both tip clearances. At station 5, the static pressure is overpredicted but the differences between the two tip clearances are comparable between the experiment and the numerical simulation. The numerical simulation predicts a similar trend of static pressure rise due to the tip clearance through the diffuser with similar proportions of static pressure rise at each point in the diffuser.

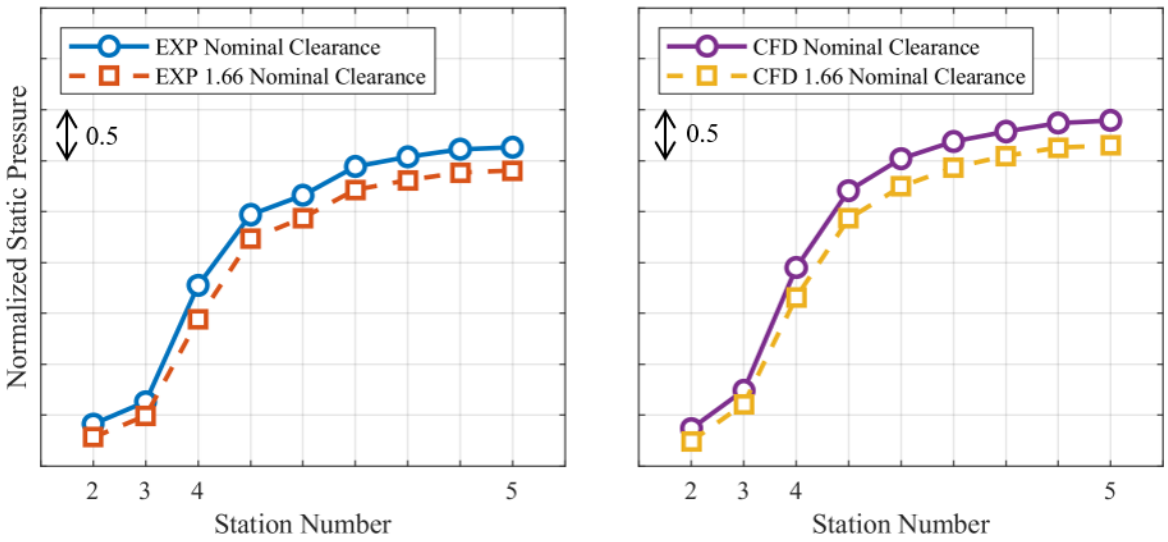

Figure 4.44 Comparison of the diffuser static pressure rise for the experiment (left) and the numerical simulation (right)

5. CONCLUSIONS AND RECOMMENDATIONS

This research aimed to investigate the tip clearance effects on the stage and component performance of a high-speed centrifugal compressor. The tip leakage flow is one of the main secondary flows that can hinder the performance of a centrifugal compressor. Stage performance effects have been well-documented for older centrifugal stages, but as centrifugal compressors become more common in the aerospace industry due to the higher-pressure ratio stages needed, reducing the losses that occur in the compressor is increasingly important. Not many of the previous studies investigate the tip clearance effects on each component's performance, though. Studying the components can provide more insight into how the tip leakage flow is affecting the flow field but also the sensitivity of various performance parameters to the changing tip clearance in the impeller. Additionally, a numerical model was developed to compare the results to the experimental data for each tip clearance and to study the resulting flow features.

5.1 Development and Validation of the Numerical Model

A steady simulation using the ANSYS CFX software was performed to predict the stage and component performance as well as the effects of changing the tip clearance. One passage per domain was simulated with the BSL turbulence model as well as accounting for surface roughness. Stage mixing planes were used as component interfaces when the reference frame was changing or when the pitch changed between domains. Inlet total temperature and total pressure were specified, and the outlet boundary condition was specified as either a mass flow rate for the upper half of the speedline or a static pressure for the choke half of the speedline. The tip clearance was changed to match the experimental data at the inducer, knee, and exducer of the impeller with curve fits between each point for the entire shroud. A grid convergence study was performed to test the quality of the grid and quantify the errors from a solution with an infinite number of grid cells using a Richardson extrapolation. The middle grid tested was chosen for all simulations because it reduced the error in the solution without significantly increasing the computational time.

Stage performance predicted by the numerical simulation matches well with the experimental data. The total pressure ratio is overpredicted by 2.8% at the peak efficiency point using the larger tip clearance and the choked mass flow rate is overpredicted by about 2%. The

total temperature rise ratio is predicted well, and at the same peak efficiency point, it is overpredicted by 0.2%. However, accounting for the overprediction in choked mass flow rate shows that the total temperature rise ratio is actually underpredicted by a small amount. Because the efficiency depends on the total pressure ratio and the total temperature rise ratio, the efficiency is also overpredicted, and the error in the efficiency is 1.8%. Each experimental speedline has a sharp knee when transitioning from choke to the operating line while the numerical model predicts a much smoother transition.

Component performance in the impeller is predicted well while diffuser performance is lacking in some areas. The impeller total pressure ratio and impeller efficiency are both slightly underpredicted but still predicted well. At the peak efficiency point for the larger tip clearance, the error in impeller total pressure ratio is -0.8% and the error in impeller efficiency is -0.6%. As with the total temperature rise ratio, both impeller parameters are underpredicted more when accounting for the differences in choked flow. The static pressure rise through the impeller also matches with the experimental data very well. The numerical simulation underpredicts the static pressure through the knee of the impeller but it matches well at the exit.

Overall performance in the diffuser is overpredicted and the static pressure distributions across the diffuser passage do not accurately capture the experimental trends. The static pressure rise coefficient in the diffuser is overpredicted by 11.1% between the experiment and the numerical simulation. The total pressure loss coefficient is also overpredicted, but only by 5.9% at the peak efficiency point. Diffuser effectiveness, a parameter calculated using the static pressure rise coefficient and the total pressure loss coefficient, is more closely predicted because both coefficients that it is dependent on are overpredicted. An error of 1.6% exists between the numerical simulation and the experiment for the diffuser effectiveness.

The static pressure rise through the diffuser at each location shows that most of the differences occur at the diffuser leading edge and throat locations. These areas are critical in the diffuser and the use of a mixing plane between the impeller and diffuser is hindering the results of the numerical simulation. Static pressures across the leading edge of the diffuser show that the general trend can be predicted but it is missing some of the detailed flow features. On the pressure surface of the diffuser vane, the numerical simulation predicts a higher pressure than in the experiment but the minimum pressure, near mid-pitch, is predicted well in magnitude but slightly shifted in the passage relative to the experimental data. On the suction surface, a small area of

separation exists with a decrease in pressure closest to the vane surface. The numerical model does not predict that separation bubble and the pressure continues to increase toward the vane surface. Likewise, in the diffuser throat, the trend between the experimental data and the numerical simulation is matched better but the pressure is still overpredicted by the numerical simulation. The overprediction of pressure continues through the rest of the passage but the increase in the overprediction is much smaller at the rest of the points.

Overall, the performance of the numerical model was able to capture the qualitative nature of the performance of the stage and components but was lacking more in the quantitative nature of the performance. While some of the performance parameters appeared to match very well, accounting for the difference in choked mass flow rate showed that they are actually slightly underpredicted. However, the good prediction of the qualitative performance allows the model to be used to predict the effects and sensitivities of the tip clearance.

5.2 Tip Clearance Effects and Sensitivities

To compare data points of different impeller tip clearances, an investigation was performed to find the best method. In previous studies, different tip clearances tested all had the same choke mass flow rate, indicating that choking was happening in impeller. In this case, comparing points of similar inlet corrected mass flow rates was representative. However, the SSCC chokes in the diffuser so changing the tip clearance alters the choke mass flow rate. Comparing points with similar inlet corrected mass flow rates resulted in two different loading conditions on each speedline. To resolve this issue, the design point was chosen as an anchor point and different parameters were used to pick the closest point on the larger clearance speedline. The parameters used were inlet corrected mass flow rate, exit corrected mass flow rate, a condition of similar loading and incidence defined by $TPR/\dot{m}_{inlet\ corr.}$, and the work factor. The similar loading condition of $TPR/\dot{m}_{inlet\ corr.}$ and the exit corrected mass flow rate chose the same point for the experimental data. A study of the three different points showed that the point chosen by $TPR/\dot{m}_{inlet\ corr.}$ and exit corrected mass flow rate gave the best comparison between points of different tip clearances. Because the loading factor requires less information to calculate, it was chosen for use for the rest of the investigation. However, exit corrected mass flow rate will represent points on a constant throttle line better than the loading factor, and if those two parameters choose different points, the exit corrected mass flow rate point is recommended.

The sensitivity of the stage and component performance parameters was first evaluated across the speed range from 60% to 100% corrected speed. Then the ability of the numerical model to predict the performance and the sensitivity was compared at 100% corrected speed. On a stage level, the total pressure ratio, efficiency, and work factor were the parameters compared at different tip clearances. The total pressure ratio and efficiency both showed the maximum sensitivity at 85% corrected speed. Above that speed, the total pressure ratio sensitivity was very similar, but the efficiency sensitivity decreased with increasing speed. Around 85% corrected speed, the impeller becomes transonic and a shock wave forms on the suction surface of the main blades at the inducer. The formation of the shock wave affects the sensitivity of the total pressure ratio by keeping it nearly constant through the rest of the speed range while the sensitivity of the efficiency decreases. The work factor, however, shows very little change in sensitivity around the speed at which the impeller becomes transonic. In general, the work factor is much less sensitive to the changing tip clearance than the total pressure ratio or the efficiency.

The numerical simulation can predict the performance and sensitivity of the stage performance parameters well. The total pressure ratio is overpredicted for both tip clearances by the numerical simulation, but the sensitivity matches closely with the experiment. The slope of the sensitivity in the total pressure ratio is 1.196 for the numerical simulation and 1.127 for the experiment. Similarly, the efficiency is overpredicted for both speedlines by the numerical simulation, but the sensitivity is underpredicted. The sensitivities for the total pressure ratio matched well but with the efficiency, the slopes are 0.465 for the numerical simulation and 0.537 for the experiment. And finally, the work factor is predicted the most accurately out of the stage performance parameters. The speedlines are almost exact with some slight overpredictions and some slight underpredictions. The comparison of the sensitivities is similar to that of the total pressure ratio. The numerical simulation predicts the sensitivity slope to be 0.377 while the experimental sensitivity is 0.302.

The impeller performance is the most sensitive to changes in the tip clearance. Like the stage performance, the maximum sensitivity for both the impeller total pressure ratio and the impeller efficiency occurs at 85% corrected speed, where the impeller becomes transonic. The impeller total pressure ratio sensitivity above 85% corrected speed is smaller but on the same order as that at 85% corrected speed. The impeller efficiency however, trends very similarly to the stage efficiency with discrete decreases from 85% to 100% corrected speed. The impeller total pressure

ratio is influenced by the formation of the shock, but the sensitivity is affected less after its formation. The impeller efficiency, however, is influenced by the formation of the shock and the continuous increase in Mach number as the speed is increased. The effects of tip clearance on the static pressure rise through the impeller are all in the knee and exducer of the impeller. By changing the axial tip clearance, the clearance in the knee is affected but the clearance in the inducer is relatively unchanged, leading to the differences in static pressure rise becoming clear in the knee of the impeller.

An accurate prediction of the impeller performance and sensitivity is provided by the numerical model. The impeller total pressure ratio is predicted very well for both tip clearances when compared to the experimental data. Both speedlines match up well with some small over and underpredictions at each point. However, when accounting for the difference in choked mass flow rate between the CFD and the experiment, the CFD underpredicts the impeller total pressure ratio and efficiency by a larger amount. Additionally, the sensitivity of the impeller total pressure ratio is predicted exactly by the numerical model. An experimental slope of the sensitivity of 1.398 is matched by the numerical solution. The impeller efficiency is not predicted as well as the impeller total pressure ratio. The numerical model underpredicts the efficiency for both tip clearances. The nominal clearance impeller efficiency is underpredicted more than the larger clearance thus leading to the underprediction in the sensitivity. The impeller efficiency sensitivity slope is 0.671 for the experimental data but only 0.562 for the numerical simulation. Despite the impeller efficiency underprediction, the static pressure rise in the impeller between tip clearances is predicted very well. Again, there is a small underprediction in overall static pressure but when comparing the differences between tip clearances, the numerical model matches closely to the experimental data.

Investigation into the flow physics in the impeller revealed that the tip leakage vortex is very similar between the two operating clearances. The vortex starts at the leading edge of the main blade in the inducer and traverses through the passage. The vortex does not change much because the inducer tip clearance change between the two operating conditions is very small. But the nominal tip clearance vortex is slightly closer to the suction side of the main blade as it forms because of the increase in mass flow rate resulting from the smaller tip clearance. The vortex then intersects the leading edge of the splitter blade where most of it stays in the same passage and moves from the splitter blade pressure surface towards the main blade suction surface through the

knee and exducer of the impeller. The vortex leaving the impeller then forms part of the wake in the jet-wake structure at the exit.

The contours of relative total pressure at the impeller exit change with the decreasing tip clearance. The main differences between the contours are located above 50% span at the exit and on the pressure surfaces of each blade. The main blade pressure surface shows significantly more differences between the simulations than the splitter blade pressure surface. There is a higher relative total pressure on the pressure surface of the main blade as not as much flow is leaking from the pressure surface to the suction surface. The splitter blade pressure surface also has an increased region of relative total pressure compared to the larger clearance simulation, but it is not as drastic of a change as that from the main blade. The wake regions on both the main and splitter blades are smaller for the nominal clearance case due to the increased relative total pressure regions.

Performance in the diffuser with changing tip clearances shows the opposite trends from the impeller. Using the performance parameters static pressure rise coefficient, total pressure loss coefficient, and effectiveness, the diffuser performance at the larger tip clearance is better. This leads to negative slopes in the general sensitivity equation for the static pressure rise coefficient and effectiveness. The total pressure loss coefficient is defined such that an increased total pressure loss will result in a positive slope for the sensitivity. All three parameters show maximum sensitivity at 85% or 90% corrected speed. The static pressure rise coefficient sensitivity marginally decreases from 85% to 90% corrected speed but then significantly decreases up to 100% corrected speed. The total pressure loss coefficient shows similar trends where the sensitivity at 85% and 90% corrected speeds are similar but then decreases as the speed is increased to 100% corrected speed. Finally, diffuser effectiveness is also very similar but trends more closely to the static pressure rise coefficient with a marginal decrease from 85% to 90% corrected speed and then significantly larger decreases up to 100% speed. The static pressure rise through the diffuser measured at each location shows that the majority of the differences between the two tip clearances occurs between the leading edge and the throat of the diffuser.

Because the diffuser performance was characterized as being moderately better for the larger tip clearance case, the matching of the impeller and diffuser peak performance operating points was investigated. By examining the peak efficiency point for the stage and the impeller and the peak effectiveness point for the diffuser on each speedline, this matching can be evaluated. If

the components are all operating at peak performance, all three points will be the same data point. This occurs at 100% corrected speed for the nominal clearance indicating that the impeller and the diffuser are both at peak efficiency for the design point. Because a difference in operating condition between components is not causing the diffuser performance behavior and the opposite trend in static pressure rise through the diffuser, it is determined that the diffuser must do more to diffuse the flow at the larger tip clearance. The impeller has a higher static pressure rise at the nominal clearance, so the diffuser does not need to diffuse the flow as much as it does for larger tip clearance operation.

The numerical simulation of the diffuser struggles to accurately predict quantitative performance metrics, but the trends are captured. The static pressure rise and total pressure loss coefficients are both overpredicted by the numerical simulation by a substantial amount. However, it does capture the trend that the nominal clearance diffuser performance is worse than the diffuser performance at the larger clearance for all three parameters. The sensitivity in the static pressure rise coefficient is predicted by the numerical simulation to have a slope of -0.55 whereas the experimental sensitivity slope is -0.628. The static pressure rise through the diffuser predicted by the numerical simulation is also overpredicted at many points but the trend between tip clearances is similar to the experimental data. The diffuser throat is the location where the largest discrepancy occurs between the experiment and the numerical simulation. The total pressure loss coefficient follows a similar trend where the performance is overpredicted, but the sensitivity is underpredicted. The sensitivity slope prediction for the total pressure loss coefficient is 1.184 and an experimental slope of 1.481 is calculated. Finally, the diffuser effectiveness is predicted to be more accurate than the two coefficients because both are overpredicted. A value of -0.575 is predicted as the sensitivity slope for the numerical simulation but -0.746 is the slope for the experimental data. Overall, the diffuser trends are underpredicted, but the performance is significantly overpredicted for each of the parameters.

5.3 Recommendations for Future Research

While the steady performance and sensitivity of the tip clearance was the focus of this thesis, a few other areas of research with respect to tip clearance effects should be investigated. Because only one tip clearance data set was tested from choke to surge, the other tip clearance could also be tested to surge instead of just past peak efficiency. The additional data would allow

for characterization of the change in surge margin as previous literature has not reached a definitive conclusion. The capabilities with the unsteady instrumentation on this compressor would also allow for changes in the surge signature as well as differences in component stability to be evaluated. Additionally, a smaller, third tip clearance could be added to not only address the unsteady effects but to evaluate the trends and sensitivities. With only two tip clearances currently tested, all trends were assumed to be linear. Previous studies have shown the trends are approximately linear but the additional data here could validate that assumption.

The performance of the numerical model was not bad overall; however, improvements could be made. The model presented here can be used for other investigations where a steady model is appropriate. For better results though, a transient model should be developed to eliminate the use of the mixing planes. The transient model should be able to predict the impeller performance and flow characteristics more accurately and provide a significant improvement to the diffuser performance. Currently, the diffuser performance is lacking important flow features that are averaged out by the mixing plane. Consequently, the diffuser is being predicted as having better performance than in the experiment. The transient model would be able to provide more accurate results and flow modeling. Additionally, should other studies be carried out where the addition of numerical results would provide a good comparison, the use of a transient model would be beneficial to accurately capture the performance and flow characteristics.

APPENDIX: ANSYS CFX IDEAL GAS CALCULATIONS

The software used for the numerical simulation, ANSYS CFX, offers options for materials to be used in the simulation, in this case, air modeled as an ideal gas. Research conducted using this software used a built-in material named "Air Ideal Gas", which was thought to be calculating air properties under the assumption that the air was thermally perfect but not calorically perfect. After analyzing results using this material, it was found that the efficiency calculations for the simulation using the ANSYS functions and those from the experimental method disagreed significantly. Since the comparison of the numerical results to the experimental data was important, the disagreement was investigated, and settings were found inside the fluid model that were assuming the air to be calorically perfect with no change in the constant pressure specific heat. Hence, the name "Air Ideal Gas" is very misleading and would be more appropriately named "Air Perfect Gas."

Settings in the CFX-Pre software allow for the constant pressure specific heat to be changed from a constant value to a curve fit, where the coefficients must be input by the user. One option is to input coefficients using the NASA format of the equation while the other option is to input coefficients for a zero-pressure polynomial. For this study, the NASA format was chosen, and the coefficients found online. Through the search for the correct coefficients for air, it was found that there are two formats of the NASA equation, the first published in 1967 and then later updated in 1992 with two additional terms. While ANSYS requires the older coefficients for use in their software, Burcat and Ruscic (2005) note that the new format and coefficients result in an improved error between one and two orders of magnitude. As with the older format, the new equation format uses two different sets of coefficients for the lower temperature range, between 200 K and 1000 K, and the upper temperature range, between 1000 K and 6000 K. Reproduced in equations A.1-A.3

$$\frac{C_P^0}{R} = a_1 T^{-2} + a_2 T^{-1} + a_3 + a_4 T + a_5 T^2 + a_6 T^3 + a_7 T^4 \qquad \text{(A.1)}$$

$$\frac{H^0}{R} = -a_1 T^{-2} + a_2 T^{-1} \ln(T) + a_3 + \frac{a_4}{2} T + \frac{a_5}{3} T^2 + \frac{a_6}{4} T^3 + \frac{a_7}{5} T^4 + \frac{b_1}{T} \qquad \text{(A.2)}$$

$$\frac{S^0}{R} = \frac{-a_1 T^{-2}}{2} - a_2 T^{-1} + a_3 \ln(T) + a_4 T + \frac{a_5}{2} T^2 + \frac{a_6}{3} T^3 + \frac{a_7}{4} T^4 + b_2 \quad \text{(A.3)}$$

is the new nine term format. Each of the corresponding coefficients from McBride (1996) are listed in Table A.1 for reference.

Table A.1 Coefficients for 9 term NASA polynomial

Coefficient	Low Temperature Range	High Temperature Range
a_1	1.00995e4	2.415214e5
a_2	-1.968275e2	-1.257874e3
a_3	5.009155	5.144558
a_4	-5.761013e-3	-2.13854e-4
a_5	1.06685e-5	7.065227e-8
a_6	-7.940297e-9	-1.071483e-11
a_7	2.185231e-12	6.5778e-16
b_1	-1.767967e2	6.462263e3
b_2	-3.9215	-8.147408

After implementation of the seven term NASA polynomial into the software, the results were compared to illustrate the effect that adding a variable specific heat had on the performance, specifically the efficiency. The efficiency for each simulation was calculated first using the built in ANSYS function for enthalpy at each of the rake locations and then averaged accordingly to calculate a stage efficiency. The experimental method of calculating efficiency involves the average of the total temperature and total pressure at the exit rake locations and using those values in REFPROP to calculate enthalpy, and subsequently, efficiency. Calculations for the simulation in REFPROP assume that air is a real gas with a composition of nitrogen, oxygen, carbon dioxide, and argon with no humidity. A comparison of the two methods for each set of simulations, one with a perfect gas and one with an ideal gas, is shown in Figure A.1. The normalized corrected mass flow rate is the abscissa and the change in efficiency between the ANSYS functions and the REFPROP method is the ordinate. A difference of more than 1 point in efficiency is realized between the methods for the simulations using a perfect gas but by switching to an ideal gas, the difference in calculated efficiency between the methods decreased by about a factor of 10.

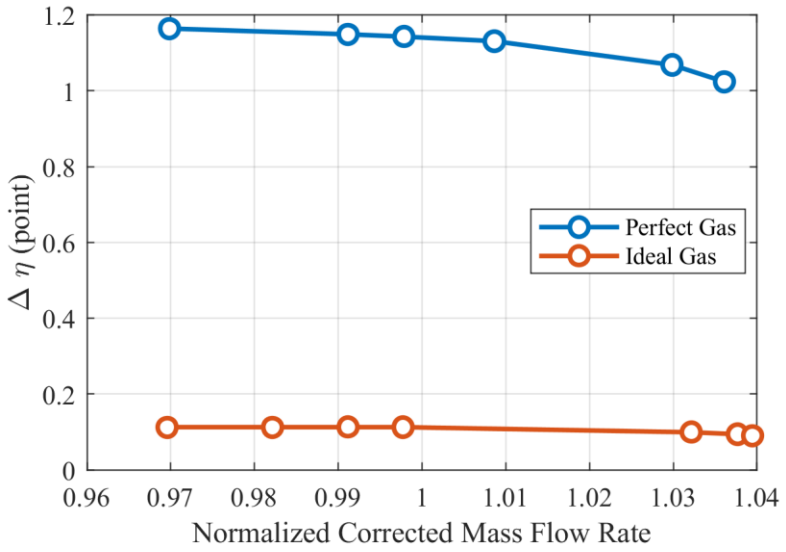

Figure A.1 Efficiency comparison between using perfect and ideal gas

REFERENCES

ANSYS CFX-Solver Theory Guide. (2019). ANSYS, Inc.

Backman, J. L. H., Reunanen, A., Saari, J., Turunen-Saaresti, T., Sallinen, P., & Esa, H. (2007). *Effects of Impeller Tip Clearance on Centrifugal Compressor Efficiency*. 1141–1146. https://doi.org/10.1115/GT2007-28200

Berdanier, R. A., Smith, N. R., Fabian, J. C., & Key, N. L. (2015). Humidity effects on experimental compressor performance—Corrected conditions for real gases. *Journal of Turbomachinery*, *137*(3), 031011.

Brasz, J. J. (1988). *Investigation Into the Effect of Tip Clearance on Centrifugal Compressor Performance*. V001T01A066. https://doi.org/10.1115/88-GT-190

Buffaz, N., & Trébinjac, I. (2012). *Impact of Tip Clearance Size and Rotation Speed on the Surge Onset in a High Pressure Centrifugal Compressor*. 2491–2500. https://doi.org/10.1115/GT2012-68427

Bunker, R. S. (2003). The Effect of Thermal Barrier Coating Roughness Magnitude on Heat Transfer With and Without Flowpath Surface Steps. *Heat Transfer, Volume 2, 2003*, 1–10. https://doi.org/10.1115/IMECE2003-41073

Burcat, A., & Ruscic, B. (2005). *Third Millennium Ideal Gas and Condensed Phase Thermochemical Database for Combustion with Updates from Active Thermochemical Tables*. 417.

Celik, I., Ghia, U., Roache, P., Freitas, C., Coleman, H., & Raad, P. (2008). Procedure for Estimation and Reporting of Uncertainty Due to Discretization in CFD Applications. *Journal of Fluids Engineering*, *130*(7), 078001. https://doi.org/10.1115/1.2960953

CFX-Solver Modeling Guide. (2019). ANSYS, Inc.

Cumpsty, N. A. (1989). *Compressor Aerodynamics*. Krieger Publishing Company.

Eckardt, D. (1976). Detailed Flow Investigations Within a High-Speed Centrifugal Compressor Impeller. *Journal of Fluids Engineering*, *98*(3), 390–399. https://doi.org/10.1115/1.3448334

Eckert, B., & Schnell, E. (1961). *Axial- und Radial-Kompressoren* (2nd ed.). Springer-Verlag.

Eisenlohr, G., & Chladek, H. (1994). Thermal Tip Clearance Control for Centrifugal Compressor of an APU Engine. *Journal of Turbomachinery, 116*(4), 629–634. https://doi.org/10.1115/1.2929453

Eum, H.-J., & Kang, S.-H. (2002). *Numerical Study on Tip Clearance Effect on Performance of a Centrifugal Compressor*. 8.

Everitt, J. N., Spakovszky, Z. S., Rusch, D., & Schiffmann, J. (2017). The Role of Impeller Outflow Conditions on the Performance of Vaned Diffusers. *Journal of Turbomachinery, 139*(4), 041004.

Harada, H. (1985). Performance Characteristics of Shrouded and Unshrouded Impellers of a Centrifugal Compressor. *Journal of Engineering for Gas Turbines and Power*, *107*(2), 528–533. https://doi.org/10.1115/1.3239765

Hong, S.-S., Schleer, M., & Abhari, R. S. (2003). Effect of Tip Clearance on the Flow and Performance of a Centrifugal Compressor. *ASME Joint Fluids Engineering Conference*, 563–569. https://doi.org/10.1115/FEDSM2003-45094

Hummel, F., Lötzerich, M., Cardamone, P., & Fottner, L. (2005). Surface Roughness Effects on Turbine Blade Aerodynamics. *Journal of Turbomachinery*, *127*, 9.

Jaatinen, A., Turunen-Saaresti, T., Grönman, A., Röyttä, P., & Backman, J. (2012). *Experimental Study of the Effect of the Tip Clearance to the Diffuser Flow Field and Stage Performance of a Centrifugal Compressor*. 641–648. https://doi.org/10.1115/GT2012-68445

Japikse, D., & Baines, N. C. (1998). *Diffuser Design Technology*. Concepts ETI.

Klassen, H. A. W. (1977a). *Experimental performance of a 16.10-centimeter-tip-diameter sweptback centrifugal compressor designed for a 6:1 pressure ratio*. https://ntrs.nasa.gov/search.jsp?R=19770018140

Klassen, H. A. W. (1977b). *Experimental performance of a 13.65-centimeter-tip-diameter tandem-bladed sweptback centrifugal compressor designed for a pressure ratio of 6*. https://ntrs.nasa.gov/search.jsp?R=19780003059

Koch, C. C., & Smith, L. H. (1976). Loss Sources and Magnitudes in Axial-Flow Compressors. *Journal of Engineering for Power, 98*(3), 411–424. https://doi.org/10.1115/1.3446202

Kunte, R., Schwarz, P., Wilkosz, B., Jeschke, P., & Smythe, C. (2012). Experimental and Numerical Investigation of Tip Clearance and Bleed Effects in a Centrifugal Compressor Stage With Pipe Diffuser. *Journal of Turbomachinery*, *135*(1), 011005-011005–011012. https://doi.org/10.1115/1.4006318

Lou, F. (2016). *A study on flow development in an APU-style inlet and its effect on centrifugal compressor performance* [PhD Dissertation]. Purdue University.

Lou, F., Fabian, J. C., & Key, N. L. (2018, January 8). Design Considerations for Tip Clearance Sensitivity of Centrifugal Compressors in Aero Engines. *2018 AIAA Aerospace Sciences Meeting*. 2018 AIAA Aerospace Sciences Meeting, Kissimmee, Florida. https://doi.org/10.2514/6.2018-0071

McBride, B. J. G. (1996). *Computer Program for Calculation of Complex Chemical Equilibrium Compositions and Applications II. Users Manual and Program Description. 2; Users Manual and Program Description*. https://ntrs.nasa.gov/search.jsp?R=19960044559

Methel, J. (2016). *An Experimental Comparison of Diffuser Designs in a Centrifugal Compressor*. Purdue University.

Pampreen, R. C. (1973). Small Turbomachinery Compressor and Fan Aerodynamics. *Journal of Engineering for Power*, *95*(3), 251–256. https://doi.org/10.1115/1.3445730

Schleer, M., Song, S. J., & Abhari, R. S. (2008). Clearance Effects on the Onset of Instability in a Centrifugal Compressor. *Journal of Turbomachinery*, *130*(3), 031002-031002–031011. https://doi.org/10.1115/1.2776956

Senoo, Y., & Ishida, M. (1987). Deterioration of Compressor Performance Due to Tip Clearance of Centrifugal Impellers. *Journal of Turbomachinery*, *109*(1), 55–61. https://doi.org/10.1115/1.3262070

Shabbir, A., & Turner, M. G. (2004). A Wall Function for Calculating the Skin Friction With Surface Roughness. *Volume 5: Turbo Expo 2004, Parts A and B*, 1661–1671. https://doi.org/10.1115/GT2004-53908

Shum, Y. K. P., Tan, C. S., & Cumpsty, N. A. (2000). Impeller–Diffuser Interaction in a Centrifugal Compressor. *Journal of Turbomachinery*, *122*(4), 777–786. https://doi.org/10.1115/1.1308570

Tang, J., Turunen-Saaresti, T., Reunanen, A., Honkatukia, J., & Larjola, J. (2006). Numerical Investigation of the Effect of Tip Clearance to the Performance of a Small Centrifugal Compressor. *Volume 5: Marine; Microturbines and Small Turbomachinery; Oil and Gas Applications; Structures and Dynamics, Parts A and B, 2006*, 411–418. https://doi.org/10.1115/GT2006-90893

Turunen-Saaresti, T., & Jaatinen, A. (2013). Influence of the Different Design Parameters to the Centrifugal Compressor Tip Clearance Loss. *Journal of Turbomachinery*, *135*(1), 011017. https://doi.org/10.1115/1.4006388

Weimer, M. (1992, July 6). Design and test of an Active Tip Clearance System for centrifugal compressors. *28th Joint Propulsion Conference and Exhibit*. 28th Joint Propulsion Conference and Exhibit, Nashville,TN,U.S.A. https://doi.org/10.2514/6.1992-3189

Zhao, H., Wang, Z., Ye, S., & Xi, G. (2016). Numerical investigations on tip leakage flow characteristics and vortex trajectory prediction model in centrifugal compressor. *Proceedings of the Institution of Mechanical Engineers, Part A: Journal of Power and Energy*, *230*(8), 757–772. https://doi.org/10.1177/0957650916673230